

AMERICAN UNIVERSITY OF BEIRUT

Interference Mitigation in 5G Network
Densification Technologies: Algorithms and
Performance Limits

by

ASMAA WALID ABDALLAH

A dissertation
submitted in partial fulfillment of the requirements
for the degree of Doctor of Philosophy
to the Department of Electrical and Computer Engineering
of the Maroun Semaan Faculty of Engineering and Architecture
at the American University of Beirut

Beirut, Lebanon
April 2020

AMERICAN UNIVERSITY OF BEIRUT

Interference Mitigation in 5G Network Densification Technologies: Algorithms and Performance Limits

by
ASMAA WALID ABDALLAH

Approved by:



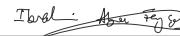
Prof. Ibrahim Abou Faycal , Professor
Electrical and Computer Engineering, AUB

Chairperson



Prof. Mohammad Mansour, Professor
Electrical and Computer Engineering, AUB

Advisor



Prof. Zaher Dawy, Professor
Electrical and Computer Engineering, AUB

Member of Committee



Prof. Naofal Al-Dahir, Professor
UT Dallas, USA

Member of Committee

Prof. Mérouane Debbah, Professor
CentraleSupélec , France



Member of Committee



Prof. Ahmed Eltawil, Professor
UC Irvine, USA

Member of Committee



Prof. Christoph Studer, Assistant Professor
Cornell University, USA

Member of Committee



Dr. Louay Jalloul,
Apple, USA

Member of Committee



Dr. Amitava Ghosh,
Nokia Bell Labs, USA

Member of Committee

Date of dissertation defense: April 22, 2020

AMERICAN UNIVERSITY OF BEIRUT

THESIS, DISSERTATION, PROJECT RELEASE FORM

Student Name: Abdallah Asmaa Walid
Last First Middle

Master's Thesis Master's Project Doctoral Dissertation

I authorize the American University of Beirut to: (a) reproduce hard or electronic copies of my thesis, dissertation, or project; (b) include such copies in the archives and digital repositories of the University; and (c) make freely available such copies to third parties for research or educational purposes.

I authorize the American University of Beirut, to: (a) reproduce hard or electronic copies of it; (b) include such copies in the archives and digital repositories of the University; and (c) make freely available such copies to third parties for research or educational purposes after: **One** ___ year from the date of submission of my dissertation.
Two ___ years from the date of submission of my dissertation.
Three ___ years from the date of submission of my dissertation.

Asmaa
Signature

May 13, 2020

Date

This form is signed when submitting the dissertation to the University Libraries

Acknowledgements

Firstly, I am thankful to Allah for the good health and the numerous blessings that has been bestowed upon me throughout my dissertation journey.

I would like to express my sincere gratitude to my advisor Prof. Mohammad Mansour for the continuous support of my Ph.D study and related research, for his patience, motivation, and immense knowledge. His guidance helped me in all the time of research and writing of this thesis. I could not have imagined having a better advisor and mentor for my Ph.D study.

Besides my advisor, I would like to thank the rest of my thesis committee: Prof. Ibrahim Abou Faycal, Prof. Zaher Dawy, Prof. Naofal Al-Dahir, Prof. Mérouane Debbah, Prof. Ahmed Eltawil, Prof. Christoph Studer, Dr. Louay Jalloul, and Dr. Amitava Ghosh, for their valuable and insightful comments and encouragement, but also for the hard question which incited me to widen my research from various perspectives.

I would like to also thank AUB and the Lebanese National Council for Scientific Research (CNRS-L) for their financial support granted through predoctoral fellowship.

I am also grateful for my dear friends: Salam Doumiati (my companion since day one), Reem Brome (my other sister), Rasha El Khansa, Tala Kichli, Dina Shaaban, Nadine Abbas, Lama Shaer, Nour Kouzayha, and Sara Jaleddine for all the fun we have had in the past years. Thank you ladies for always being there for me.

A special thanks goes to my parents for their endless love, unconditional support and guidance throughout my life. Words cannot express how grateful I am to my father Walid and my mother Rawan for giving me strength to reach for the stars and chase my dreams.

My sister Batool and my brothers Mohammad and Khalid deserve my wholehearted thanks as well. Thank you for the unceasing encouragement, support and attention, and for always listening to my problems.

Last but not least, I would like to express my deepest appreciation and gratitude to *Jad*, my soulmate, my beloved fiancé and my best friend, for providing

me with unfailing support and continuous encouragement throughout my years of study and research. He has been with me through it all and so he deserves big thanks for helping me keep things in perspective and for being a good listener. Thank you *Jad* for providing me all the love and care I needed to stay strong and to persevere. Without your precious support, and persistent help, this dissertation would not have been possible.

I consider myself so lucky to have such a lovely and caring family. This dissertation is dedicated to you.

An Abstract of the Dissertation of

Asmaa Walid Abdallah for Doctor of Philosophy
Major: Electrical and Computer Engineering

Title: Interference Mitigation in 5G Network Densification Technologies:
Algorithms and Performance Limits

The advent of fifth generation (5G) wireless technology is expected to unleash an unprecedented boost in network capacity, spectral and energy efficiencies, and peak data rates, accompanied by a significant increase in the number of connected devices via ultra-low latency connections. To achieve these aggressive goals, network densification has emerged as a mainstream technology in 5G in various manifestations to improve the capacity and spectral efficiency: increasing the number of base stations, increasing the number of antennas per site (a.k.a. massive multiple-input multiple-output (MIMO)), deploying distributed cell-free massive MIMO, employing distributed device-to-device (D2D) communications, and applying non-orthogonal multiple access (NOMA) communications, among many others. However, interference, whether in the form of inter-user or inter-cell, remains the major bottleneck as we densify the networks and reuse the spectral resources, and cannot be eliminated if we rely on network-centric topologies. While the spatial dimensions available at the centralized and distributed massive MIMO base stations (BSs) can be leveraged to suppress interference at the user equipment (UE), new approaches for interference mitigation that take into consideration the underlying hardware constraints and impairments, as well as signaling overhead are needed. In addition, by exploiting the physical proximity of communicating devices, offloading traffic from network-centric entities to distributed D2D networks and increasing resource utilization via NOMA communications, adequate user pairing criteria and power allocation policies become attractive efficient interference mitigation schemes with affordable complexity and signaling overhead.

In this dissertation, we investigate the problem of efficient interference mitigation schemes for emerging network densification technologies in 5G communications from four different perspectives. First, we propose and analyze channel

allocation (CA) and power control (PC) schemes to mitigate interference in a D2D underlaid cellular system modeled as a random network using stochastic geometry. Second, we extend the proposed interference mitigation techniques to consider NOMA MIMO systems. Third, in the context of massive MIMO systems, we propose and analyze the performance of various baseband processing schemes under low resolution analog-to-digital converters (ADCs). We analyze the uplink achievable rate by a massive MIMO system when the base station is equipped with a large number of low-resolution ADCs. We propose new techniques that account for the severe non-linearity effects of the coarse quantization and incorporate a pilot-based channel estimation error. Fourth, in the context of distributed massive MIMO systems, we study angle-domain processing techniques targeted for suppressing interference in frequency-division duplexing (FDD) based cell-free massive MIMO systems. Most prior work on cell-free (distributed) massive MIMO systems assume time-division duplexing mode, although FDD systems dominate current wireless standards. Efficient power control schemes are investigated for cell-free massive MIMO systems while considering the effect of backhaul power consumption. This dissertation describes the research scope, presents the completed work, and draws the future work.

Contents

Acknowledgements	v
Abstract	vii
1 Introduction	1
1.1 Network Densification Technologies	1
1.1.1 D2D Communication Technology	3
1.1.2 NOMA Communication Technology	3
1.1.3 Massive MIMO Communication Technology	4
1.1.4 Cell-Free Massive MIMO Communication Technology	5
1.2 Contributions and Outline	7
1.3 Publications and Awards	10
1.3.1 Thesis Related	10
1.3.2 Non-Thesis Related	12
1.3.3 Awards	12
2 Literature Review	13
2.1 Power Control and Resource Allocation in D2D Communications	13
2.2 Detection and Power Control in MIMO-NOMA systems	15
2.3 Low Resolution Detection in Massive MIMO	18
2.4 Array Signal Processing in Cell Free Massive MIMO	18
3 Channel Allocation and Coverage Probability Analysis for D2D Underlaid Cellular Systems	21
3.1 D2D System Model	22
3.2 Proposed Channel Allocation Scheme	27
3.3 Analysis of Coverage Probability	30
3.3.1 Cellular Link Coverage Probability	30
3.3.2 D2D Link Coverage Probability	32
3.3.3 Discussion	33

4	Proposed D2D Distributed Power Control Schemes	35
4.1	Proposed Distance-based Path-loss Power Control (DPPC)	35
4.1.1	Analysis of Power Moments	37
4.1.2	Sum Rate of D2D Links	38
4.1.3	D2D Power Control Threshold for DPPC	39
4.2	Proposed Extended Distance-based Path-loss Power Control (EDPPC)	42
4.2.1	Analysis of Power Moments	43
4.3	Proposed Soft Dropping Distance-based Power Control (SDDPC)	46
4.4	Discussion	48
4.5	Simulation Results	50
4.5.1	Simulation Setup	51
4.5.2	Coverage Probability for DPPC and EDPPC with Variable Parameters	52
4.5.3	Cellular Coverage Probability for all PC schemes	53
4.5.4	D2D Coverage Probability for all PC schemes	53
4.5.5	Coverage Probability with Variable Channel Allocation parameter (M)	55
4.5.6	Spectral and Power Efficiency	55
4.6	Conclusion	57
5	Clustering and Power Control for NOMA-MIMO systems	64
5.1	System Model	65
5.2	Proposed Joint Clustering and Power Control	67
5.2.1	Multi-User MIMO-NOMA Detection	69
5.3	Preliminary Simulation Results and Discussions	71
5.4	Conclusion	72
6	Low-Resolution Massive MIMO	73
6.1	System Model and Proposed Detection Scheme	73
6.1.1	Quantization in the ADC	74
6.1.2	Channel Estimation	77
6.1.3	Data Detection	78
6.2	Analysis of Uplink Achievable Rate	79
6.2.1	Sum-Rate Approximation for Gaussian Inputs	79
6.3	Extended study for downlink (DL) quantized massive MIMO . . .	82
6.4	Experimental Simulation Results	85
6.4.1	Simulation Setup	85
6.4.2	Achievable Rates with perfect and imperfect CSI	86
6.5	Conclusion	89
7	Array Signal Processing For FDD-based Cell Free Massive MIMO	94
7.1	System Model	95
7.1.1	Uplink Training	97

7.1.2	Downlink Payload Data Transmission	98
7.1.3	Uplink Payload Data Transmission	99
7.2	Proposed Angle information aided channel estimation for FDD systems	100
7.2.1	AoA Estimation Algorithm	100
7.2.2	Large Scale Fading Estimation	103
7.2.3	Performance Analysis	106
7.2.4	Angle Coherence Time	109
7.3	Proposed Beamforming and Combining Techniques	110
7.3.1	Angle-Based Beamforming	110
7.3.2	Angle-Based Combining	113
8	Power Control and AP selection For FDD-based Cell Free Massive MIMO	114
8.1	Spectral and Energy efficiency Analysis	115
8.1.1	Spectral Efficiency	115
8.1.2	Energy Efficiency	117
8.2	Proposed Max-Min Power control	118
8.2.1	Downlink Power Control	118
8.2.2	Uplink Weight Control	122
8.2.3	User-Centric (UC) AP Selection Method	122
8.3	Experimental Simulation Results	123
8.3.1	Experimental Setup and Parameters	123
8.3.2	Results and Discussions	125
8.4	Conclusion	132
9	Conclusions and Future Work	140
9.1	Conclusions	140
9.2	Open Research Directions and Future work	142
A	Proofs	146
A.1	Proof of Lemma 1	146
A.2	Proof of Proposition 1	147
A.2.1	Proof of Proposition 2	147
A.3	Proof of Corollary 1	148
A.4	Proof of Theorem 1	149
A.5	Proof of Lemma 2	149
A.6	Proof of Corollary 2	150
B	Abbreviations	151
C	Notations	155

List of Figures

3.1	A single-cell D2D underlaid cellular network. Two cellular users c_1 and c_2 establish a link with the eNB while several active D2D links are established in a disk centered at the eNB with radius R_C . For the case $m = 2$, a subset of active D2D links share resources with cellular UE c_1 (\star), while other D2D links share resources with c_2 (\blacktriangle).	22
3.2	The system model shows the channel model for one of the cellular users and a subset of active D2D links that share resources with c_1 . The active D2D links outside the cell are considered as out-of-cell D2D interference, whereas out-of-cell interference from cellular users belonging to cross-tier cells is ignored.	23
4.1	Analytical vs. simulated coverage probability for cellular and D2D users using (a) DPPC, and (b) EDPPC scheme.	45
4.2	Number of iterations for the SDDPC scheme for $\lambda = 5 \times 10^{-5}$ and different M channel allocations.	49
4.3	A snapshot of link geometry for a D2D underlaid cellular network assuming a sparse D2D link deployment scenario (i.e., $\lambda = 2 \times 10^{-5}$). D2D links in circles share resources with CUE c_1 , while D2D links in dashed circles share resources with CUE c_2	58
4.4	(a) Coverage probability for cellular and D2D users where resources are shared with 2 CUEs, using the proposed DPPC with variable ε . (b) Same as (a) but using the proposed EDPPC scheme. (c) Using the proposed EDPPC with variable μ	59
4.5	Coverage probability for cellular using all the proposed PC schemes in this work vs. that of [1,2]: (a) For cellular users in dense network scenario, (b) for cellular users in sparse network scenario.	60
4.6	Coverage probability for D2D users using all the proposed PC schemes in this work vs. that of [1, 2]: (a) for D2D users in dense network scenario, and (b) for D2D users in sparse network scenario.	61

4.7	Coverage probability for: (a) cellular, and (b) D2D users, for $M = 1, M = 2$, and $M = K$	62
4.8	Spectral efficiency (left axis) and power efficiency (right axis) for the proposed PC schemes in a dense network.	63
5.1	Multi-user MIMO NOMA system model	66
5.2	BER performance of proposed detectors in the multi-user scenario (dotted lines refer to the reference optimal power allocation scheme).	70
6.1	Uplink quantized massive MIMO system model	75
6.2	Uplink 1-bit quantized massive MIMO system model	76
6.3	Downlink quantized massive MIMO system model	82
6.4	Mutual information per user versus SNR for a $K \times N$ massive MIMO system where $K = 8, 16, 32$ users and $N = \{128, 256\}$ BS antennas.	89
6.5	Mutual information per user versus SNR for a $K \times N$ massive MIMO system where $K = 16$ users and $N = 128$ BS antennas and $b = \{1, 2, 3\}$ quantization bits; analytical versus simulated for the proposed MMSE-based detection with imperfect channel estimation.	90
6.6	A comparison of the total system throughput for a $K \times N$ quantized Massive MIMO where where $K = \{8, 16, 32\}$ users and $N = \{128, 256\}$ versus Conventional MIMO (8×8 and 16×16) systems.	91
6.7	Comparison of total system throughput for a $K \times N$ quantized b -bit UL massive MIMO with $K = \{16, 32\}$ users and $N = \{128, 256\}$ with imperfect channel estimation, vs. two conventional 8×8 and 16×16 MIMO systems.	92
6.8	Comparison of total system throughput for a $K \times N$ quantized b -bit DL massive MIMO with $K = 16$ users and $N = 128$ with imperfect channel estimation, vs. conventional 16×16 MIMO systems.	93
7.1	Cell-free massive MIMO system model	95
8.1	RMSE performance of the multipath component estimation versus SNR for $N = 32$ and $T = 16$ compared with the gradient-descent based estimation and subspace-based estimation.	125
8.2	Spectral efficiency of the proposed beamforming schemes versus SNR for $M = 10$ APs with $N = 32$ antennas and $K = 20$ users under imperfect channel estimation: (a) for DL, and (b) UL.	134
8.3	DL sum-rate of the proposed combining schemes versus (a) number of APs at SNR=10 dB for $MN = 320$ and $K = \{10, 20, 40\}$ users, and (b) versus number of antennas N at various SNR values for $M = 10$ APs and $K = 20$ users.	135

8.4	Spectral efficiency of the proposed combining schemes with equal power control, water-filling power control and the proposed max-min power control versus SNR for $M = 10$ APs, and $K = 20$ users for the Cell-Free (CF) massive MIMO (AP selection is not applied): (a) DL and (b) UL.	136
8.5	Same as Fig. 8.4 but applying the user centric (UC) AP selection scheme: (a) DL and (b) UL.	137
8.6	(a) Cumulative distribution of the spectral efficiency for all power control schemes with/without applying the proposed AP selection (CF/UC), and (b) DL energy efficiency of the proposed combining schemes with equal power control and max-min power control versus number of APs. Here, SNR=10 dB for $M = 10$, $N = 32$, and $K = 20$ users.	138
8.7	DL spectral efficiency versus multiple antenna configurations at the users for $K = \{10, 20, 40\}$, $M = 10$, and $N = 32$	139

List of Tables

3.1	System Parameters	27
4.1	Simulation Parameters	51
5.1	Simulation Parameters	72
7.1	System Parameters	100
8.1	Simulation Parameters	124

Chapter 1

Introduction

1.1 Network Densification Technologies

With the ever-increasing demand for better performance and higher throughput, network operators are struggling to meet the requirements for fast mobile data connectivity and more data traffic. From first generation (1G) to fourth generation (4G), the massive traffic growth has been handled by a combination of wider bandwidths, refined radio interfaces, and smaller cells [3–5]. As a result of this development, current cellular networks have reached their capacity limits, especially in highly populated metropolitan areas.

These escalating demands of mobile applications for massive network capacity have shaped the design of the upcoming fifth generation (5G) of mobile networks, which is expected to offer unprecedented levels of connectivity, quality of service (QoS) and $10\times$ more denser networks than 4G networks [5].

Moreover, early cell densification was achieved by deploying more macro base stations (BSs) (i.e., macro cellular densification). The main motivation

was to increase user capacity and achieve wider coverage. This approach was later expanded to include the use of smaller size stations with reduced coverage footprint. Micro, pico and small cells utilizing low transmission power and supporting a smaller number of users are easier to install and provide improved cost efficiency. A network incorporating these different cell sizes is known as a Heterogeneous Network (HetNet). HetNets have become the trend in spatial network densification allowing home users the ability to purchase small cell BSs and install them in indoor environments where received signal is weak.

However, the higher number of randomly deployed cells in HetNets carries with it many challenges such increased power consumption, overhead of transmitted signals, interference and overhead on the backhaul. Despite these challenges, the tremendous overall performance benefits obtained by network densification suggest their use will continue to grow and expand in upcoming future wireless networks. It is expected that network architectures employed in 5G will offer solutions to many of the current challenges faced by network operators relative to managing dense networks.

Therefore, network densification [5,6] has become as a key driver for enabling 5G through reusing spectral resources in device-to-device (D2D) communications and non-orthogonal multiple access (NOMA) systems, increasing the number of antennas per site in massive multiple-input and multiple-output (MIMO) systems, and deploying smaller and smaller cells in cell-free massive MIMO systems. Therefore, 5G densification can be accomplished in space, time and frequency dimensions [5]. However, managing interference remains one of the most challenging problems facing network densification. Problems intensify when BSs of different coverage footprints, access schemes, and transmission powers share the same licensed frequency spectrum. In addition, while network densification

is seen as an effective method of increasing system capacity and coverage, such gain comes at the expense of increased power consumption.

1.1.1 D2D Communication Technology

D2D communications is a network densification approach suggested to solve high-density cellular network challenges. D2D communication underlying cellular systems enables communication between devices in close vicinity with low latency and low energy consumption while offloading the telecommunication network from handling local traffic [7–11]. D2D is a promising approach to support proximity-based services such as social networking and file sharing [10]. When the devices are in close vicinity, D2D communication improves the spectral and energy efficiency of cellular networks [11]. Despite the benefits of D2D communications in underlay mode, interference management and energy efficiency have become fundamental requirements [12] in keeping the interference caused by the D2D users under control, while simultaneously extending the battery lifetime of the User Equipment (UE). For instance, cellular links experience cross-tier interference from D2D transmissions, whereas D2D links not only deal with the inter-D2D interference, but also with cross-tier interference from cellular transmissions. Therefore, power control (PC) and channel allocation (CA) have become necessary for managing interference levels, protecting the cellular UEs (CUEs), and providing energy-efficient communications.

1.1.2 NOMA Communication Technology

While orthogonal multiple access (OMA) schemes have traditionally dominated wireless communication standards [13–16], where wireless resources are allocated

for multiple users orthogonally in time, frequency, or code domains, the spectral efficiency remains low especially when resources are allocated to users with poor channel conditions.

NOMA [17–20] has been recently proposed as a network densification technology that enables multiple users with significantly different channel conditions to share resources simultaneously. This can be achieved through superposition coding (SC) at the transmitter, that is followed by successive interference cancellation (SIC) at the receiver. Proper user pairing criteria and power allocation policies can guarantee user fairness as well as affordable complexity overheads and signaling costs. NOMA is currently being celebrated as one of the main enabling technologies of the upcoming 5G of wireless mobile communication standards, which promises to connect billions of devices and achieve several gigabit-per-second data rates.

1.1.3 Massive MIMO Communication Technology

MIMO [21] technology is another popular approach to increase spectral efficiency and network capacity, which exploits the spatial dimension by adding more antennas. MIMO systems have been extensively studied over the past three decades. However, conventional MIMO configurations fall short of providing the requirements of 5G. Towards this end, *massive* MIMO has been introduced [22], in which few hundred antennas serve tens of terminals over the same time and frequency resources. However, equipping the base station (BS) with a large number of antenna elements dramatically increases the associated hardware cost and resulting power consumption of the radio-frequency (RF) circuits and data converters. It is known that the power consumption of analog-to-digital converters (ADCs) grows significantly with the number of quantization bits [23,24] and with

large sampling rates. One potential solution is the use low-resolution quantized massive MIMO (e.g., 1-bit ADCs) as a means of reducing costs and power consumption, and improving computational efficiency [24–30]. However, the main drawback of reducing the ADC resolution is the need to compensate for the severe non-linearity introduced by quantization, which might render traditional detection schemes highly sub-optimal.

1.1.4 Cell-Free Massive MIMO Communication Technology

Cell-free massive MIMO has recently been considered as a practical and useful embodiment of network MIMO that can potentially reduce inter-cell interference through coherent cooperation between base stations [31–34]. In cell-free massive MIMO, the serving antennas are distributed over a large area. Distributed systems can potentially provide higher coverage probability than co-located massive MIMO due to their ability to efficiently exploit diversity against shadow fading effects, at the cost of increased backhaul requirements [35]. According to [34], “cell-free” massive MIMO implies that, from a user perspective during data transmission, all access points (APs) cooperate to jointly serve the end-users; hence there are no cell boundaries and no inter-cell interference (ICI) in the data transmission. The APs are connected to a central processing unit (CPU) via a backhaul link. This approach, with simple signal processing, can effectively control ICI, leading to significant improvements in spectral and energy efficiency over the cellular systems [31–35]. The main challenge in deploying cell-free networks lies mainly in acquiring sufficiently accurate channel state information (CSI) so that the APs can simultaneously transmit (receive) signals to (from) all UEs and cancel interference in the spatial domain. The conventional approach

of sending downlink (DL) pilots and letting the UEs feed back channel estimates is unscalable since the feedback load is proportional to the number of APs. Therefore, to reduce the signaling overhead [36, 37], channel reciprocity can be exploited in time-division duplex (TDD) mode so that each AP only needs to estimate the uplink CSI.

An attractive alternative to consider is frequency-division duplexing (FDD) based cell-free massive MIMO systems for the following reasons: 1) channel reciprocity in TDD mode might not be accurate due to calibration errors in RF chains [38], 2) with the lack of downlink training symbols in TDD systems, users may not be able to acquire instantaneous CSI, and thus system performance will deteriorate in detecting and decoding the intended signals, 3) while TDD operation is preferable at sub-6 GHz massive MIMO, in millimeter wave (mmWave) bands FDD may be equally good since the angular parameters of the channel are reciprocal over a wide bandwidth [39], and 4) FDD systems dominate current wireless communications and have many benefits such as lower cost and greater coverage than TDD [40]. On the other hand, FDD-based cell-free massive MIMO systems still suffer from CSI acquisition and feedback overhead since the amount of downlink CSI feedback scales linearly with the number of antennas [41] and the number of APs in cell-free massive MIMO system. However, we can still benefit from 1) angle reciprocity, which holds true for FDD systems as long as the uplink and downlink carrier frequencies are not too far from each other (less than several GHz [42]), and 2) angle coherence time which is much longer than the conventional channel coherence time [43] where the channel angle information can be regarded as unchanged. Hence, angle information is essential in FDD-based cell-free massive MIMO systems. Therefore, a low complexity estimation approach that can efficiently estimate the angle information is required. In

addition, array signal processing schemes based on the estimated angle information are needed to enhance the overall spectral efficiency and energy efficiency.

1.2 Contributions and Outline

The purpose of this dissertation is to design efficient interference mitigation schemes for the aforementioned network densification technologies. Using theoretical analysis and empirical simulations, the proposed algorithms are proven to be high-performance and low-complexity solutions. The structure of this dissertation is as follows:

Chapter 2 covers the existing work related to the aforementioned network densification technologies in terms of power control and resource allocation schemes for D2D communication, detection and power control schemes for NOMA systems, low resolution detection for massive MIMO systems, and array signal processing schemes for cell free massive MIMO.

Chapter 3 considers a random network model for a D2D underlaid cellular system based on stochastic geometry. We propose a channel allocation scheme together with a set of three power control schemes to mitigate interference in a D2D underlaid cellular system modeled as a random network using the mathematical tool of stochastic geometry. The novel aspect of the proposed CA scheme is that it enables D2D links to share resources with *multiple* cellular users as opposed to one as previously considered in the literature. The coverage probability of D2D links and that of cellular links is studied and analyzed.

Chapter 4 considers the analysis of the proposed power control schemes for

the D2D underlaid cellular system. Moreover, it is shown that the accompanying distributed PC schemes further manage interference during link establishment and maintenance. The first two PC schemes compensate for large-scale path-loss effects and maximize the D2D sum rate by employing distance-dependent path-loss parameters of the D2D link and the base station, including an error estimation margin. The third scheme is an adaptive PC scheme based on a variable target signal-to-interference-plus-noise ratio, which limits the interference caused by D2D users and provides sufficient coverage probability for cellular users. Closed-form expressions for the coverage probability of cellular links, D2D links, and sum rate of D2D links are derived in terms of the allocated power, density of D2D links, and path-loss exponent. The impact of these key system parameters on network performance is analyzed and compared with previous work. Simulation results demonstrate an enhancement in cellular and D2D coverage probabilities, and an increase in spectral and power efficiency. This work has been published in [44–46].

Chapter 5 extends the study in Chapter 3 to consider efficient interference mitigation schemes for large MIMO-NOMA systems. We assume a large number of antennas on both, transmitting and receiving sides, and we propose clustering and power control schemes for a randomly distributed users in which users in each cluster are served on the same time-frequency resources and allocated different powers depending on their distance from a base station. Through special layer ordering and power allocation, we show that successive interference cancellation at stronger streams can be carried with minimal performance-complexity costs at the receiver side using detectors previously proposed in [47]. Simulations demonstrate that the proposed schemes are near-optimal compared to previous work.

Chapter 6 studies the uplink throughput achievable by a massive MIMO system in which the base station is equipped with a large number of low resolution analog-to-digital converters. We propose a new linear MMSE-based detector which accounts for the severe non-linearity effect of the low resolution quantization and incorporates a pilot-based channel estimation error. An analytical framework that derives the achievable rate of a MMSE-based detector in a massive MIMO configuration with the assumption that the front-end is limited to a 1-bit ADC and the pilot-based channel estimation error is presented. We compare the capacity of a massive MIMO system using a 1-bit ADC and a linear detector against a conventional MIMO system with higher-order modulation and near maximum likelihood (ML) detection. We show that in the low SNR regime with channel estimation error, the quantized massive MIMO system can outperform the conventional large MIMO system; however for high SNR, the conventional MIMO system with a near ML detector can outperform the quantized massive MIMO system. This work has been published in [48, 49].

Chapter 7 considers FDD-based cell-free massive MIMO in which distributed multi-antenna access points serve many single-antenna users simultaneously. Most prior work on cell-free massive MIMO systems assume time-division duplexing mode, although FDD systems dominate current wireless standards. The key challenges in FDD massive MIMO systems are CSI acquisition and feedback overhead. To address these challenges, we exploit the so-called angle reciprocity of multipath components in the uplink and downlink, so that the required CSI acquisition overhead scales only with the number of served users, and not the number of AP antennas nor APs. We propose a low complexity multipath component estimation technique and present linear angle-of-arrival (AoA)-based beamforming/combining schemes for FDD-based cell-free massive MIMO systems.

We analyze the performance of these schemes by deriving closed-form expressions for the mean-square-error of the estimated multipath components, as well as expressions for the uplink and downlink spectral efficiency.

Chapter 8 continues the work done in Chapter 7 and considers a max-min power allocation problem that maximizes the minimum user rate under per-user power constraints, using semi-definite programming. Furthermore, we present a user-centric (UC) AP selection scheme in which each user chooses a subset of APs to improve the overall energy efficiency of the system. Simulation results demonstrate that the proposed multipath component estimation technique outperforms conventional subspace-based and gradient-descent based techniques. We also show that the proposed beamforming and combining techniques along with the proposed power control scheme substantially enhance the spectral and energy efficiencies with an adequate number of antennas at the APs. This work has been published in [50, 51].

Chapter 9 concludes the dissertation and specifies future directions.

1.3 Publications and Awards

1.3.1 Thesis Related

At the time of writing, this research work has been incrementally published in prestigious journal papers and conference papers as follows:

Journals:

- Journal paper in preparation: A.Abdallah, and M. M. Mansour, “Survey on Array Signal Processing for Massive MIMO systems”.

- Journal paper in preparation: H. Sareddeen, A. Abdallah, and M. M. Mansour, “Sub-Space Detection for Single and Multi-User Large MIMO-NOMA”.
- A. Abdallah and M. M. Mansour, “Efficient Angle-Domain Processing for FDD-based Cell-free Massive MIMO Systems,” in *IEEE Transactions on Communications*, pp. 1-1, 2020.
- A. Abdallah, M. M. Mansour and A. Chehab, “Power Control and Channel Allocation for D2D Underlaid Cellular Networks,” in *IEEE Transactions on Communications*, vol. 66, no. 7, pp. 3217-3234, July 2018.
- A. Abdallah, M. M. Mansour, L. M. A. Jalloul and A. Chehab, “When Quantized Massive MIMO Meets Large MIMO With Higher Order Modulation,” in *IEEE Communications Letters*, vol. 22, no. 12, pp. 2599-2602, Dec. 2018.

Conference papers:

- A. Abdallah and M. M. Mansour, “Angle-Based Multipath Estimation and Beamforming for FDD Cell-free Massive MIMO,” in *Proc. IEEE Int. Sig. Process. Advances in Wireless Communication. Workshop (SPAWC)*, Cannes, France, July. 2019.
- A. Abdallah, M. M. Mansour, A. Chehab and L. Jalloul, “MMSE Detection for 1-bit Quantized Massive MIMO with Imperfect Channel Estimation”, in *Proc. IEEE Int. Sig. Process. Advances in Wireless Communication. Workshop (SPAWC)*, Kalamata, Greece, March. 2018.
- A. Abdallah, M. M. Mansour and A. Chehab, “Joint channel allocation and power control for D2D communications using stochastic geometry,” in *Proc.*

IEEE Wireless Communications and Networking Conference (WCNC), Barcelona, 2018, pp. 1-6.

- A. Abdallah, M. M. Mansour and A. Chehab, “A Distance-Based Power Control Scheme for D2D Communications Using Stochastic Geometry,” in *Proc. IEEE Vehicular Technology Conference (VTC-Fall)*, Toronto, ON, 2017, pp. 1-6.

1.3.2 Non-Thesis Related

- A. Abdallah and S. Doumiati, “Hybrid Precoding for Device-to-Device Communication at MmWave Frequencies,” in *Proc. European Wireless Conference (EW)*, Oulu, Finland, 2016, pp. 1-6.
- A. Abdallah, D. Serhal and K. Fakhri, “Relaying Techniques for LTE-Advanced,” in *Proc. of European Wireless Conference (EW)*, Budapest, Hungary, 2015, pp. 1-6.

1.3.3 Awards

In recognition of my research efforts during my Ph.D. journey, I received the CNRS-L/AUB doctoral scholarship award from the Lebanese National Council for Scientific Research (CNRS), Sept. 2018.

Chapter 2

Literature Review

The aim of this chapter is to review the state-of-the-art for the interference mitigation techniques that are applied in D2D, NOMA, massive MIMO, and cell-free massive MIMO systems. The related work covers power control and resource allocation schemes for D2D communication, detection and power control schemes for NOMA systems, low resolution detection for massive MIMO systems, and array signal processing schemes for cell free massive MIMO.

2.1 Power Control and Resource Allocation in D2D Communications

Power control and channel allocation schemes have been presented in the literature as strategies to mitigate interference in D2D wireless networks [1, 2, 52–66]. In [52], open loop PC (OLPC) and closed loop PC schemes (CLPC), used in LTE [67], are compared with an optimization based approach aimed at increasing spectrum usage efficiency and reducing total power consumption. However, such

schemes require a large number of iterations to converge.

In [53–56], a power allocation scheme is presented based on a “soft dropping” PC algorithm, in which the transmit power meets a variable target signal-to-interference-plus-noise ratio (SINR). However, the system considered is not random, and the D2D users in [54–56] are confined within a hotspot in a cellular region.

In [57], a D2D “mode” is selected in a device based on its proximity to other devices and to its distance to the eNB. However, the inaccuracy of distance derivation is a key aspect that is not addressed in [57]. In [59], a two-phase auction-based algorithm is used to share uplink spectrum. The authors assume that all the channel information is calculated at the eNB and broadcasted to users in a timely manner, which will cause an excessive signaling overhead. In [60], a heuristic delay-tolerant resource allocation is presented for D2D underlying cellular networks; however, power control is ignored since D2D users always transmit at maximum power.

In the above schemes, power control and channel allocation methods [52–56, 59, 60, 65, 66] are developed and evaluated assuming deterministic D2D link deployment scenarios. On the other hand, PC in [1] is presented for unicast D2D communications by modeling a random network for a D2D underlaid cellular system, using stochastic geometry. D2D users are distributed using a (2-dimensional) spatial Poisson point process (PPP) with density λ . Stochastic geometry is a useful mathematical tool to model irregular spatial structures of D2D locations, and to quantify analytically the interference in D2D underlaid cellular networks using the Laplace transform [68–70]. Two PC schemes are developed in [1]; a centralized PC and a simple distributed on-off PC scheme. The former requires global channel state information (CSI) possibly at a centralized controller, which may incur high CSI feedback overhead, whereas the latter is based on a decision set and requires

only direct link information. However, the authors assume a fixed distance between the D2D pairs, and that the D2D devices for the distributed case operate at maximum power leading to severe co-channel interference. Moreover, the distributed PC scheme of [1] does not guarantee reliable cellular links, especially at high SINR targets. In [2], similar PC algorithms to [1] are presented but with channel uncertainty considered; the results in [1] are regarded as ideal best-case scenarios with perfect channel knowledge. In [61, 62], a framework based on stochastic geometry to analyze the coverage probability and average rate with different channel allocations in a D2D overlaid cellular systems is presented.

In [63], PC and resource allocation schemes are considered; however, the interference between D2D pairs is ignored. In [64], a transmission cost minimization problem using hypergraph model is investigated based on a content encoding strategy to download a new content item or repair a lost content item in D2D-based distributed storage systems. Moreover, [64] considers the one-to-one matching case, in which only one D2D link shares resources with only one uplink cellular user. In [65, 66], resource allocation is considered where one D2D link shares resources with only one cellular user in the underlay case. Obviously, these schemes in [63–66] are not spectrally efficient because D2D pairs are restricted to use different resource allocations. In [71, 72], power control is studied in random ad hoc networks without taking into consideration the underlaid cellular network.

2.2 Detection and Power Control in MIMO-NOMA systems

The combination of MIMO and NOMA (MIMO-NOMA) [73–82] is an inevitable extension to both technologies, that has the potential to improve spectral effi-

ciency and achieve high data rates, dense coverage, massive connectivity and low latency, all of which are major requirements of 5G. MIMO-NOMA configurations can be single-cluster or multi-cluster. In a single-cluster setting, all users, except one, conduct SIC. In a multi-cluster setting, users are first partitioned into different clusters to reduce interference, and SIC follows. The full potential of MIMO-NOMA is achieved by the joint optimization of user clustering, beamforming, power allocation, and SIC. In [74], an ergodic capacity maximization problem is studied for Rayleigh fading MIMO-NOMA with statistical channel state information (CSI) at the transmitter. Both, optimal and low complexity power allocation schemes were used to maximize the ergodic capacity, with total transmit power constraint and minimum rate constraint over weak users. Whereas in [75], fairness, weighted sum rate, sum rate with quality of service constraints, and energy efficiency maximizations are considered, and the matching algorithm is employed to jointly optimize channel assignment and power allocation.

Several MIMO-NOMA-specific digital signal processing designs have been presented for precoding and detection. Joint clustering and precoding is achieved in [76] by using eigenspaces of channel matrices, to eliminate inter-cluster interference and enhance sum capacity. In [77, 78], user pairing and the design of precoding and detection matrices for downlink transmissions are studied, where the performance is analyzed in terms of outage probabilities and diversity orders. In [79], downlink minimum Euclidean distance precoders are presented by combining methodologies previously developed for unicast and multicast MIMO scenarios. In [80], minorization-maximization based hybrid precoding is presented, where user clustering and power allocation pair two suitable users in a group. Furthermore, an iterative linear minimum mean square error (MMSE) uplink detector is proposed in [81], and a Gaussian message passing iterative detector is proposed

in [82]. The latter converges faster when the number of users is greater than the number of serving antennas.

MIMO performance is largely determined by the detection scheme at the receiver side; various schemes provide different performance-complexity trade-offs [83]. Linear detectors, such as zero forcing (ZF) and minimum mean square error (MMSE), are the least-complex, but the least-optimal as well. On the other hand, maximum likelihood (ML) detectors are optimal but most computationally intensive. Several sub-optimal detectors fill the spectrum in between, including sphere decoders (SD) and their variants [84,85]. While in massive MIMO systems linear detectors achieve near-optimal performance by exploiting the channel hardening effect [86], for large MIMO systems, the detection schemes in the literature are grouped into several areas: detection based on local search [87]; detection based on meta-heuristics [88]; detection via message passing on graphical models [89]; lattice reduction (LR) aided detection [90]; and detection using Monte Carlo sampling [91]. However, for these schemes to achieve a near-ML performance with high orders of antennas and modulation constellations, the entailed complexity would be prohibitive.

A popular family of MIMO detectors that achieves good performance-complexity trade-offs employs non-linear subset-stream detection. The nulling-and-cancellation (NC) detector [92] is a low-complexity member of this family; it consists of linear nulling followed by back-substitution and slicing over layers. The chase detector (CD) [93] is a more complex member of this family; it first creates a list of candidate decision vectors, and then chooses the best candidate from this list as a final decision. Furthermore, the layered orthogonal lattice detector (LORD) [94] is an even more complex detector that consists of several iterations of CD. All aforementioned subset-stream detectors make use of QR decomposition (QRD).

Other popular subset-stream detectors exist (e.g., [95–97]), that decompose the channel matrix into lower order sub-channels to reduce the number of jointly detected streams. A less complex alternative [47, 98–100] is to decompose the channel matrix via a punctured QRD, WR decomposition (WRD).

2.3 Low Resolution Detection in Massive MIMO

Prior work has studied the case of uplink quantized massive MIMO [24–27], and analyzed the non-linearity effects of quantization. However, there has not been any comparison of achievable rates of the 1-bit uplink massive MIMO with that of a conventional MIMO system employing higher-order modulation (e.g., 1024-QAM) schemes. In addition, linear detectors such as ZF, match filtering, and maximal ratio combining (MRC) have been previously analyzed in [24] for the uplink massive MIMO with 1-bit ADCs. However, linear MMSE detection, that accounts for the non-linearity effect of the low resolution ADCs, has not been analyzed in previous work. In [101, 102] the gradient projection algorithm is used to iteratively find a precoder that minimizes the mean square error (MSE) between the transmitted and the received signal for the downlink case, but [101, 102] contain no mathematical analysis of the achievable rate.

2.4 Array Signal Processing in Cell Free Massive MIMO

There has been considerable interest, in only TDD mode, cell-free massive MIMO systems [31–35, 103]. In [31], a cell-free system is considered and algorithms

for power optimization and linear precoding are analyzed. Compared with the conventional small-cell scheme, cell-free massive MIMO can yield more than ten-fold improvement in terms of outage rate. While in [32], the APs perform multiplexing/de-multiplexing through conjugate beamforming in the downlink and matched filtering in the uplink.

In [33], a cell-free massive MIMO downlink is considered, wherein a large number of distributed multiple-antenna APs serve many single-antenna users. A distributed conjugate beamforming scheme is applied at each AP via the use of local CSI. Spectral efficiency and energy efficiency are studied while considering channel estimation error and power control.

In [103, 104], cell-free and user-centric architectures at mmWave frequencies are considered. A multiuser clustered channel model is introduced, and an uplink multiuser channel estimation scheme is described along with hybrid analog/digital beamforming architectures. Moreover, in [104], the non-convex problem of power allocation for downlink global energy efficiency maximization is addressed. In [105], an uplink TDD-based cell-free massive MIMO system is considered. Geometric programming GP is used to sub-optimally solve a quasi-linear max–min signal-to-interference-and-noise ratio (SINR) problem.

Angle estimation has been studied in other wireless networks without considering cell-free massive MIMO networks (see e.g. [106–115]). For instance, subspace-based angle estimation algorithms, such as multiple signal classification (MUSIC), estimation of signal parameters via rotational invariance technique (ESPRIT) and their extensions have gained interest in the array processing community due to their high resolution angle estimation capability [106–108]. Their applications in massive MIMO systems and MIMO systems for angle estimation have been presented in [109–112]. Unfortunately, the classical MUSIC and ESPRIT schemes

are not suitable for mmWave communications due to the following main reasons:

- 1) They have high computational complexity mainly due to the singular value decomposition (SVD) operation on channels with massive number of antennas;
- 2) They are considered as blind estimation techniques originally targeted for radar applications, and do not make full use of training sequences in wireless communication systems.

In [113–115], an angle-of-arrival (AoA) estimation scheme for mmWave massive MIMO systems with a uniform planar array at the base station is presented. The initial AoAs of each uplink path are estimated through the two dimensional discrete Fourier transform (2D-DFT), and then the estimation accuracy is further enhanced via an angle rotation technique. The AoA estimation scheme in [113–115] does not consider the cell-free massive MIMO network and ignores the large scale fading estimation. Moreover, in order to apply efficient beamforming and combining techniques, large scale fading estimation is crucial in FDD-based cell free massive MIMO system. Hence in this work, we further extend the estimation scheme in [113–115] to consider FDD-based cell-free massive MIMO system and estimate both AoA and large scale fading coefficients. In addition using the estimated AoA and the large scale fading, we apply low complexity angle-based beamforming/combining in downlink and uplink directions.

In [116], a multipath component estimation technique and base station cooperation scheme based on the multipath components for the FDD-based cell-free massive MIMO systems are presented. However, no closed form expression of the MSE of the considered multipath estimation is presented.

Chapter 3

Channel Allocation and Coverage Probability Analysis for D2D Underlaid Cellular Systems

In this chapter, we propose channel allocation and analyze the performance assuming a random D2D underlaid cellular network model. A main shortcoming in most papers in the literature is that unrealistic assumptions are considered. For instance, in [1, 2] the authors rely on deterministic values such as fixed distance between the D2D transmitter and receiver, fixed transmission power, and fixed SINR targets and they only consider one cellular user sharing the resources with the D2D links. These deterministic assumptions simplify the derivation of the analytical models, but are in many cases unrealistic. In our work, we study a general scenario by randomly modeling the distance between the D2D pairs, assigning different transmission power to D2D links, varying the SINR targets, and consider multiple cellular users sharing the resources with the D2D links. Therefore, the presented analytical expressions in this work give more insight into the performance of a D2D underlaid cellular system in a rather more realistic

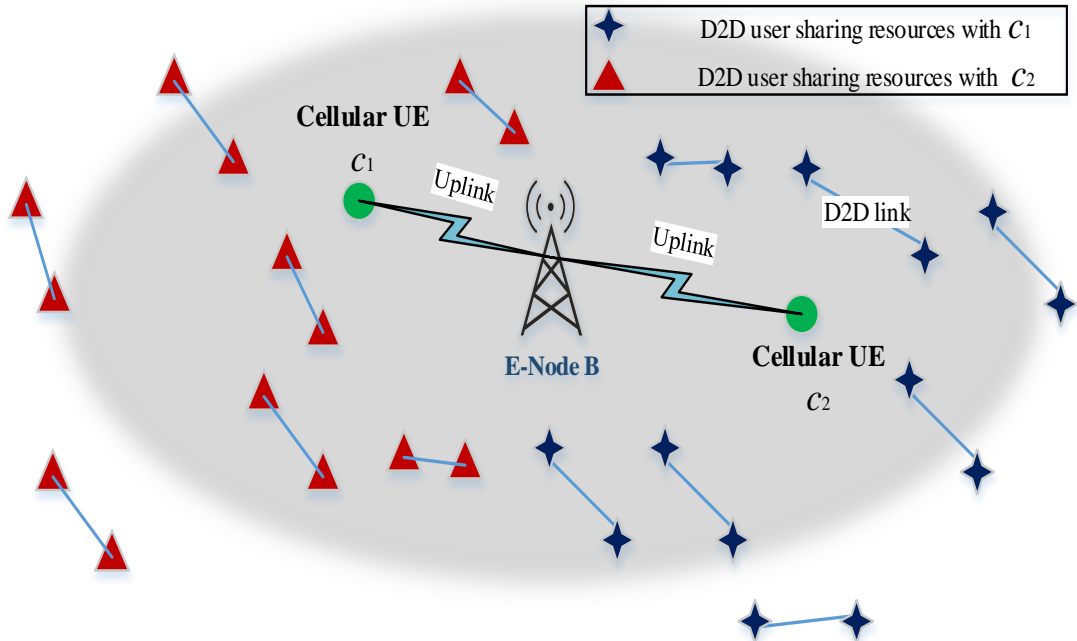


Figure 3.1: A single-cell D2D underlaid cellular network. Two cellular users c_1 and c_2 establish a link with the eNB while several active D2D links are established in a disk centered at the eNB with radius R_C . For the case $m = 2$, a subset of active D2D links share resources with cellular UE c_1 (\star), while other D2D links share resources with c_2 (\blacktriangle).

approach. The corresponding results appeared in [44–46].

3.1 D2D System Model

In this section, the system model and the corresponding network parameters are presented. As shown in Fig. 3.1, we study a D2D underlaid cellular network in which a pool of K active D2D users is divided into M groups such that each group shares distinct resources with one of M cellular users, as opposed to the assumption taken in [1, 2] where all the K D2D users share the same resource with *one* cellular user. The e-Node B (eNB) coverage region is modeled as a circular disk \mathcal{C} with radius R_C and centered at the eNB. We assume that two

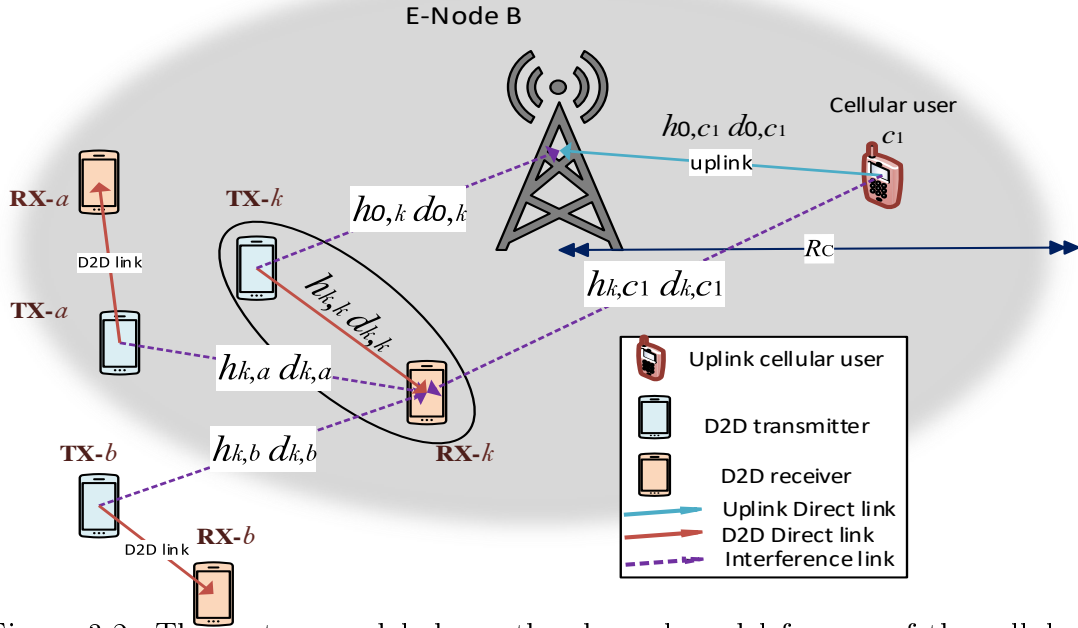


Figure 3.2: The system model shows the channel model for one of the cellular users and a subset of active D2D links that share resources with c_1 . The active D2D links outside the cell are considered as out-of-cell D2D interference, whereas out-of-cell interference from cellular users belonging to cross-tier cells is ignored.

cellular users are uniformly distributed in this disk, while the D2D transmitters are distributed in the whole \mathbb{R}^2 plane by the homogeneous PPP Φ with density λ , where $\mathbb{P}[\Phi = n] = \exp(-\lambda) \frac{\lambda^n}{n!}$. The PPP assumption corresponds to having the expected number of nodes per unit area equal to λ , and the nodes being uniformly distributed in the area of interest. Hence, the number of D2D transmitters in \mathcal{C} is a Poisson random variable K with mean $\mathbb{E}[K] = \lambda\pi R_C^2$. In addition, the associated D2D receiver is uniformly distributed in a disk centered at its transmitter with radius R_D .

We consider a particular realization of the PPP Φ and a transmission time interval (TTI) t to describe the system model. In the following, we use subscript 0 to refer to the uplink signal received by the eNB, c_m to refer to the m th transmitting cellular user, and $k \neq 0$ to refer to the k th D2D user. Denote

by $s_{0,c_m}^{(t)}$ the signal transmitted by the m th cellular user in the uplink, and by $s_{k,k}^{(t)}$ the signal transmitted by the k th D2D *transmitter* to its k th D2D *receiver*, during the TTI t . We assume distance-independent Rayleigh fading channel models between the eNB and the UEs, between the eNB and the D2D users, and between the D2D users themselves. Let $h_{0,c_m}^{(t)}$ denote the uplink channel gain between the m th cellular user and eNB, $h_{k,k}^{(t)}$ the direct link channel gain between the k th D2D *transmitter* (TX) and corresponding k th D2D *receiver* (RX), $h_{0,k}^{(t)}$ the channel gain of the interfering link from the k th D2D TX to the eNB, $h_{k,c_m}^{(t)}$ the channel gain of the interfering link from the m th cellular UE to the k th D2D RX, and $h_{k,l}^{(t)}$ the lateral channel gain of the interfering link from the l th D2D TX to the k th D2D RX. Random variables n_0 and n_k denote additive noise at the eNB and the k th D2D RX, and are distributed as $\mathcal{CN}(0, \sigma^2)$, where σ^2 is the noise variance. We also assume a distance-dependent path-loss model, i.e., a factor of the form $d_{k,l}^{-\alpha}$ that modulates the channel gains, where $d_{k,l}$ represents the distance between the l th TX and the k th RX, with α being the path-loss exponent.

Moreover, we assume that each cellular user and a subset $K' < K$ of the D2D transmitters share the same uplink physical resource block (PRB) during the same TTI (t) as depicted in Fig. 3.2. Furthermore, we assume that the channel coherence bandwidth is larger than the bandwidth of a PRB, leading to a flat fading channel over each PRB. Therefore, the received signals $y_{k,k}^{(t)}$ at the k th D2D *receiver*, and $y_{0,c_m}^{(t)}$ at the eNB can be expressed as

$$y_{k,k}^{(t)} = h_{k,k}^{(t)} d_{k,k}^{(t)-\alpha/2} s_{k,k}^{(t)} + \sum_{l=1, l \neq k}^{K'} h_{k,l}^{(t)} d_{k,l}^{(t)-\alpha/2} s_{k,l}^{(t)} + n_k^{(t)}, \quad (3.1)$$

$$y_{0,c_m}^{(t)} = h_{0,c_m}^{(t)} d_{0,c_m}^{(t) -\alpha/2} s_{0,c_m}^{(t)} + \sum_{k=1}^{K'} h_{0,k}^{(t)} d_{0,k}^{(t) -\alpha/2} s_{k,k}^{(t)} + n_0^{(t)}. \quad (3.2)$$

The transmit powers ρ_0 and ρ_k are conditioned to meet certain peak power constraints, i.e. $\rho_0 \triangleq |s_{0,c_m}|^2 \leq P_{\max,C}$ and $\rho_k \triangleq |s_{k,k}|^2 \leq P_{\max,D}$ for all links. The channel gains are estimated at each D2D receiver using the reference signal received power (RSRP), and are fed back to the corresponding D2D transmitter. In addition, it is worth noting that $\mathbb{E}[K]$ represents the average number of D2D links (or transmitters) before channel allocation, whereas $\mathbb{E}[K']$ represents the number of D2D links (or transmitters) sharing resources with c_m .

The SINR of any typical link is defined as $\text{SINR} \triangleq \frac{W}{I + N}$, where W represents the power of the intended transmitted signal, I represents the power of the interfering signals, and N denotes the noise power. Therefore, the SINR at the eNB and D2D receiver k can be written as

$$\text{SINR}_0(K', \boldsymbol{\rho}) = \frac{\rho_0 |h_{0,c_m}|^2 d_{0,c_m}^{-\alpha}}{\sum_{k=1}^{K'} \rho_k |h_{0,k}|^2 d_{0,k}^{-\alpha} + \sigma^2}, \quad (3.3)$$

$$\text{SINR}_k(K', \boldsymbol{\rho}) = \frac{\rho_k |h_{k,k}|^2 d_{k,k}^{-\alpha}}{\sum_{i \neq 0,k}^{K'} \rho_i |h_{k,i}|^2 d_{k,i}^{-\alpha} + \rho_0 |h_{k,c_m}|^2 d_{k,c_m}^{-\alpha} + \sigma^2}, \quad k > 0 \quad (3.4)$$

where $\boldsymbol{\rho} = [\rho_0, \rho_1, \dots, \rho_k]^T$ represents the transmit power profile vector, with ρ_i being the transmit power of the i th UE transmitter, and K' is the number of D2D transmitters. The super-subscript (t) is suppressed for simplicity.

The proposed system model ignores the out-of-cell interference transmission from other uplink users from cross-tier cells. However, the density of the D2D links is a network parameter that captures the expected interference on cellular and D2D links. Moreover, when the density of the D2D links is high, the proposed system is able to capture the effect of the dominant interferer for both cellular

(uplink) and D2D links, since there is a high probability that the nearest D2D interferer would become the dominant interference of a D2D link and that of the cellular link. Furthermore, when this network parameter is high, it can provide an upper bound on the performance of a D2D underlaid cellular network with out-of-cell interference. In addition, one can note that the radius of the disk R_C is large enough to encompass all the D2D pairs, since the dominant interference is generated from the nearest D2D interferers.

Based on the above defined SINRs, we use the coverage probability and achievable sum rate as metrics to evaluate system performance. Precisely, the proposed CA and PC algorithms aim to maximize those quantities while maintaining a minimum level of Quality-of-Service (SINR threshold β). The coverage probabilities of both the cellular link and D2D links are derived in this work. The cellular coverage probability $\bar{\mathcal{P}}_{\text{cov,C}}(\beta_0)$ is defined as

$$\bar{\mathcal{P}}_{\text{cov,C}}(\beta_0) = \mathbb{E}[\mathcal{P}_{\text{cov,C}}(\boldsymbol{\rho}, \beta_0)] = \mathbb{E}[\mathbb{P}(\text{SINR}_0(K', \boldsymbol{\rho}) \geq \beta_0)], \quad (3.5)$$

where β_0 denotes the minimum SINR value for reliable uplink connection. Similarly, the D2D coverage probability $\bar{\mathcal{P}}_{\text{cov,D}}(\beta_k)$ is defined as

$$\bar{\mathcal{P}}_{\text{cov,D}}(\beta_k) = \mathbb{E}[\mathcal{P}_{\text{cov,D}}(\boldsymbol{\rho}, \beta_k)] = \mathbb{E}[\mathbb{P}(\text{SINR}_k(K', \boldsymbol{\rho}) \geq \beta_k)], \quad (3.6)$$

where β_k denotes the minimum SINR value for a reliable D2D link connection. In addition, the ergodic sum rate of D2D links is defined as

$$\mathcal{R}_s^{(D)} = \mathbb{E} \left[\sum_{k=1}^{K'} \log_2 (1 + \text{SINR}_k(K', \boldsymbol{\rho})) \right]. \quad (3.7)$$

The main system parameters are summarized in Table 3.1.

Table 3.1: System Parameters

Cell radius	R_C
PPP of all D2D users in the cell	Φ
PPP of all D2D users in the cell after channel allocation	Φ'
Density of D2D links (D2D/ m^2)	λ
Channel gain from the cellular UE c_m to eNB	h_{0,c_m}
Channel gain from D2D TX k to D2D RX k	$h_{k,k}$
Channel gain from D2D TX k to eNB	$h_{0,k}$
Channel gain from the cellular UE c_m to D2D RX k	h_{k,c_m}
Channel gain from D2D TX l to D2D RX k	$h_{k,l}$
Distribution of channel fading ($h_{x,y}$)	Rayleigh fading $ h_{x,y} ^2 \sim \exp(1)$
Distance between D2D links ($d_{k,k}$)	Uniformly distributed
Distance between uplink user and eNB (d_{0,c_m})	Uniformly distributed
Distance between D2D TX k and eNB ($d_{0,k}$)	Uniformly distributed
Expectation of an event	$\mathbb{E}[\cdot]$
Probability of an event	$\mathbb{P}[\cdot]$
Laplace transform of a variable X	\mathcal{L}_X
Coverage probability of link L	$\mathcal{P}_{\text{cov},L}$
Transmit probability	\mathcal{P}_{tx}
Ergodic sum rate of D2D links	$\mathcal{R}_s^{(D)}$
Maximum transmit power for cellular user	$P_{\text{max},C}$
Maximum transmit power for D2D user	$P_{\text{max},D}$
Receiver sensitivity (dBm)	ϱ_{rx}
Cumulative distribution function (cdf) of variable X	$F_X(\cdot)$
Probability density function (pdf) of variable X	$f_X(\cdot)$

3.2 Proposed Channel Allocation Scheme

In this section, we propose a channel allocation scheme that enables active D2D users to share the same resource blocks used by $M > 1$ (two or more) cellular UEs (CUEs). Its main objective is to decrease the density of D2D users sharing the same resource with a particular cellular user by dividing all active D2D pairs into M groups, such that each group shares resources with one of M distinct CUEs. By this, we further extend the system model in [1, 2], where only the case $M=1$ is considered and all the active D2D pairs are assumed to share resources with only one CUE. However, we include in our study a new resource allocation scheme for $M > 1$.

Initially, mode selection determines whether a D2D pair can transmit in D2D mode or in cellular mode, and time and/or frequency resources are allocated accordingly. For simplicity, we study the case of two CUEs ($M = 2$); the same approach is also generalized for any M . Using the independent thinning property [117], we independently assign random binary marks $\{1, 2\}$ to the subset of active D2D users that can share resources with cellular users c_1 and c_2 , respectively. The assignment is based on the following criterion: when the distance between the cellular UE c_1 and the k th D2D RX is greater than the distance between cellular c_2 and the k th D2D RX ($d_{k,c_1} > d_{k,c_2}$), the k th D2D TX at instant (t) will be assigned the value $\{1\}$; otherwise the D2D TX will be assigned $\{2\}$. Consequently, all D2D users assigned with value $\{1\}$ will share the same resources as c_1 , while the rest will share the same resources as c_2 . Therefore, sharing resources with the farthest cellular user reduces the interference at the eNB by decreasing the density of the D2D TXs sharing the same resources, and reduces the interference generated from the cellular user at the D2D RXs.

Remark 1. Independent thinning of a PPP alters the density of the point process. If we independently assign random binary marks $\{1, 2\}$ with $\mathbb{P}[Q_k = 1] = q$ and $\mathbb{P}[Q_k = 2] = 1 - q$ to each point in a PPP and collect all the points which are marked as 1, the new point process will be a PPP Φ' but with density $q\lambda$, while the remaining points marked as 2 will have a PPP Φ'' with density $(1 - q)\lambda$. In our case, the arrival of D2D users such that $d_{k,c_1} > d_{k,c_2}$ is independent of the arrival of another pair of D2D users such that $d_{k,c_2} > d_{k,c_1}$. Hence the thinning property applies.

Lemma 1. *Using the above remark, half of the active D2D users will share the same resources with one of the cellular users and the other half will share them with the other cellular user.*

Proof. The proof relies on the pdf of the distance between two uniformly distributed points, which is given by [118]:

$$f_{d_{k,c_m}}(r) = \frac{2r}{R_C^2} \left(\frac{2}{\pi} \cos^{-1} \left(\frac{r}{2R_C} \right) - \frac{r}{\pi R_C} \sqrt{1 - \frac{r^2}{4R_C^2}} \right), \quad 0 \leq r \leq 2R_C. \quad (3.8)$$

Using (3.8), we have $\mathbb{P}[Q_k = 1] = q = \frac{1}{2}$. See detailed proof in Appendix A.1. A similar approach can be applied for a more general case of M CUEs. A D2D UE shares resources with the CUE that is furthest away from it. For instance, if resources are shared with M CUEs, then after $M - 1$ comparisons, $\mathbb{P}[d_{k,c_m} \geq \max_{n \neq m} \{d_{k,c_n}, \dots, d_{k,c_M}\}] = \mathbb{P}[Q_k = \text{value assigned to } c_m] = q_k = \frac{1}{M}$, where $\sum_i^M q_i = 1$. \square

We show in Section 3.3 that the coverage probabilities for cellular and D2D links depend on the density of the D2D users sharing the same resource. With the proposed CA scheme, the density of the D2D users is decreased by a factor of $q < 1$ to be $q\lambda$. Therefore, the interference at the eNB is further reduced compared to the scenario considered in [1], because here a smaller number of D2D users ($\mathbb{E}[K'] = \frac{\mathbb{E}[K]}{M} = \frac{1}{M} \lambda \pi R_C^2$) share the same resources with the each CUE.

It should be noted that sharing resources with more than one CUE increases the coverage probability, which is intuitive as the interference caused by the D2D links is reduced. However, upon increasing M (implying decreasing K'), the spectral efficiency of the system will decrease according to (3.7), and hence we would lose one of the main advantages of D2D communications that is increasing the spectral efficiency of the cellular system. Therefore, a trade-off exists between enhancing the link coverage probability and increasing the system throughput.

In addition, the complexity of the proposed channel allocation is $O(MK)$

where K is the total number of the D2D links that will share resources with $(M > 1)$ uplink cellular users. This is due to the fact that the base station will compute, for each D2D link, the distance (d_{k,c_m}) from the k th D2D receiver to the all M cellular users (where $0 < k \leq K$ and $1 < m \leq M$). Therefore, the base station computes a total of MK distance parameters (d_{k,c_m}) to perform the comparisons $(d_{k,c_m} \geq \max_{n \neq m} \{d_{k,c_n}, \dots, d_{k,c_M}\})$ as discussed above.

3.3 Analysis of Coverage Probability

In this section, the cellular and D2D coverage probabilities are derived using the tool of stochastic geometry. In order to analyze the coverage probabilities, the transmit powers ρ_k of the D2D transmitters are assumed to be i.i.d. with cdf $F_{\rho_k}(\cdot)$, $k = 1, \dots, K'$, and the transmit power ρ_0 of the uplink cellular user is independent having distribution $F_{\rho_0}(\cdot)$.

3.3.1 Cellular Link Coverage Probability

Based on the system model and assuming that the eNB is located at the origin, the SINR of the uplink is given by (3.3). We are interested in the cellular coverage probability $\bar{\mathcal{P}}_{\text{cov,C}}(\beta_0)$, which is the probability that the SINR of cellular link is greater than a minimum SINR β_0 for a reliable uplink connection as defined (3.5). Using Lemma 1, we derive an analytical expression for the coverage probability of a cellular link.

Proposition 1. *The cellular coverage probability is given by*

$$\bar{\mathcal{P}}_{\text{cov,C}}(\beta_0) = \mathbb{E}_X \left[e^{-a_1 X - \theta_0 X^{2/\alpha}} \right], \quad (3.9)$$

where $a_1 = \beta_0 \sigma^2$, $\theta_0 = \frac{\pi \mathbb{P}[Q_k=1] \lambda \beta_0^{2/\alpha}}{\text{sinc}(2/\alpha)} \mathbb{E}[\rho_k^{2/\alpha}]$, and $X = d_{0,c_m}^\alpha \rho_0^{-1}$ is a random variable with cdf

$$F_X(x) = \int F_{d_{0,c_m}}(x^{1/\alpha} p^{1/\alpha}) dF_{\rho_0}(p).$$

Proof. See Appendix A.2. □

One can note that the SINR of the uplink signal given in (3.3) is independent of d_{k,c_m} ; however, it depends on K' , which is the number of D2D users sharing the resource block with a particular uplink cellular user c_m . Therefore, the base station depends on how far the D2D users are from it and not how far the D2D users are from the cellular users; therefore, the joint probability distribution with respect to the random location of c_m 's is not needed when deriving the cdf of the SINR at the eNB.

The coverage probability depends on three D2D-related network parameters: $\mathbb{P}[Q_k = 1] = q$, λ , and $\mathbb{E}[\rho_k^{2/\alpha}]$. As the density $q\lambda$ of D2D transmitters decreases, $\bar{\mathcal{P}}_{\text{cov,C}}(\beta_0)$ increases because a lower D2D link density causes less interference to the cellular link. Moreover, the random D2D PC parameter ρ_k , affects $\bar{\mathcal{P}}_{\text{cov,C}}(\beta_0)$ only through its $(2/\alpha)$ th moment.

Since the cellular user is uniformly distributed in a circle with center eNB and radius $R = R_C$, the cdf of the distance $d = d_{0,c_m}$ of the uplink is given by

$$F_d(r) = \begin{cases} 0 & \text{if } r < 0; \\ \frac{r^2}{R^2} & \text{if } 0 \leq r \leq R; \\ 1 & \text{if } r \geq R. \end{cases} \quad (3.10)$$

Using (3.10), we consider the case when the uplink user employs a constant transmit power $\rho_0 = P_{\text{max,C}}$, and assume a noise variance of $\sigma^2 = 0$ (so SINR_0 is reduced to SIR_0 (signal-to-interference ratio)). For a given path-loss exponent

value, the coverage probability in the interference-limited regime becomes

$$\bar{\mathcal{P}}_{\text{cov,C}}(\beta_0) = \int_0^{R_C} \exp\left(-\theta_0 r^2 \rho_0^{-2/\alpha}\right) \frac{2r}{R_C^2} dr = \frac{1 - \exp\left(-\frac{\mathbb{E}[K'] \beta_0^{2/\alpha}}{\text{sinc}(2/\alpha) \rho_0^{2/\alpha} \mathbb{E}[\rho_k^{2/\alpha}]}\right)}{\frac{\mathbb{E}[K'] \beta_0^{2/\alpha}}{\text{sinc}(2/\alpha) \rho_0^{2/\alpha} \mathbb{E}[\rho_k^{2/\alpha}]}} \quad (3.11)$$

where $\mathbb{E}[K'] = \mathbb{P}[Q_k = 1] \lambda \pi R_C^2$.

Expression (3.11) explicitly shows that the coverage probability of the cellular link depends on: 1) the average number of active D2D transmitters $\mathbb{E}[K']$, 2) certain moments of the power transmitted from the D2D transmitters, 3) the power transmitted by the cellular user ρ_0 , 4) path-loss exponent α , and 5) the target SINR threshold β_0 .

3.3.2 D2D Link Coverage Probability

Using the same approach in the previous subsection, the SINR of the k th D2D link, based on the system model, is given in (3.4). Then:

Proposition 2. *The D2D coverage probability is given by*

$$\bar{\mathcal{P}}_{\text{cov,D}}(\beta_k) = \mathbb{E}_Z \left[e^{-a_2 Z - \theta_k Z^{2/\alpha}} \mathcal{L}_Y(\beta_k Z) \right], \quad (3.12)$$

where β_k is the minimum SINR required for reliable transmission, $a_2 = \beta_k \sigma^2$,

$\theta_k = \frac{\pi \mathbb{P}[Q_k = 1] \lambda \beta_k^{2/\alpha}}{\text{sinc}(2/\alpha)} \mathbb{E}[\rho_k^{2/\alpha}]$, $Z = d_{k,k}^\alpha \rho_k^{-1}$ is a random variable with cdf

$F_Z(z) = \int F_{d_{k,k}}(x^{1/\alpha} p^{1/\alpha}) dF_{\rho_k}(p)$, $Y = |h_{k,c_m}|^2 d_{k,c_m}^{-\alpha} \rho_0$, and $\mathcal{L}_Y(\beta_k Z) = \mathbb{E}_Y[e^{-(\beta_k Z)Y}]$.

Proof. See Appendix A.2.1. □

Using the fact that $|h_{k,c_m}|^2 \sim \exp(1)$, which implies $\mathbb{P}(|h_{k,c_m}|^2 \geq x) = e^{-x}$, and the expectation is over d_{k,c_m} in $\mathcal{L}_Y(\beta_k Z)$, we derive a closed form expression for the D2D coverage probability (3.12) in an interference-limited regime (where

noise variance $\sigma^2 = 0$, and SINR_k reduces to SIR_k) as

$$\begin{aligned}\bar{\mathcal{P}}_{\text{cov,D}}(\beta_k) &= \mathbb{E}_{d_{k,k}^\alpha \rho_k^{-1}} \left[\exp \left(-\theta_k \left(d_{k,k}^\alpha \rho_k^{-1} \right)^{2/\alpha} \right) \times \mathbb{E}_{d_{k,c_m}} \left[e^{-\beta_k \left(d_{k,k}^\alpha \rho_k^{-1} \right) |h_{k,c_m}|^2 d_{k,c_m}^{-\alpha} \rho_0} \right] \right] \\ &= \mathbb{E}_{d_{k,k}^\alpha \rho_k^{-1}} \left[\exp \left(-\theta_k \left(d_{k,k}^\alpha \rho_k^{-1} \right)^{2/\alpha} \right) \times \mathbb{E}_{d_{k,c_m}} \left[\frac{1}{1 + \beta_k \frac{\rho_0}{\rho_k} d_{k,k}^\alpha d_{k,c_m}^{-\alpha}} \right] \right].\end{aligned}\quad (3.13)$$

We next simplify (3.13) by deriving expressions for the various expectations involved.

Corollary 1. *Using Lemma 1 and considering the proposed channel allocation scheme for the case of 2 CUEs, then the first moment of the distance between two uniformly distributed points can be approximated as $\mathbb{E}[d_{k,c_m}] \approx 512R_C/(45\pi^2)$.*

Proof. See Appendix A.3. □

We next employ the following approximation $\mathbb{E}_{d_{k,c_m}} \left[\frac{1}{1 + \kappa d_{k,c_m}^{-\alpha}} \right] \approx \frac{1}{1 + (\kappa)^{2/\alpha} \mathbb{E}[d_{k,c_m}]^{-2}}$ as in [1]. Using this approximation together with the result from corollary 1, equation (3.13) reduces to

$$\bar{\mathcal{P}}_{\text{cov,D}}(\beta_k) \approx \mathbb{E}_{d_{k,k}^\alpha \rho_k^{-1}} \left[\frac{\exp \left(-\theta_k \left(d_{k,k}^\alpha \rho_k^{-1} \right)^{2/\alpha} \right)}{1 + \left(\beta_k \frac{\rho_0}{\rho_k} d_{k,k}^\alpha \right)^{2/\alpha} (512R_C/(45\pi^2))^{-2}} \right]. \quad (3.14)$$

3.3.3 Discussion

The coverage probability depends on the following D2D-related network parameters: density of the D2D links (λ), thinning probability q , target SINR (β), the moments of the power transmitted from the D2D transmitters, and the power transmitted by the cellular user. This modeling approach allows us to analyze the coverage probability and ergodic rate for a D2D underlaid cellular network with high

accuracy. It also enables network designers/operators to optimize network performance by efficiently determining the optimal network parameters mentioned above. The system can control the impact of D2D links on the cellular link through 1) the proposed channel allocation scheme, which constrains the density of the D2D links that uses the same resources with a particular cellular user, and 2) through the proposed power control schemes, which control the transmit power of the D2D users.

Chapter 4

Proposed D2D Distributed Power Control Schemes

In this chapter, we propose distributed power control schemes that only require the CSI of the direct link in order to minimize the interference caused by the D2D users. For link establishment, two static distributed PC are proposed, and both rely on the distance-dependent path-loss parameters [45,46]. On the other hand, for link maintenance, a more adaptive distributed PC is proposed that compensates the measured SINR at the receiver with a variable target SINR. Simulation results are presented to demonstrate the effectiveness of the proposed schemes related to D2D communication.

4.1 Proposed Distance-based Path-loss Power Control (DPPC)

In this PC scheme, each D2D transmitter selects its transmit power based on the channel conditions, namely the distance-based path-loss $d_{k,k}^{-\alpha}$, so as to maximize its own D2D link rate. In order to realize our proposed scheme, we

define D2D proximity as the area of a disk centered at the transmitting UE, with radius $R_D = \left(\frac{P_{\max,D}}{\varrho_{\text{rx}}}\right)^{1/\alpha}$, where $P_{\max,D}$ is the maximum transmit power of the D2D UE, and ϱ_{rx} is the minimum power for the D2D RX to recover a signal (sometimes referred to as receiver sensitivity).

The k th D2D TX can only use transmit power ρ_k with transmit probability \mathcal{P}_{tx} , if the channel quality of the k th D2D link is favorable, in the sense that it exceeds a known non-negative threshold Γ_{\min} :

$$\mathcal{P}_{\text{tx}} \triangleq \mathbb{P}[|h_{k,k}|^2 d_{k,k}^{-\alpha} \geq \Gamma_{\min}] \approx \exp(-\Gamma_{\min} \mathbb{E}[d_{k,k}^\alpha]). \quad (4.1)$$

Furthermore, an estimation error margin ε is introduced to compensate for the error in estimating the distance between the D2D pairs. Hence, the proposed power allocation, based on the *channel inversion* for the D2D link, is given by

$$\rho_k = \begin{cases} \varrho_{\text{rx}} d_{k,k}^\alpha (1 + \varepsilon) & \text{with } \mathcal{P}_{\text{tx}}, \\ 0 & \text{with } 1 - \mathcal{P}_{\text{tx}}, \end{cases} \quad (4.2)$$

where $d_{k,k}$ is the distance between the k th D2D pair, α is the path-loss exponent, and ε is the estimation error margin of $d_{k,k}^\alpha$, such that $0 \leq \varepsilon \leq 1$.

Each D2D transmitter decides its transmit power based on its own channel gain and a known non-negative threshold Γ_{\min} . For a given distribution of the channel gain, selecting a proper threshold Γ_{\min} plays an important role in determining the sum rate performance of the D2D links. For instance, if a large Γ_{\min} is chosen (implying a small \mathcal{P}_{tx}), the inter-D2D interference is reduced. However, a larger Γ_{\min} (implying a smaller \mathcal{P}_{tx}) means a smaller number of active D2D links within the cell. Thus, Γ_{\min} needs to be carefully chosen to balance these two conflicting factors, while providing a high D2D sum rate. We optimize

the choice Γ_{\min} so as to maximize the D2D sum rate as discussed in Section 4.1.3.

Moreover, the D2D transmitter checks if the link quality degrades (i.e., $|h_{k,k}|^2 d_{k,k}^{-\alpha} < \Gamma_{\min}$), then the D2D communication is dropped. Also, the D2D receiver checks if the estimated distance-based path-loss increases, and reports it to the D2D transmitter, conditioned on the fact that the D2D communication link remains active if this distance remains within R_D .

Note here that channel inversion only compensates for the large-scale path-loss effects and not for small-scale fading effects. For instance, instantaneous CSI is not required at the transmitter, since the loss due to distance is compensated. Moreover, the proposed scheme captures the randomness of the distance between the D2D pairs, and if the D2D pairs are close to each other, they will allocate less power than the case if they are further apart. However in [1], a fixed distance between the pairs is assumed and maximum power $P_{\max,D}$ is always allocated for D2D transmission, which needlessly increases power consumption and generates more interference.

Considering the proposed DPPC scheme along with the random locations of D2D users, the transmit powers and the SINRs experienced by the receivers become random as well. Therefore in what follows, we first characterize the transmit power ρ_k via its $\alpha/2$ th moment, and then characterize the cellular and D2D coverage probabilities accordingly. Finally, we derive an expression for the D2D sum rate and maximize in order to optimize the DPPC threshold Γ_{\min} .

4.1.1 Analysis of Power Moments

According to the system model, the D2D receivers are considered to be uniformly distributed in a circle centered at the corresponding D2D transmitter with radius

R_D ; therefore, the cdf of the distance $d_{k,k}$ of the D2D link is similar to that of d_{0,c_m} in (3.10), where $d = d_{k,k}$ and $R = R_D$. Using (3.10), the moments of the transmit power ρ_k for the DPPC scheme, where $\rho_k = \varrho_{\text{rx}} d_{k,k}^\alpha (1 + \varepsilon)$, can be expressed as

$$\mathbb{E}_{d_{k,k}} \left[\rho_k^{2/\alpha} \right] = \varrho_{\text{rx}}^{2/\alpha} \int_0^{R_D} r^2 \frac{2r}{R_D^2} (1 + \varepsilon)^{2/\alpha} dr = \varrho_{\text{rx}}^{2/\alpha} \frac{R_D^2}{2} (1 + \varepsilon)^{2/\alpha}. \quad (4.3)$$

Cellular Coverage Probability for DPPC: By substituting (4.3) for $\mathbb{E}_{d_{k,k}} \left[\rho_k^{2/\alpha} \right]$ into the derived expression (3.11), the cellular coverage probability for DPPC can be obtained.

D2D Coverage Probability for DPPC: For $\rho_k = \varrho_{\text{rx}} d_{k,k}^\alpha (1 + \varepsilon)$, and using the moments of ρ_k in (4.3), the D2D coverage probability in (3.13) becomes

$$\bar{\mathcal{P}}_{\text{cov,D}}(\beta_k) = e^{-\theta_k (\varrho_{\text{rx}} (1 + \varepsilon))^{-2/\alpha}} \times \mathbb{E}_{d_{k,c_m}} \left[\frac{1}{1 + \beta_k \frac{\rho_0}{\varrho_{\text{rx}} (1 + \varepsilon)} d_{k,c_m}^{-\alpha}} \right], \quad (4.4)$$

Following the same approach as in (3.14), the approximated expression for $\bar{\mathcal{P}}_{\text{cov,D}}(\beta_k)$ is given by

$$\bar{\mathcal{P}}_{\text{cov,D}}(\beta_k) \approx \frac{e^{-\theta_k (\varrho_{\text{rx}} (1 + \varepsilon))^{-2/\alpha}}}{1 + \left(\beta_k \frac{\rho_0}{\varrho_{\text{rx}} (1 + \varepsilon)} \right)^{2/\alpha} (512 R_C / (45 \pi^2))^{-2}}. \quad (4.5)$$

4.1.2 Sum Rate of D2D Links

We analyze the sum rate of D2D links when the proposed DPPC scheme is employed, and compute the optimal threshold Γ_{min} of the proposed PC that maximizes the sum rate of D2D links.

Let $|A_D|$ denote the number of active links selected by the proposed PC and

CA algorithms, i.e., $|A_D| = \mathbb{P}[Q_k = 1] \times \mathbb{P}[|h_{k,k}|^2 d_{k,k}^{-\alpha} \geq \Gamma_{\min}] \lambda \pi R_C^2 = \tilde{\lambda} \pi R_C^2$, where $\tilde{\lambda} = \mathbb{P}[Q_k = 1] \times \mathbb{P}[|h_{k,k}|^2 d_{k,k}^{-\alpha} \geq \Gamma_{\min}] \lambda = q \mathcal{P}_{\text{tx}} \lambda$. As in [1], we assume Gaussian signal transmissions on all links, and hence, the distribution of the interference terms becomes Gaussian.

From the SIR distribution of the D2D link given in (4.5) with $\sigma^2 = 0$, the ergodic rate of the typical D2D link is generally expressed as

$$\begin{aligned} \bar{R}_{D2D} &= \int_0^\infty \log_2(1+x) \frac{\partial}{\partial x} [\mathbb{P}[\text{SIR}_k \geq x]] dx \approx \int_0^\infty \frac{1}{1+x} \bar{\mathcal{P}}_{\text{cov,D}}(x) dx \\ &\approx \int_0^\infty \frac{\exp\left(-\frac{\pi \tilde{\lambda} x^{2/\alpha}}{\text{sinc}(2/\alpha)} \mathbb{E}[\rho_k^{2/\alpha}] \left(d_{k,k}^\alpha \rho_k^{-1}\right)^{2/\alpha}\right)}{(1+x) \times \left(1 + \left(x \frac{\rho_0}{d_{k,k}^\alpha \rho_k}\right)^{2/\alpha} \mathbb{E}[d_{k,c_m}]^{-2}\right)} dx. \end{aligned} \quad (4.6)$$

Note that the above general expression of the ergodic rate is valid for any distributed power control scheme that allocates its own transmit power independently of the transmit power used at other D2D transmitters.

Using (3.7) and (4.6), the new achievable sum rate of D2D links is given as

$$\mathcal{R}_s^{(D)} = \mathbb{E} \left[\sum_{k=1}^{K'} \log_2(1 + \text{SIR}_k) \right] = |A_D| \times \bar{R}_{D2D} = \tilde{\lambda} \pi R_C^2 \times \bar{R}_{D2D}. \quad (4.7)$$

4.1.3 D2D Power Control Threshold for DPPC

From the ergodic sum rate of D2D links, we optimize the D2D PC threshold Γ_{\min} by maximizing the derived transmission capacity of D2D links, which is given as

$$\begin{aligned} \mathcal{R}_s^{(D)}(\beta_k) &\approx \frac{q \lambda \mathcal{P}_{\text{tx}} \pi R_C^2 \log_2(1+\beta)}{1 + \left(\beta_k \frac{\rho_0}{(\varrho_{\text{rx}}(1+\varepsilon))}\right)^{2/\alpha} \left(\frac{512 R_C}{45 \pi^2}\right)^{-2}} \times \exp\left(-\frac{\pi \tilde{\lambda} \beta_k^{2/\alpha}}{\text{sinc}(2/\alpha)} \mathbb{E}[\rho_k^{2/\alpha}] (\varrho_{\text{rx}}(1+\varepsilon))^{-2/\alpha}\right) \\ &\approx \frac{\tilde{\lambda} \pi R_C^2 \log_2(1+\beta_k)}{1 + \kappa \beta_k^{2/\alpha}} \exp\left(-\frac{\pi \tilde{\lambda} \beta_k^{2/\alpha}}{\text{sinc}(2/\alpha)} \frac{R_D^2}{2}\right), \end{aligned} \quad (4.8)$$

where $\kappa = \left(\frac{\rho_0}{(\varrho_{\text{rx}}(1+\varepsilon))}\right)^{2/\alpha} \left(\frac{512R}{45\pi^2}\right)^{-2}$ and $\tilde{\lambda} = q\lambda\mathcal{P}_{\text{tx}}$. By solving the following optimization problem, we can compute the new optimal transmission probability:

$$\begin{aligned} & \text{maximize} && \mathcal{R}_s^{(D)}(\beta) \\ & \text{subject to} && 0 \geq \mathcal{P}_{\text{tx}} \geq 1 \end{aligned}$$

The optimal solution of \mathcal{P}_{tx} can be obtained by the 1st order optimality solution, since the objective function has one optimum point. The first order derivative yields:

$$\frac{d\mathcal{R}_s^{(D)}(\beta_k)}{d\mathcal{P}_{\text{tx}}} = 1 - \frac{\pi q \lambda \beta_k^{2/\alpha} \frac{R_D^2}{2}}{\text{sinc}(2/\alpha)} \mathcal{P}_{\text{tx}} = 0. \quad (4.9)$$

The second derivative of $\mathcal{R}_s^{(D)}(\beta_k)$ is applied to test the concavity at \mathcal{P}_{tx} , which is given as

$$\frac{d^2\mathcal{R}_s^{(D)}(\beta_k)}{d\mathcal{P}_{\text{tx}}^2} = -\frac{\pi q \lambda \beta_k^{2/\alpha} \frac{R_D^2}{2}}{\text{sinc}(2/\alpha)} < 0 \quad \text{for } \alpha \geq 2. \quad (4.10)$$

Thus, $\mathcal{R}_s^{(D)}(\beta_k)$ is maximum at $\mathcal{P}_{\text{tx}} = \frac{2\text{sinc}(2/\alpha)}{\pi q \lambda \beta_k^{2/\alpha} R_D^2}$. However, to satisfy the conditions of $\mathcal{P}_{\text{tx}} \in \{0, 1\}$, we have $\mathcal{P}_{\text{tx}}^* = \min\left\{\frac{2\text{sinc}(2/\alpha)}{\pi q \lambda \beta_k^{2/\alpha} R_D^2}, 1\right\}$. Using (4.2) where $\mathcal{P}_{\text{tx}} = \exp(-\Gamma_{\min} \mathbb{E}[d_{k,k}^\alpha])$, then the optimal threshold Γ_{\min}^* can be obtained as

$$\Gamma_{\min}^* = -\ln(\mathcal{P}_{\text{tx}}^*) \frac{2 + \alpha}{2} R_D^{-\alpha} \quad (4.11)$$

Knowing the solution $\mathcal{P}_{\text{tx}}^*$, the approximated transmission capacity in (4.8) can be rewritten as

$$\mathcal{R}_s^{(D)}(\beta) \approx \begin{cases} \frac{\lambda \pi R_C^2 \log_2(1 + \beta_k)}{1 + \kappa \beta_k^{2/\alpha}} \exp\left(-\frac{\pi q \lambda \beta_k^{2/\alpha} R_D^2}{2\text{sinc}(2/\alpha)}\right) & \text{for } \beta_k \leq \tilde{\beta}_k, \\ \frac{2\text{sinc}(2/\alpha) R_C^2 \log_2(1 + \beta_k)}{\beta_k^{2/\alpha} R_D^2 (1 + \kappa \beta_k^{2/\alpha}) \exp(1)} & \text{for } \beta_k > \tilde{\beta}_k, \end{cases} \quad (4.12)$$

where $\tilde{\beta}_k = \left[\frac{2\text{sinc}(2/\alpha)}{\pi q \lambda R_D^2}\right]^{\alpha/2}$.

The transmission capacity of the D2D links depends on the relationship

between the minimum SINR value β_k and the network parameters: path-loss exponent α , the density of the D2D links $q\lambda$, and the maximum allowable distance between the D2D pairs R_D . When $\beta_k < \tilde{\beta}_k$, all D2D transmitters are scheduled; therefore no admission control is applied. However, when $\beta_k \geq \tilde{\beta}_k$, the D2D links are scheduled with transmit probability $\mathcal{P}_{\text{tx}}^*$, which mitigates the inter-D2D interference since the transmission capacity no longer depends on the density of the nodes λ .

By integrating the transmission capacity in (4.12) with respect to β , the sum rate of D2D links is expressed as follows

$$\begin{aligned} \mathcal{R}_s^{(D)} \approx & \int_0^{\tilde{\beta}_k} \frac{q\lambda\pi R_C^2}{(1+x)(1+\kappa x^{2/\alpha})} \exp\left(-\frac{\pi q\lambda x^{2/\alpha} R_D^2}{2\text{sinc}(2/\alpha)}\right) dx \\ & + \int_{\tilde{\beta}_k}^{\infty} \frac{2\text{sinc}(2/\alpha)R_C^2}{(x^{2/\alpha}R_D^2)(1+x)(1+\kappa x^{2/\alpha})} \exp(-1) dx. \end{aligned} \quad (4.13)$$

The DPPC scheme is summarized in the first part of the pseudo-code in Algorithm 1.

Algorithm 1 Static Distributed Power Control

- 1: **if** D2D TX k is unable to acquire $d_{0,k}$ **then**
 - 2: \triangleright Apply *DPCC* scheme
 - 3: Calculate Γ_{\min} that maximizes the D2D sum rate $\mathcal{R}_s^{(D)}(\beta)$ according to (4.11)
 - 4: **if** $|h_{k,k}|^2 d_{k,k}^{-\alpha} \geq \Gamma_{\min}$ **and** $d_{k,k} \leq R_D$ **then**
 - 5: D2D candidates transmit in D2D mode
 - 6: $\rho_k \leftarrow \varrho_{\text{rx}} d_{k,k}^{\alpha} (1 + \varepsilon)$.
 - 7: **else** $\rho_k \leftarrow 0$
 - 8: **else**
 - 9: \triangleright Apply *EDPPC* scheme
 - 10: Set $\Gamma_{\min} = G_{\min}$
 - 11: **if** $|h_{k,k}|^2 d_{k,k}^{-\alpha} \geq \Gamma_{\min}$ **and** $d_{k,k} \leq R_D$ **then**
 - 12: D2D candidates transmit in D2D mode
 - 13: $U \leftarrow \varrho_{\text{rx}} (1 + \varepsilon)$, $V \leftarrow \mu \varrho_{\text{rx}} (1 + \varepsilon)$
 - 14: $\rho_k \leftarrow \min\{U d_{k,k}^{\alpha}, V d_{0,k}^{\alpha}\}$.
 - 15: **else** $\rho_k \leftarrow 0$
-

4.2 Proposed Extended Distance-based Path-loss Power Control (EDPPC)

EDPPC is proposed as an extended DPPC scheme for link establishment stage. We consider in this scheme an extra distance-based path-loss parameter $d_{0,k}^{-\alpha}$, where $d_{0,k}$ is the distance between the eNB and the D2D k th TX, in order to reduce the D2D interference at the eNB. This scheme works only if the D2D users are able to obtain estimates of $d_{0,k}$ from the eNB.

We apply the same conditions as in DPPC in (4.1), where the k th D2D TX can only use the transmit power ρ_k with transmit probability \mathcal{P}_{tx} for favorable channel conditions. However, in this PC scheme, $\Gamma_{\min} = G_{\min}$ is a static value that is chosen by the eNB and broadcasted to the D2D transmitters.

The EDPPC scheme works as follows: each D2D TX selects its transmit power based on the distance-based path-loss parameters $d_{k,k}^{-\alpha}$ and $d_{0,k}^{-\alpha}$. The role of the additional parameter $d_{0,k}^{-\alpha}$ is to suppress interference even more at the eNB. Let $U = \varrho_{\text{rx}}(1 + \varepsilon)$ and $V = \mu\varrho_{\text{rx}}(1 + \varepsilon)$, where μ is a PC parameter with small value chosen so that the D2D transmitter does not cause excessive interference to the eNB and to other D2D UEs in the same cell, and ε is an estimation error margin that offsets any inaccuracy in estimating the path-loss parameters $d_{k,k}^{\alpha}$ and $d_{0,k}^{\alpha}$. Then, the proposed power allocation for the D2D link is based on the following:

$$\rho_k = \begin{cases} \min\{Ud_{k,k}^{\alpha}, Vd_{0,k}^{\alpha}\} & \text{with } \mathcal{P}_{\text{tx}} \\ 0 & \text{with } 1 - \mathcal{P}_{\text{tx}}, \end{cases} \quad (4.14)$$

Due to the nature of the EDPPC scheme, along with the random locations of D2D users, the transmit powers and the SINRs experienced by the receivers become also random. Therefore, we derive $\alpha/2$ th moments of the transmit power

ρ_k so that the cellular and D2D coverage probabilities can be characterized accordingly.

4.2.1 Analysis of Power Moments

The D2D TX and the corresponding D2D RX are assumed to be uniformly distributed; therefore, the distance $d_{0,k}$ of the D2D interfering link with the eNB and the distance $d_{k,k}$ of the direct D2D link are uniformly distributed in circles with radii R_C and R_D , respectively.

Theorem 1. *The expected value of the minimum of two random variables $A, B \in \Omega \rightarrow \mathbb{R}$ is $\mathbb{E}[\min(A, B)] = \mathbb{E}[A] + \mathbb{E}[B] - \mathbb{E}[\max(A, B)]$.*

Proof. See Appendix A.4. □

Lemma 2. *The expected value of the maximum of two random variables $A, B \in \Omega \rightarrow \mathbb{R}$ with pdfs $f_A(a), f_B(b)$ and cdfs $F_A(a), F_B(b)$, respectively, is*

$$\mathbb{E}[\max(A, B)] = \int_{-\infty}^{\infty} a f_A(a) F_B(a) da + \int_{-\infty}^{\infty} b f_B(b) F_A(b) db. \quad (4.15)$$

Proof. See Appendix A.5. □

Corollary 2. *Using the distribution functions of $d_{k,k}$ and $d_{0,k}$, the moments of the transmit power ρ_k are given by*

$$\mathbb{E}_{d_{k,k}} \left[\rho_k^{2/\alpha} \right] = \begin{cases} \frac{R_C^2 V^{2/\alpha}}{2} - \frac{R_C^4 V^{4/\alpha}}{6R_D^2 U^{2/\alpha}} & \text{if } R_D^2 U^{2/\alpha} > R_C^2 V^{2/\alpha} \\ \frac{R_D^2 U^{2/\alpha}}{2} - \frac{R_D^4 U^{4/\alpha}}{6R_C^2 V^{2/\alpha}} & \text{if } R_D^2 U^{2/\alpha} \leq R_C^2 V^{2/\alpha}. \end{cases} \quad (4.16)$$

Proof. See Appendix A.6. □

Under this power control scheme, it is noted that: 1) D2D UEs closer to the serving eNB (where $d_{0,k} < d_{k,k}$) normally cause a stronger uplink interference and

thus their transmit powers are reduced, 2) D2D UEs closer to the cell edge can transmit at a higher power since their interference to the uplink cellular UE is dropped due to path-loss, and 3) D2D pairs with close proximity will be allocated less power than D2D pairs that are far apart.

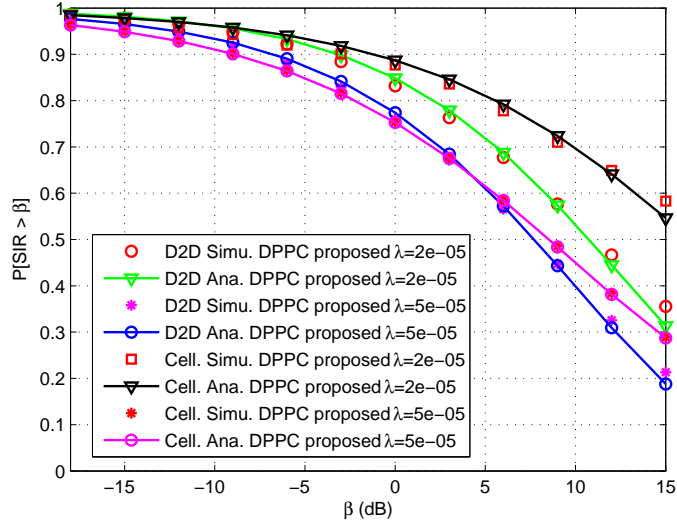
The EDPPC scheme is summarized in the second part of Algorithm 1.

Cellular Coverage Probability for EDPPC: By substituting $\mathbb{E}_{d_{k,k}} \left[\rho_k^{2/\alpha} \right]$ obtained in (4.16) into the derived expressions (3.11), the cellular coverage probability for EDPPC can be obtained.

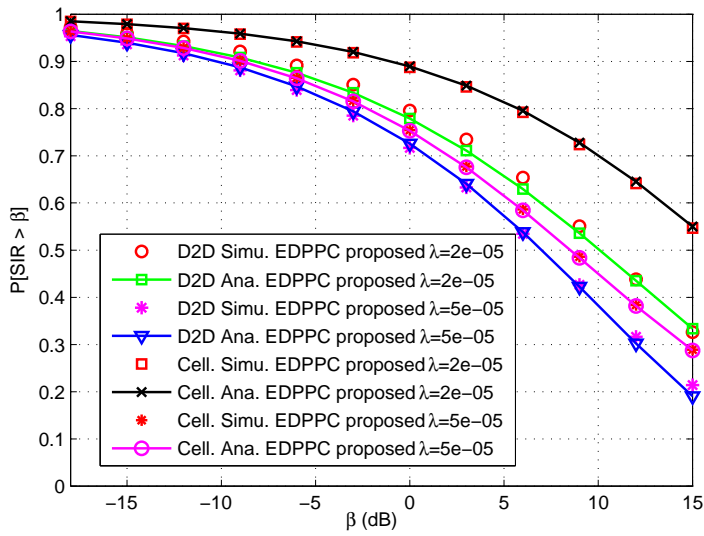
D2D Coverage Probability for EDPPC: Using the same methodology as in Theorem 1, for $\rho_k = \min\{Ud_{k,k}^\alpha, Vd_{0,k}^\alpha\}$, and using the moments of ρ_k in (4.16) and the pdf of $d_{k,k}$ and $d_{0,k}$, the D2D coverage probability in (3.14) becomes

$$\begin{aligned} \bar{\mathcal{P}}_{\text{cov,D}}(\beta_k) \approx & \frac{e^{-\theta_k(\varrho_{\text{rx}}(1+\varepsilon))^{-2/\alpha}}}{1 + \left(\beta_k \frac{\rho_0}{\varrho_{\text{rx}}(1+\varepsilon)} \right)^{2/\alpha} (512R_C/(45\pi^2))^{-2}} \int_0^{\mu^{1/\alpha}R_C} \left(\int_0^x \frac{2y}{R_D^2} dy \right) \frac{2\mu^{-2/\alpha}x}{R_C^2} dx + \\ & \int_0^{R_D} \left(\int_0^y \frac{\exp\left(-\theta_k\left(x^{-\alpha}y^\alpha(\varrho_{\text{rx}}(1+\varepsilon))^{-1}\right)^{2/\alpha}\right)}{1 + \left(\beta_k \frac{\rho_0}{x^\alpha y^{-\alpha}(\varrho_{\text{rx}}(1+\varepsilon))} \right)^{2/\alpha} (512R_C/(45\pi^2))^{-2}} \frac{2\mu^{-2/\alpha}x}{R_C^2} dx \right) \frac{2y}{R_D^2} dy. \end{aligned} \quad (4.17)$$

To validate our analysis for DPPC and EDPPC, we compare the derived analytical expressions with their corresponding simulated results for $\lambda \in \{2 \times 10^{-5}, 5 \times 10^{-5}\}$, $\tilde{\lambda} = 0.5\lambda$, $M = 2$, $\mu = 0.0005$, $\varepsilon = 0.5$, and $\alpha = 4$. In Fig. 4.1(a) and Fig. 4.1(b), we validate the correctness of the analytical expressions for the cellular coverage probability of (3.11) and D2D coverage probability of (4.5) and (4.17), while using the derived expressions of $\mathbb{E}[\rho_k^{2/\alpha}]$ for DPPC and EDPPC in (4.3) and (4.16), respectively. As shown in the plots, the curves of the proposed DPPC and EDPPC schemes match well with simulated results over the entire range of β .



(a)



(b)

Figure 4.1: Analytical vs. simulated coverage probability for cellular and D2D users using (a) DPPC, and (b) EDPPC scheme.

4.3 Proposed Soft Dropping Distance-based Power Control (SDDPC)

The PC schemes proposed earlier provide a static power allocation where varying channel quality during D2D transmissions is not taken into consideration. An adaptive PC with variable target SINR would be an attractive approach to guard cellular and D2D communications against mutual interference and maintain good link quality. We propose a soft dropping distance-based PC (SDDPC) scheme that gradually decreases the target SINR as the required transmit power increases. This increases the probability of finding a feasible solution for the PC problem in which the target SINR values for all co-channel links can be achieved. Hence, links with bad quality, where the receiver is far from the transmitter and requires higher power, would target *lower* SINR values. On the other hand, links with better quality, where the receiver is near the transmitter and requires lower power, would target *higher* SINR values.

In the SDDPC scheme, each UE iteratively varies its transmit power so that a power vector $\boldsymbol{\rho}$ for all UEs in the system is found such that the SINR_k of the k th UE satisfies

$$\text{SINR}_k(K', \boldsymbol{\rho}) \geq \beta_k(d_{k,k}),$$

where $\beta_k(d_{k,k})$ is the target SINR of the k th UE that varies according to the distance between the D2D pairs $d_{k,k}$. The SDDPC scheme uses a target SINR that varies between a maximum value β_{\max} and a minimum β_{\min} as the distance between the D2D pairs varies between $R_{\min,D}$ and a maximum value R_D , while satisfying a power constraint of $P_{\min,D} \leq \rho_k \leq P_{\max,D}$.

The target SINR $\beta_k(d_{k,k})$ of the k th D2D UE at TTI (t) is given according to

$$\beta_k(d_{k,k}) = \begin{cases} \beta_{\max} & \text{if } d_{k,k}^{(t)} \leq R_{\min,D} \\ \beta_{\max} \left(\frac{d_{k,k}^{(t)}}{R_{\min,D}} \right)^v & \text{if } R_{\min,D} < d_{k,k}^{(t)} < R_D \\ \beta_{\min} & \text{if } d_{k,k}^{(t)} \geq R_D, \end{cases} \quad (4.18)$$

where $v = \frac{\log_{10}(\beta_{\min}/\beta_{\max})}{\log_{10}(R_D/R_{\min,D})}$.

Furthermore, the power of each D2D transmitter is updated with every transmission as

$$\rho_k^{(t+1)} = \rho_k^{(t)} \left(\frac{\beta_k(d_{k,k}^{(t)})}{\text{SINR}_k(K, \boldsymbol{\rho}^{(t)})} \right)^\eta, \quad (4.19)$$

where η is a control parameter given by $(1 - v)^{-1}$ [53]. Finally, the achieved power $\rho_k^{(t+1)}$ is constrained as follows

$$\rho_k^{(t+1)} = \min\{P_{\max,D}, \max\{\rho_k^{(t+1)}, P_{\min,D}\}\}.$$

The SDDPC scheme is a distributed approach and the target SINR ($\beta_k(d_{k,k})$) depends on the distance between the D2D pair; therefore, decision making is done by the D2D users themselves. In particular, the D2D receivers can use the sidelink control channel (e.g., Physical Sidelink Control Channel (PSCCH)) as per the LTE technical specification in 3GPP TS 36.331 [119] to report back to the corresponding D2D transmitter the received SINR value and the distance based path-loss $d_{k,k}$ whenever the received SINR is below the target value.

The SDDPC scheme is summarized in Algorithm 2.

Algorithm 2 Dynamic Distributed Power Control

procedure SDDPC

$$\rho_k^{(t)} \leftarrow P_{\min,D} = \varrho_{\text{rx}} R_{\min,D}^\alpha (1 + \varepsilon)$$

Calculate $\beta_k(d_{k,k})$ according to (4.18)

if $\text{SINR}_k(K, \boldsymbol{\rho}) < \beta_k(d_{k,k})$ **then**

LOOP: While $\text{SINR}_k(K, \boldsymbol{\rho}) < \beta_k(d_{k,k})$ **and** $\rho_k^{(t)} \neq P_{\max,D}$ **do**

$$\rho_k^{(t+1)} \leftarrow \rho_k^{(t)} \left(\frac{\beta_k(d_{k,k}^{(t)})}{\text{SINR}_k(K, \boldsymbol{\rho}^{(t)})} \right)^\eta$$

$$\rho_k^{(t+1)} \leftarrow \min\{P_{\max,D}, \max\{\rho_k^{(t+1)}, P_{\min,D}\}\}$$

goto LOOP

else $\rho_k^{(t+1)} \leftarrow \rho_k^{(t)}$

end

4.4 Discussion

On complexity and convergence of Algorithms 1 and 2, we note that Algorithm 1 is a non-iterative, low complexity algorithm $O(1)$, which requires around 4 simple computations. Convergence is not an issue since it is non-iterative. For Algorithm 2, the power allocated to the D2D users is chosen iteratively and in a non-decreasing manner. At each iteration, ρ_k is increasing which increases SINR_k until SINR_k approaches the target β_k . Since the D2D TX has finite available power, the SINR_k achieved by the proposed algorithm is also finite. For these reasons and following the same methodology as [53,120], the proposed algorithm is guaranteed to converge to a finite SINR_k . The proof is similar to Theorem 3 in [53, 120] and hence is omitted for brevity. Furthermore, figure 4.2 shows the number of iterations needed in this algorithm that are very low. For instance, as M increases, the number of D2D links K' , sharing the resources with one of the cellular users, decreases; therefore the interference level caused by the D2D users will decrease and hence increasing the SINR_k . This will cause Algorithm 2 (SDDPC) to converge faster (for $M = 3$, it requires an average of 3 iterations to converge).

Moreover, Algorithms 1 and 2 may not necessarily converge to the global

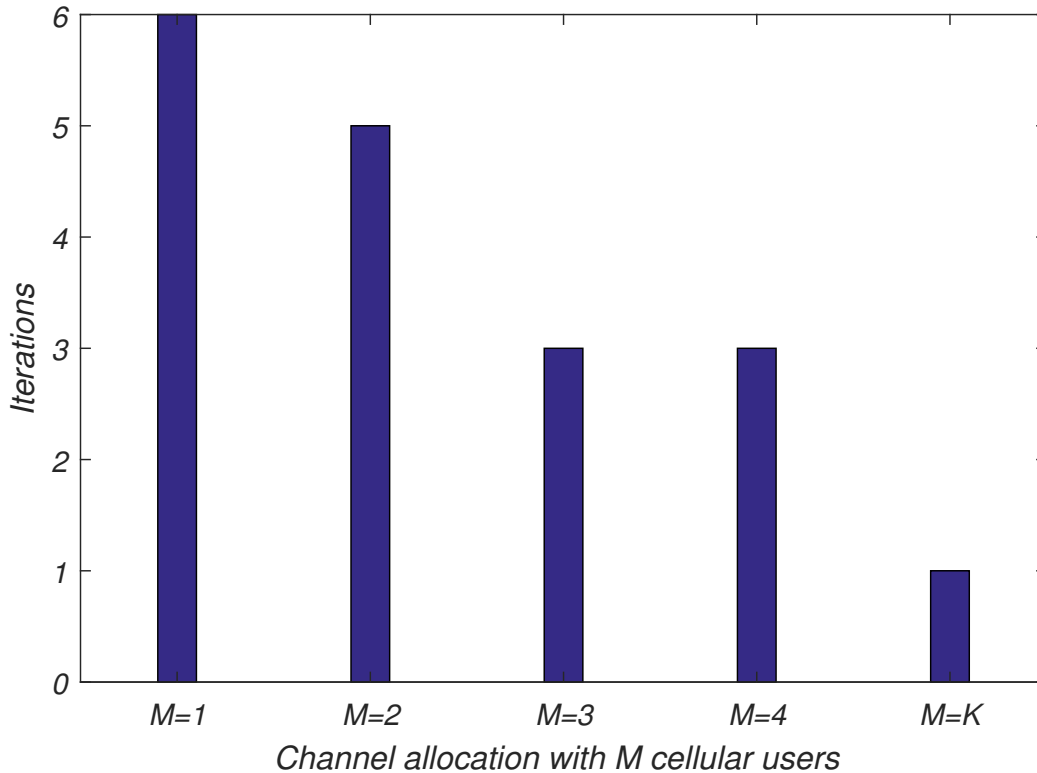


Figure 4.2: Number of iterations for the SDDPC scheme for $\lambda = 5 \times 10^{-5}$ and different M channel allocations.

optimal solutions. The development of global optimal power allocation is otherwise done in a centralized manner at the base station. However, it would require excessive signaling overhead in which the computational complexity grows exponentially with K [1, 2]. This excessive overhead is avoided in the distributed case, with graceful degradation in performance.

Furthermore, we note that using the two proposed static distributed PC schemes for link establishment, the allocated power remains constant over the resource blocks since we apply equal power allocation to all the assigned resource blocks. On the other hand, for link maintenance, SDDPC compensates the measured SINR at the receiver with a variable target SINR. The power allocated per PRB of each D2D UE is updated every transmission as per (4.19).

In order to realize the proposed PC schemes, each D2D transmitter needs to have knowledge of: 1) the distance based path-loss parameters $d_{k,k}^\alpha$ and $d_{0,k}^\alpha$ in order to allocate power, 2) the target SINR β , 3) the density of the D2D links $q\lambda$, and (4) CSI of the direct link. Knowledge of distance based path-loss $d_{k,k}^\alpha$ and β can be acquired through feedback from the corresponding D2D receiver. During D2D link establishment [10], the density of the D2D links (which is the average number of active D2D links per unit area) as well as $d_{0,k}^\alpha$ can be estimated at the eNB. The D2D transmitters acquire the density $q\lambda$ when the eNB broadcasts it using the downlink control channel, and acquire $d_{0,k}^\alpha$ through feedback from the eNB.

All D2D pairs can use the sidelink channels (Physical Sidelink Broadcast Channel (PSBCH) and PSCCH) [119] to transmit reference signals to enable D2D receivers to perform measurements and report them back to the eNB or to the corresponding D2D transmitter. Each D2D receiver can reliably estimate the distance based path-loss parameters using these signals by averaging the effects of fading over multiple resource blocks.

The eNB can also estimate distances through the location updates defined in 3GPP TS 23.303 [121], and the path-loss exponent can be estimated as per [122] through defining path-loss exponents based on the region of the D2D pairs location. The UE's location information exchanged is expressed in shapes as defined in 3GPP TS 23.032 [123] as universal geographical area description (GAD).

4.5 Simulation Results

In this section, we provide numerical results for the D2D underlaid cellular network. First, we show how the estimation error margin (ε) and the PC control parameter (μ) for DPPC and EDPPC affect the coverage probability for the

Table 4.1: Simulation Parameters

Parameter	Value
Cell radius (R_C)	500 m
Max. D2D link range (R_D)	50 m
Min. D2D link range ($R_{\min,D}$)	5 m
D2D link density (λ)	2×10^{-5} and 5×10^{-5}
Average # D2D links (K)	$\mathbb{E}[K] = \pi\lambda R_C^2 \in \{15, 39\}$
Path-loss exponent (α)	4
Target SINR threshold (β)	varies from -18 dB to 18 dB
Max. TX power of cellular user [2]	$P_{\max,C} = 100$ mW
Max. TX power of D2D user [1]	$P_{\max,D} = 0.1$ mW
Min. TX power of D2D user	$P_{\min,D} = 0.2$ μ W
Estimation margin ε	0.5
Channel quality threshold for EDPPC G_{\min}	-40 dbm
PC parameter μ for EDPPC	0.0005
Receiver sensitivity ϱ_{rx}	$\varrho_{\text{rx}} = P_{\max,D} R_D^{-\alpha}$
Noise variance (σ^2)	-112.4 dBm
Monte-Carlo Simulations	1000
TTI	1 ms

cellular and the D2D links. Then, we show the performance gains of using the proposed CA and PC schemes (compared to the on/off PC in [1]) in terms of coverage probability, spectral and energy efficiency.

4.5.1 Simulation Setup

Figure 4.5.1 shows a snap shot depicting the geometry of a typical cell. The eNB is located at the center position $(0, 0)$ and the uplink users are uniformly located within a radius R_C . The D2D transmitters are located according to a PPP distribution with $\lambda \in \{2 \times 10^{-5}, 5 \times 10^{-5}\}$ in a ball centered at the eNB and radius $R_C + 250$ m. The system parameters used throughout the experimental simulations are summarized in Table 4.1. Moreover, the transmit power of the cellular user is set as $\rho_0 = P_{\max,C}$.

4.5.2 Coverage Probability for DPPC and EDPPC with Variable Parameters

In a dense D2D link deployment scenario, the average number of D2D links in the cell is $\mathbb{E}[K] = 39$ and the average number of D2D links sharing resources with one of the two cellular users is $\mathbb{E}[K'] = 20$. For the case of variable ε for both DPPC and EDPPC, we plot the cellular and D2D coverage probability in Figs. 4.4(a) and 4.4(b). As shown in the figures, as the error margin varies from 0.1 to 0.9 ($\mu = 0.0005$), the cellular coverage probability decreases while the D2D coverage probability increases. D2D users allocate more power to enhance the D2D link, thus causing more interference to the cellular users. In addition, it is noted in Fig. 4.4(a) for DPPC that no D2D link is dropped when $\beta < 10$ dB, since the transmit probability $\mathcal{P}_{\text{tx}} = \min\left\{\frac{2\text{sinc}(2/\alpha)}{\pi q \lambda \beta^{2/\alpha} R_D^2}, 1\right\} = 1$. However, when $\beta > 10$ dB, the transmit probability is activated where $\mathcal{P}_{\text{tx}} \neq 1$, and some D2D links are dropped thus reducing the D2D interference and enhancing the link coverage for D2D and cellular transmitters.

In Fig. 4.4(c), we vary the control parameter μ for $\varepsilon = 0.5$ using the EDPPC scheme. As μ decreases from 0.005 down to 0.0001, the cellular coverage probability increases and D2D coverage probability decreases. Hence D2D links are dropped according to μ so that they do not cause excessive interference to cellular users. Furthermore, the remaining D2D users will allocate less power, thus the interference at the cellular users and at the other D2D users will be even more diminished. Therefore, the proposed scheme can effectively protect cellular users from interference caused by the D2D users.

4.5.3 Cellular Coverage Probability for all PC schemes

In Figs. 4.5(a) and 4.5(b), we plot the coverage probability of the cellular links using our proposed schemes for two scenarios where the D2D links share the resources with one and two cellular users in dense and sparse networks. We also compare the results with that of 1) the on/off PC scheme in [1], which are the same results as in [2] for the best case scenario with zero channel uncertainty, and 2) the on/off PC scheme in [2] with channel uncertainty factor of 0.5. It can be seen that all the proposed schemes outperform the scheme in [1, 2]. In particular for the case of 2 CUEs, SDDPC increases the coverage probability by more than 40% (45%) in dense (sparse) networks compared to [1, 2] for the entire range of β_0 . The EDPPC scheme performs better than DPPC due to the extra $d_{0,k}^{-\alpha}$ parameter that further reduces the interference at the eNB. However, SDDPC outperforms the other PC schemes as it protects the cellular links using the adaptive approach.

As expected, the cellular coverage probability increases when D2D users share resources with multiple cellular users. The reason is that a smaller number of D2D links share the same resources with a particular CUE, which results in a reduction in the interference caused by the D2D transmissions.

In addition, one can note that the centralized power control [2] achieves nearly perfect cellular user coverage probability performance in the low target SINR values, at high cost of system complexity as discussed in Section. 4.4.

4.5.4 D2D Coverage Probability for all PC schemes

Figures 4.6(a) and 4.6(b) show the coverage probability of D2D links using the proposed PC schemes in dense and sparse network deployments. As shown, all proposed schemes outperform the schemes in [1, 2]. On one hand, the coverage

probability for SDDPC increases by up to 60% (50%) for the dense (sparse) scenario. On the other hand, DPPC and EDPPC have approximately similar performance where the coverage probability increases by 40% (30%). However, SDDPC outperforms the other PC schemes, since the D2D links set variable target SINRs. For instance, links with good quality have high SINR target, while links with low quality have low SINR target.

Moreover, when D2D users share resources with more than one cellular user, the D2D coverage probability using our proposed PC schemes is significantly enhanced as the interference caused by the D2D transmission on other D2D users is reduced.

In general, the D2D coverage probability performance decreases in the dense scenario; however, the total number of successful D2D transmissions is larger than that of the sparse D2D link deployment scenario. For instance, when the target SINR is 0 dB, the total number of successful D2D transmissions in both sparse and dense scenarios is $|A_D|_{\text{sparse}} = \mathbb{E} [K\bar{\mathcal{P}}_{\text{cov,D}}(\beta_k)] = 15 \times 0.9 \approx 13$ and $|A_D|_{\text{dense}} = 39 \times 0.88 \approx 34$, respectively, using the proposed SDDPC scheme and resources are shared with 2 CUEs. The corresponding numbers of successful D2D transmissions from [1] are $|A_D|_{\text{sparse}} = 15 \times 0.58 \approx 8$ and $|A_D|_{\text{dense}} = 39 \times 0.4 \approx 15$, respectively. Therefore, a significant increase in the number of the D2D links is attained using the proposed SDDPC scheme.

In addition, one can note that the centralized power control [2] (with high signaling overhead and complexity) does not perform as well for the D2D case, since this approach works on maximizing the SINR of the uplink user and allows less D2D links to access the network through the admission control. However, with less complexity, our proposed schemes outperform the centralized approach.

4.5.5 Coverage Probability with Variable Channel Allocation parameter (M)

Figures 4.7(a) and 4.7(b) show the coverage probability of cellular and D2D links using the proposed PC schemes in dense network while varying the channel allocation parameter M . Upon increasing M , the coverage probability for the D2D and cellular users is enhancing, since a smaller number of D2D users (which share the same resources) will generate interference. Moreover, we have considered the maximum allocation case where $M = K$ in which one cellular uplink will share the resources with only one D2D link and $\mathbb{E}[K'] = \frac{\mathbb{E}[K]}{M} = 1$. In this case, the uplink signal will observe interference from only the farthest D2D user, and the D2D link will observe the interference from only the farthest cellular uplink user. Thus, the coverage probability for the D2D and the cellular link is greatly enhanced. Furthermore, we compare our results with the case of no power control applied at the D2D links where $\rho_k = P_{\max,D}$ and, as expected, the coverage probabilities are drastically affected (decreased by more than 20%); since the D2D-interference is overwhelming the receivers (Base station and the D2D receivers). Therefore, our proposed channel allocation and power control schemes are effective interference mitigation methods in order to guarantee the QoS of the cellular uplinks and D2D links.

4.5.6 Spectral and Power Efficiency

Figure 4.8 shows the spectral and power efficiency of the D2D and cellular system when applying the proposed PC schemes in a dense deployment scenario, where resources are shared with one, two, and three cellular users. The spectral and power efficiency are defined as follows: 1) Spectral efficiency (SE) is the sum rate $\mathcal{R}_s^{(D)}$ for all D2D links in bps/Hz/cell as defined in (3.7), and 2) Power

efficiency (PE) is given by the ratio of the D2D spectral efficiency achieved over the average transmit power of the D2D links in bps/Hz/cell/W. The figure shows that SDDPC is spectrally and power efficient since more D2D links are able to achieve higher SINR values and less power is allocated for the D2D links. For the case of static PC schemes, DPPC is more spectrally efficient because it maximizes the D2D sum rate. On the other hand EDPPC is more power efficient than DPPC, since less power is allocated. In addition, as expected, when sharing resources with more cellular users, the spectral efficiency of the system decreases (by 15% as shown); however, the coverage probabilities (for cellular and D2D) increase because the interference level is reduced, as shown in Fig. 4.5 and Fig. 4.7.

In addition, when considering $M=2$ the performance is efficient in the sense that it gives a compromise between coverage, spectral efficiency, and complexity. The eNB performs only one comparison for each active D2D ($d_{k,c_1} > d_{k,c_2}$). However, when M is further increased, the spectral efficiency for the EDDPC becomes lower than that in [1] and the complexity increases.

A trade-off exists between spectral efficiency, power efficiency, and coverage probability. If it is desired for the cellular and D2D link to be of high quality, then CA should be applied with D2D users sharing resources with more than one cellular user. However, if it is required that the D2D communications to be power efficient and not cause too much interference on the uplink, then EDPPC has an advantage over the DPPC. Otherwise, if spectral efficiency is a priority, then DPPC performs best, particularly when D2D users share resources with one cellular user. Finally, SDDPC proves most adequate for link maintenance since it is both spectrally and power efficient, and it maintains the link quality for both D2D and cellular users.

4.6 Conclusion

In this work, a random network model for a D2D underlaid cellular system based on stochastic geometry has been proposed. Using this modeling approach, it is possible to derive closed-form analytical expressions for the coverage probabilities and ergodic sum-rates, which give insight into how the various network parameters interact and affect link performance and quality. Unlike previous work, it is shown that a channel allocation scheme that allows D2D links to share resources with more than just one cellular user has merit. New power control schemes targeted for D2D link establishment and link maintenance have been shown to adequately control interference levels under various static and dynamic conditions, using distance-based path-loss parameters (with error margin), varying target SINR, and local CSI. It has been shown through experimental simulations that network performance in terms of coverage probability and spectral efficiency is improved by activating more underlaid D2D links while maintaining the quality of cellular links, and at the same time enhancing power efficiency.

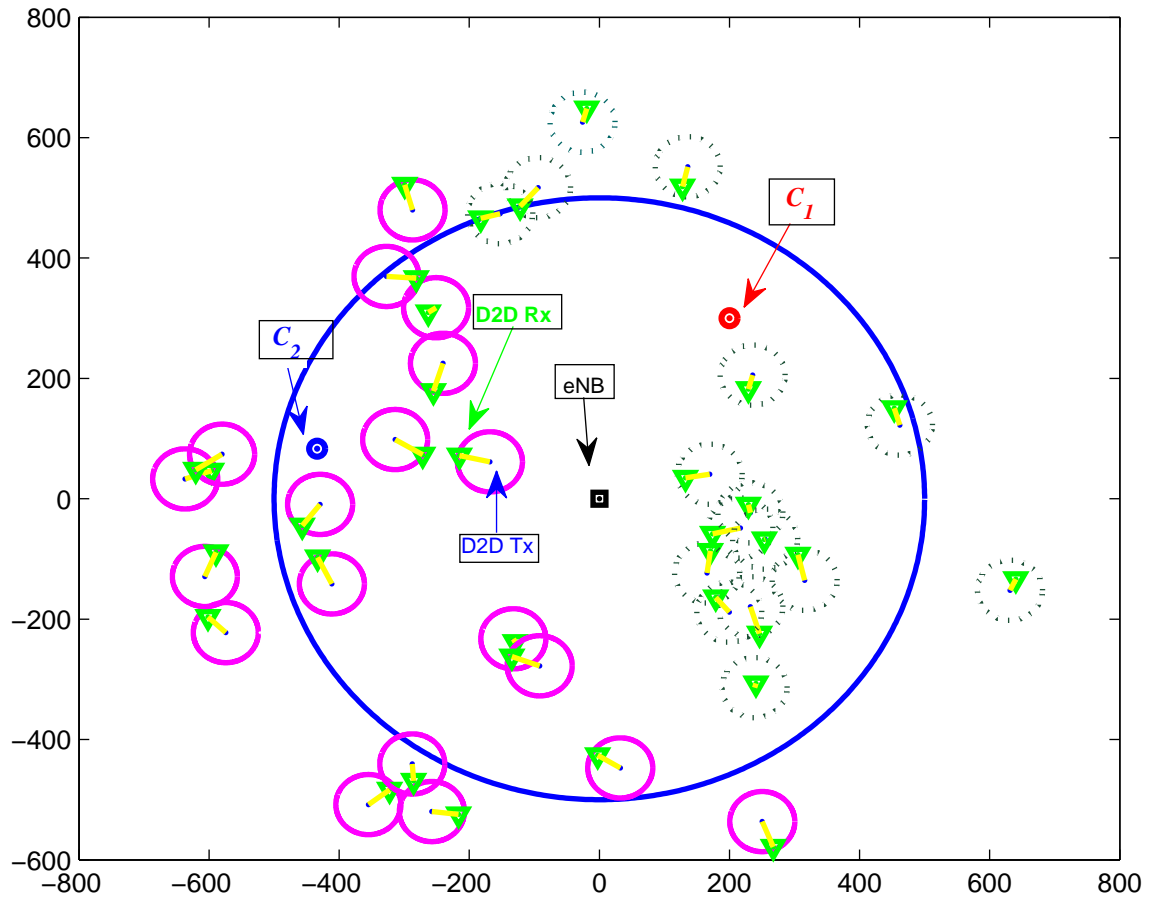
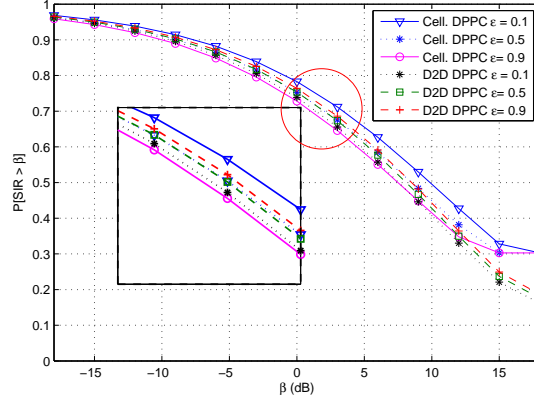
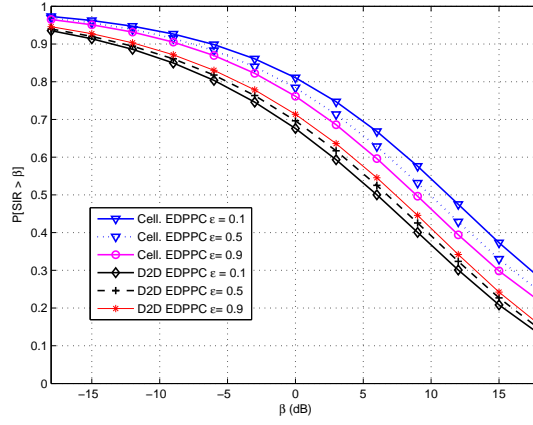


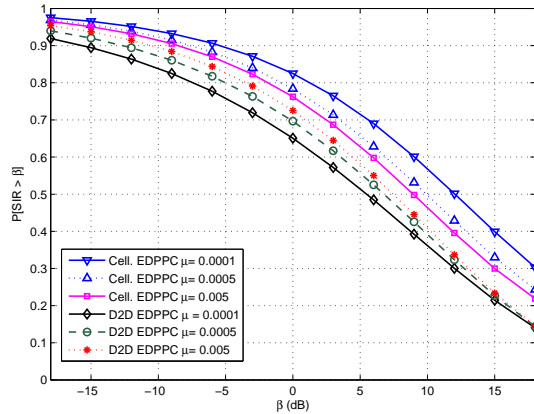
Figure 4.3: A snapshot of link geometry for a D2D underlaid cellular network assuming a sparse D2D link deployment scenario (i.e., $\lambda = 2 \times 10^{-5}$). D2D links in circles share resources with CUE c_1 , while D2D links in dashed circles share resources with CUE c_2 .



(a)

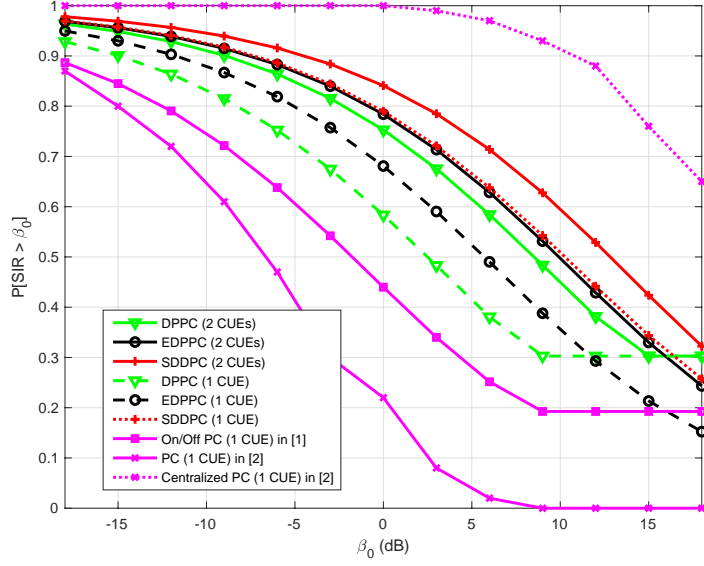


(b)

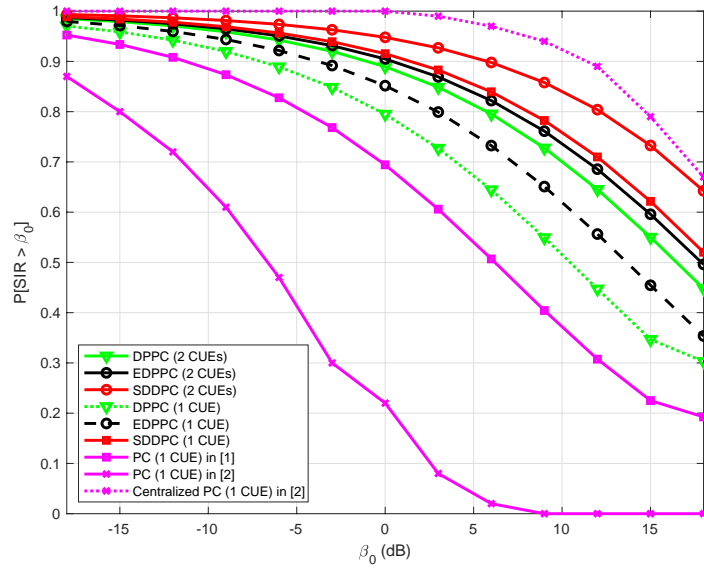


(c)

Figure 4.4: (a) Coverage probability for cellular and D2D users where resources are shared with 2 CUEs, using the proposed DPPC with variable ε . (b) Same as (a) but using the proposed EDPPC scheme. (c) Using the proposed EDPPC with variable μ .

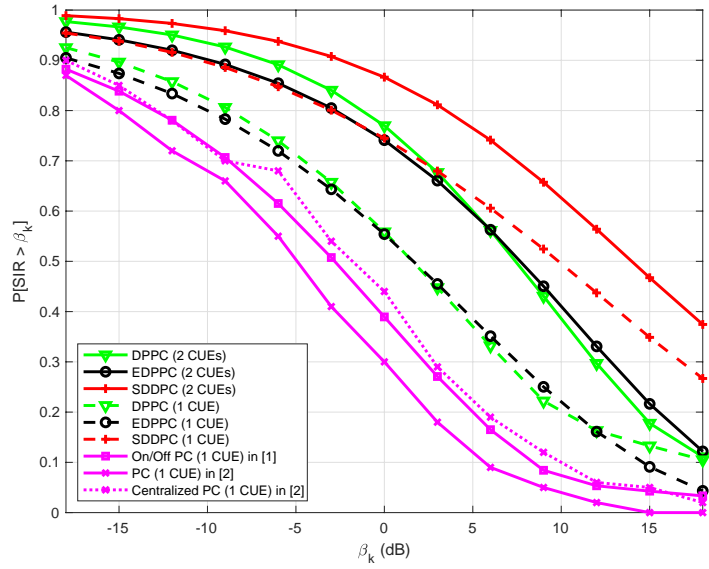


(a)

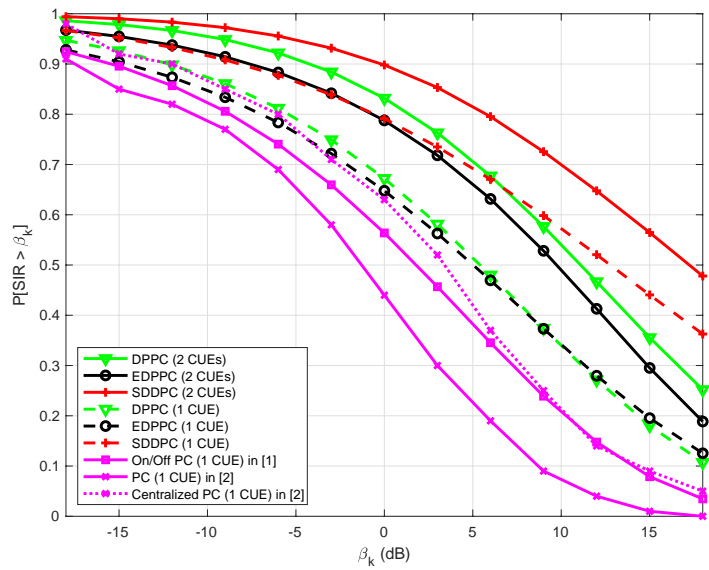


(b)

Figure 4.5: Coverage probability for cellular using all the proposed PC schemes in this work vs. that of [1, 2]: (a) For cellular users in dense network scenario, (b) for cellular users in sparse network scenario.

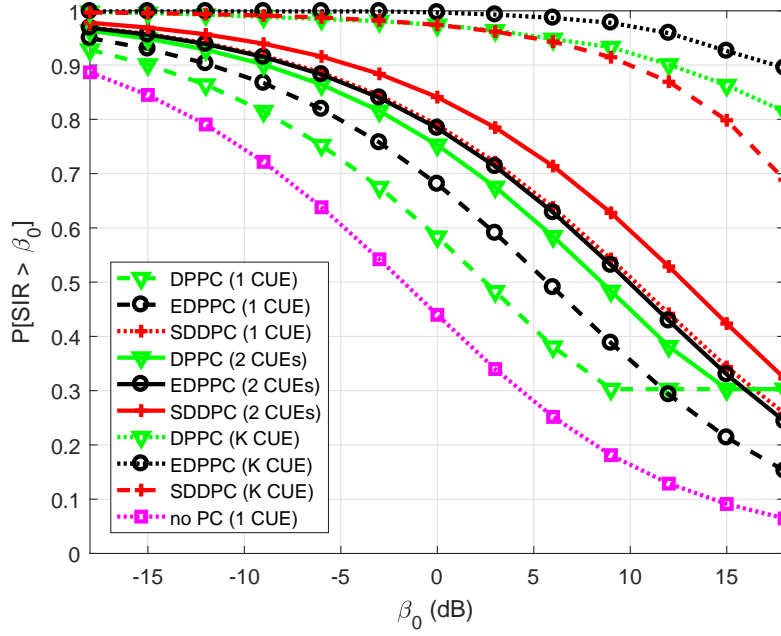


(a)

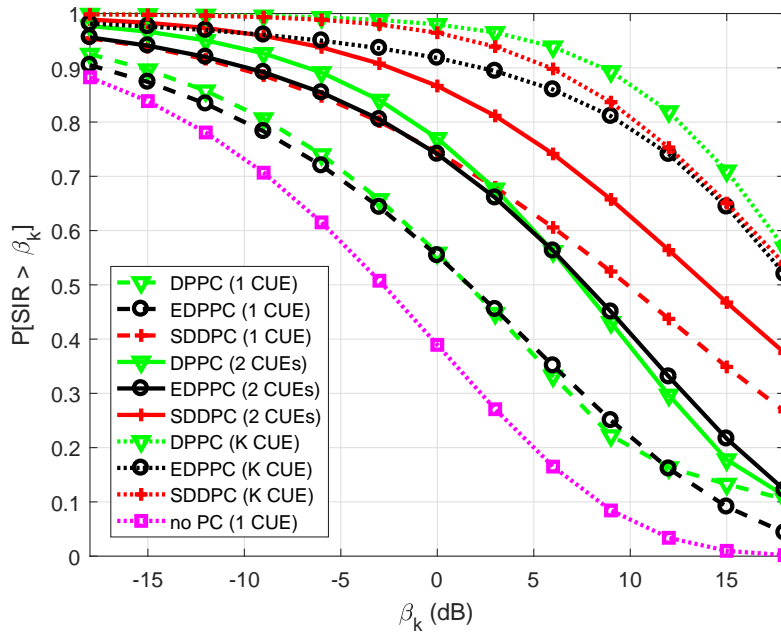


(b)

Figure 4.6: Coverage probability for D2D users using all the proposed PC schemes in this work vs. that of [1, 2]: (a) for D2D users in dense network scenario, and (b) for D2D users in sparse network scenario.



(a)



(b)

Figure 4.7: Coverage probability for: (a) cellular, and (b) D2D users, for $M = 1$, $M = 2$, and $M = K$.

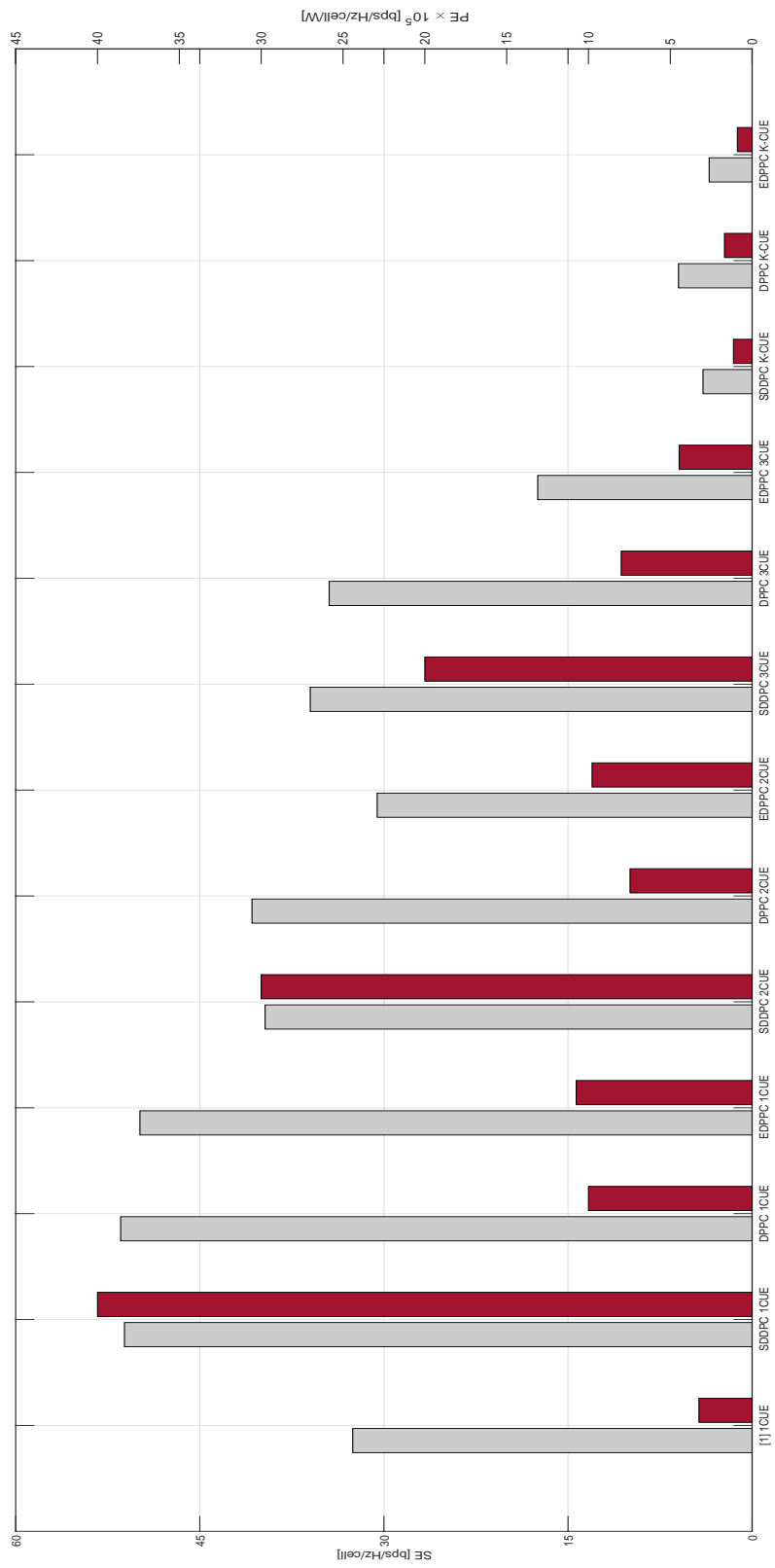


Figure 4.8: Spectral efficiency (left axis) and power efficiency (right axis) for the proposed PC schemes in a dense network.

Chapter 5

Clustering and Power Control for NOMA-MIMO systems

In this Chapter, we study the downlink of large MIMO-NOMA systems when the transmitters and receivers are assumed to have a large number of antennas. Furthermore, we propose a joint clustering and power control mechanism in which randomly distributed users in a cell are clustered and allocated different power depending on their distance from a BS while users in each cluster get served on the same time and frequency resources. While beamforming and SIC ordering are typically coupled, due to the fact that effective channel gains depend on beamforming designs, in this work, we assume uniform precoding and focus on detection. A family of QRD-based and WRD-based detectors, tailored for large MIMO-NOMA are considered. These detectors are extensions to reference subspace detectors, that were previously proposed [47] in the context of regular large MIMO systems. Simulations demonstrate that the proposed schemes are near-optimal and enable significant complexity reductions.

5.1 System Model

We consider a single-cell multiuser MIMO-NOMA setting, as shown in Fig. 5.1. The coverage region is modeled as a circular disk C with radius R_C , centered at the BS. We assume that the cellular users are divided into two groups. Users in the first group are uniformly distributed in the cell-center disk C_1 , of radius R_N , centered at the BS, while users in the second group are uniformly distributed in the cell-edge disk C_2 , from R_N to R_C .

We assume the number of users in each group to be distributed by the homogeneous Poisson point process (PPP) Φ_1 with density λ_1 in C_1 , and Φ_2 with density λ_2 in C_2 , where $\mathbb{P}[\Phi_i = q] = \exp(-\lambda_i) \frac{\lambda_i^q}{q!}$. The PPP assumption corresponds to having the expected number of nodes per unit area equal to λ_i , while the nodes are uniformly distributed over the area of interest. Moreover, the same number of users is assumed in both disks, C_1 and C_2 , which is a Poisson random variable K , with mean $\mathbb{E}[K] = \lambda_1 \pi R_N^2 = \lambda_2 \pi R_C^2 - \lambda_2 \pi R_N^2$. Hence, the total number of users in C is $2 \times \mathbb{E}[K]$.

A BS with N transmit antennas simultaneously services two users; user 1 with M_1 antennas in the inner disk (C_1), and user 2 with M_2 antennas in the outer disk (C_2), in the same frequency and time slot, via power-domain division (SC). The equivalent baseband input-output system relations are

$$\mathbf{y}_1 = \mathbf{H}_1 \mathbf{x}_1 + \mathbf{H}_1 \mathbf{x}_2 + \mathbf{n}_1 \quad (5.1)$$

$$\mathbf{y}_2 = \mathbf{H}_2 \mathbf{x}_1 + \mathbf{H}_2 \mathbf{x}_2 + \mathbf{n}_2, \quad (5.2)$$

where $\mathbf{y}_1 \in \mathcal{C}^{M_1 \times 1}$ and $\mathbf{y}_2 \in \mathcal{C}^{M_2 \times 1}$ are the received vectors at user 1 and user 2, $\mathbf{x}_1 \in \mathcal{C}^{N \times 1}$ and $\mathbf{x}_2 \in \mathcal{C}^{N \times 1}$ are the transmitted symbol vectors such that $\mathbb{E}[\mathbf{x}_1 \mathbf{x}_1^H] = p_1 \mathbf{I}_N$ and $\mathbb{E}[\mathbf{x}_2 \mathbf{x}_2^H] = p_2 \mathbf{I}_N$ (the total power is constrained by the maximum

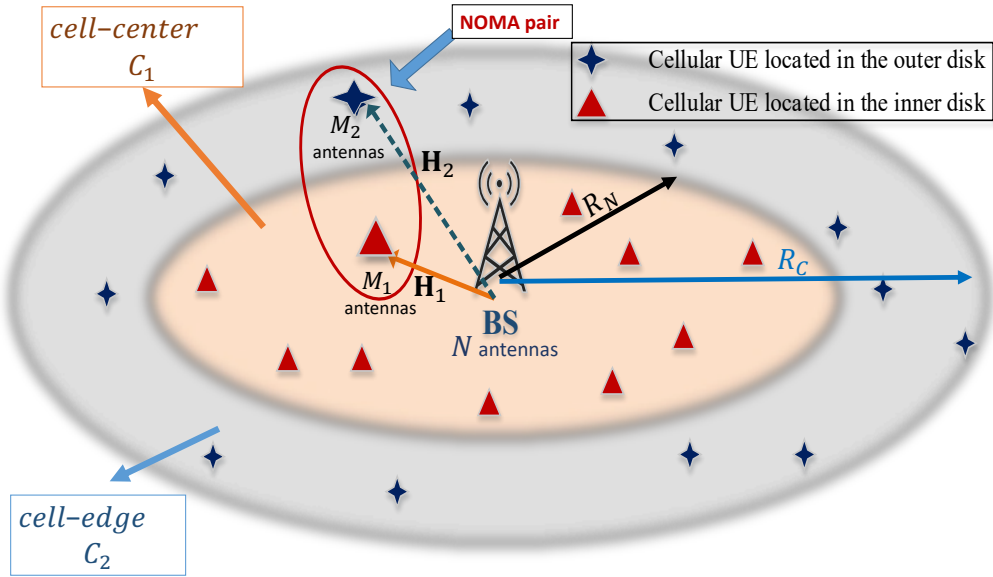


Figure 5.1: Multi-user MIMO NOMA system model

transmit power $\rho_1 + \rho_2 \leq \frac{P_{\max}}{N}$), and $\mathbf{n}_1 \in \mathcal{C}^{M_1 \times 1}$ and $\mathbf{n}_2 \in \mathcal{C}^{M_2 \times 1}$ are the $\mathcal{CN}(0, \sigma_1^2)$ and the $\mathcal{CN}(0, \sigma_2^2)$ noise vectors ($\mathbb{E}[\mathbf{n}_i \mathbf{n}_i^*] = \sigma_i^2 \mathbf{I}_{M_i}$), respectively. $\mathbf{H}_1 \in \mathcal{C}^{M_1 \times N}$ and $\mathbf{H}_2 \in \mathcal{C}^{M_2 \times N}$ are the corresponding channel matrices, which are modeled as a combination of large-scale and small scale fading. In particular, the channel matrix from the BS to k th user is

$$\mathbf{H}_k = \frac{\mathbf{G}_k}{\sqrt{d_{ck}^\alpha}}, \quad (5.3)$$

where \mathbf{G}_k denotes an $M_k \times N$ matrix whose elements represent Rayleigh fading channel gains, and d_{ck}^α denotes the distance-dependent path-loss, with d_{ck} being the distance from the BS to the k th user in the c th disk, and α is the path-loss exponent. Hence, the elements of \mathbf{H}_1 and \mathbf{H}_2 are distributed as $\mathcal{CN}(0, \sigma_{\mathbf{H}_1}^2)$ and $\mathcal{CN}(0, \sigma_{\mathbf{H}_2}^2)$, respectively, with $\sigma_{\mathbf{H}_1}$ and $\sigma_{\mathbf{H}_2}$ denoting the distance-dependent large scale fading coefficients.

NOMA is achieved by clustering users from the inner disk C_1 , with users

from the outer disk C_2 , and assigning different power levels to the multiplexed transmitted symbol vectors.

5.2 Proposed Joint Clustering and Power Control

In this section, we first propose a joint clustering and power control mechanism.

In a multi-user MIMO-NOMA setting, SC results in intra-cluster interference (ICI). Maintaining efficient user clustering, however, facilitates ICI cancellation via SIC. The SIC process distinguishes same-cluster users by the difference in their power, and users are allocated power levels based on their corresponding channel vector norms. Hence, an efficient clustering approach is to select two users with significantly different channel vector norms, i.e., to couple a far user from the BS, with a near user, in a single cluster. Motivated by this realization, we propose a joint distance-based path-loss clustering and power control scheme (JDCP).

With multi-user NOMA, SIC decoding is only required at the receiver of the strong user. In the clustering phase, user 1 with better channel conditions is considered as the strong user, and user 2 as the weak user, i.e., we have $\sigma_{\mathbf{H}_1}^2 \geq \sigma_{\mathbf{H}_2}^2$, which indicates that user 1 is a central user and user 2 is at cell-edge. Hence, the SNR at user 1 is higher than that at user 2. Consequently, user 2 will be allocated more power. In this case, user 2 will decode its own symbol \mathbf{x}_2 directly, by treating the interference caused by \mathbf{x}_1 as unknown interference, while user 1 will apply SIC to cancel out symbol \mathbf{x}_2 and then decode its own symbol \mathbf{x}_1 .

The clustering approach works as follows: First, the farthest user in disk C_1 is grouped with the farthest user in disk C_2 . Then, the second farthest user in C_1 is grouped with the second farthest user in C_2 , and so on. Hence, SIC can be

applied efficiently, since more power is allocated to the weak user.

Following clustering, we propose a low-complexity power control (PC) mechanism, that exploits the CSI of the cellular link, to minimize the interference between NOMA pairs. The NOMA pairs select their transmit power based on channel conditions, namely, the distance-based path-loss $d_{ck}^{-\alpha}$. The allocated power for the k th close user (in C_1), based on channel inversion, is given by

$$\rho_1^{(k)} = \varrho_{\text{rx}} d_{1k}^\alpha, \quad (5.4)$$

where d_{1k} is the distance between the BS and the k th user equipment (UE) in C_1 , α is the path-loss exponent, and ϱ_{rx} is the minimum required power for the UE to recover a signal (also referred to as receiver sensitivity). The power allocated to the k th far user in C_2 is thus given by

$$\rho_2^{(k)} = \min\left\{\mu \varrho_{\text{rx}} d_{2k}^\alpha, \frac{P_{\max}}{N} - \rho_1^{(k)}\right\}, \quad (5.5)$$

where μ is a NOMA PC parameter, d_{2k} is the distance between the BS and the k th UE in C_2 , and P_{\max} is the maximum transmit power.

Note here that channel inversion only compensates for the large-scale path-loss effects, and not for small-scale fading effects. Consequently, it is not required in our proposed PC scheme to establish instantaneous CSI at the transmitter. Moreover, the BS can estimate distances through location updates, as defined in the 3GPP TS 23.032 [123] universal geographical area description (GAD). Furthermore, this scheme is particularly suitable for SIC decoding, since it guarantees allocating much more power to far users and much less power for close users. This guarantees alluding the worst-case scenario of allocating equal power for both users, which must be avoided in NOMA. The JDCP scheme is summarized

Algorithm 3 Joint Distance-based Path-loss Clustering and Power Control

```
1: procedure JDCP
2:   ▷ BS has the distance vectors  $\mathbf{d}_{C_1} = [d_{11}, d_{12}, \dots, d_{1,K}]$ 
      and  $\mathbf{d}_{C_2} = [d_{21}, d_{22}, \dots, d_{2,K}]$  of the users in  $C_1$  and  $C_2$ , respectively.
3:   ▷ Initialize index vectors:  $I_1 = \{1, 2, \dots, K\}$  for users in  $C_1$ 
      and  $I_2 = \{1, 2, \dots, K\}$  for users in  $C_2$ 
4:   ▷ Initialize  $k = 1$ ,  $P_{\max}$ , and  $L = \emptyset$ 
5:   LOOP: While  $I_1 \neq \emptyset$  and  $I_2 \neq \emptyset$  do
6:     Clustering:
7:       Choose  $i_1 = \arg \max_k [\mathbf{d}_{C_1}]_k$ 
8:       Choose  $i_2 = \arg \max_k [\mathbf{d}_{C_2}]_k$ 
9:       Fix  $L \leftarrow L \cup [i_1, i_2]$ 
10:    Power Allocation:
11:     $\rho_1^{(k)} \leftarrow \varrho_{\text{rx}}\{[\mathbf{d}_{C_1}]_{i_1}\}^\alpha$ 
12:     $\rho_2^{(k)} \leftarrow \min\{\mu \varrho_{\text{rx}}\{[\mathbf{d}_{C_2}]_{i_2}\}^\alpha, \frac{P_{\max}}{N} - \rho_1^{(k)}\}$ 
13:    Save  $I_1 \leftarrow I_1 \setminus i_1$ 
14:    Save  $I_2 \leftarrow I_2 \setminus i_2$ 
15:     $k = k + 1$ .
16:    goto LOOP
17:  end
```

in Algorithm 3.

5.2.1 Multi-User MIMO-NOMA Detection

Following JDCP, user 2 decodes its symbol vector \mathbf{x}_2 directly, by treating the interference caused by \mathbf{x}_1 as unknown interference. This can be achieved by using any of the detectors presented in [47]. The considered detectors build on three QRD-based MIMO detectors, NC, CD, and LORD, as well as three WRD-based MIMO detectors [47], punctured NC (PNC), punctured CD (PCD), and the subspace detector (SSD). Hence, the resultant formulations per data stream are a simple extension to those in [47]. This concludes the operations at user 2, where no SIC is required. Hence, the detection routine at user 2 is in fact regular MIMO detection.

Nevertheless, SIC-based detection applies for user 1. First, the symbol vector

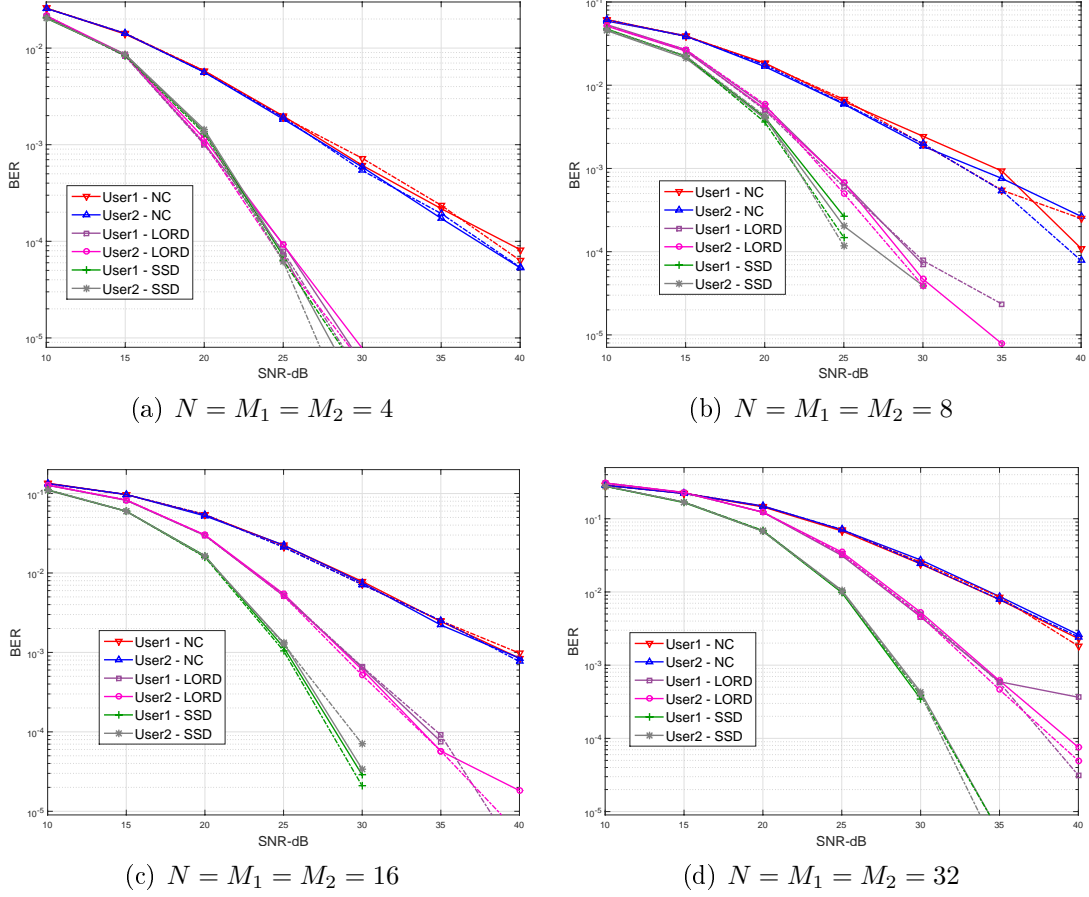


Figure 5.2: BER performance of proposed detectors in the multi-user scenario (dotted lines refer to the reference optimal power allocation scheme).

\mathbf{x}_2 is detected, while treating \mathbf{x}_1 as unknown interference (note that this stage is required since we assume no communication between users, where each user decodes its own information independently). Then, user 1 cancels the part of the received signal that is caused by \mathbf{x}_2 , and decodes \mathbf{x}_1 from the remainder of the received signal:

$$\mathbf{y}_2 = \mathbf{y}_2 - \mathbf{H}_2 \mathbf{x}_2 = \mathbf{H}_2 \mathbf{x}_1 + \mathbf{n}_2. \quad (5.6)$$

5.3 Preliminary Simulation Results and Discussions

Figure 5.2 then shows the BER plots for the multi-user setting of Sec. 5.1, where two users are accommodated per cluster. The system parameters that were used for multi-user MIMO-NOMA simulations are summarized in Table 5.1. Three different detectors were tested NC, LORD, and SSD (from [47]). The detectors were applied directly at user 2, and successively to detect both symbol vectors at user 1. Four different scenarios were simulated, all of which assume an equal number of antennas at the BS, as well as at the two users ($N = M_1 = M_2$). The proposed JDCP scheme (solid curves) was compared with a reference optimal power control scheme (dotted curves) [74], which formulates the power allocation problem as an ergodic capacity maximization problem. Note, however, that this PC scheme is of high complexity and of slow convergence, since it employs a bisection search method. To the contrary, our joint clustering and power control scheme is of low complexity, and it only relies on the distance-based path-loss parameter for channel inversion. Unlike the optimal approach, our proposed JDCP scheme guarantees allocating more power to the far user in a cluster, which is suitable for SIC. Furthermore, our proposed scheme results in lower power consumption on average, as we have $\rho_1 + \rho_2 \leq \frac{P_{\max}}{N}$, whereas in the optimal scheme, the transmission power is always P_{\max} , where $\rho_1 + \rho_2 = \frac{P_{\max}}{N}$.

Figures 5.2(a) to 5.2(d) show the results for systems with 4, 8, 16, and 32 antennas, respectively. Both, optimal power control and channel-inversion-based power control achieved similar BER performances. Furthermore, at lower antenna orders, the gap between LORD and SSD was found to be negligible. However, for 16 and 32 antenna systems, SSD clearly outperformed LORD at a lower complexity.

Table 5.1: Simulation Parameters

Parameter	Value
Cell radius (R_C)	500 m
Radius of cell-center disk C_1 (R_N)	150 m
NOMA pairs density (λ_1, λ_2)	$2.1 \times 10^{-4}, 2.1 \times 10^{-5}$
Average # NOMA pairs (K)	$\mathbb{E}[K] = \pi \lambda_1 R_N^2 \in \{15\}$
Path-loss exponent (α)	4
Max. transmit power	$P_{\max} = 100 \text{ mW} \times N$
NOMA PC parameter μ	10
Receiver sensitivity ρ_{rx}	-100 dBm
Monte-Carlo Simulations	1000

5.4 Conclusion

In this work, a large MIMO-NOMA system has been considered. A low complexity joint clustering and power control scheme has been proposed, that exploits the distance-based path-loss parameter, to guarantee efficient SIC demodulation. An architectural design has been presented, by using the detectors of lower complexity as building blocks in their more complex extensions, and the proposed schemes have been shown to achieve significant computational savings.

Chapter 6

Low-Resolution Massive MIMO

In this Chapter, we consider a massive MIMO system with low resolution ADCs on each receive antenna. We propose a new linear MMSE-based detector that incorporates the effects of coarse quantization in the ADC and the pilot-based channel estimation error. We analytically derive the achievable rate, and compare it against the capacity of a conventional MIMO system with higher order modulation and near ML detection. By using 1-bit ADCs in massive MIMO, the same achievable rate obtained as the conventional MIMO system can be attained but with significantly less power consumption even with channel estimation error. The corresponding results appeared in [48, 49].

6.1 System Model and Proposed Detection Scheme

We consider a *single-cell* uplink (UL) system as depicted in Figs. 6.2 and 6.1, where K single-antenna users are served by a BS that is equipped with an array of $N \gg K$ antennas. The sub-channels between each transmit-receive antenna

pair is modeled as a Rayleigh block-fading channel in which the channel stays constant over the channel coherence time.

The discrete-time complex baseband received signal over all antennas prior to quantization, is given as

$$\mathbf{y} = \sqrt{\rho}\mathbf{H}\mathbf{s} + \mathbf{w}, \quad (6.1)$$

where $\mathbf{y} \in \mathbb{C}^N$ is the received vector, ρ is the uplink SNR, $\mathbf{H} \in \mathbb{C}^{N \times K}$ is the channel matrix between the K users and the N BS antennas, and $\mathbf{s} \in \mathbb{C}^K$ denotes the channel input from all users. We assume that the channel gains $[\mathbf{H}]_{n,k} \sim \mathcal{CN}(0, 1)$. Similarly, the entries $[\mathbf{w}]_n$ of the additive white gaussian noise vector $\mathbf{w} \in \mathbb{C}^N$ are $\mathcal{CN}(0, 1)$ distributed. Moreover, $\mathbb{E}[\text{tr}(\mathbf{s}\mathbf{s}^H) \leq K\rho]$ in which the average power constraint is satisfied, and $\text{tr}\{\cdot\}$ represents the trace of a matrix.

6.1.1 Quantization in the ADC

The in-phase and quadrature components of the received signal at each antenna are quantized separately by an ADC of b -bit resolution. Following the notation of [24], we define a set of 2^b+1 quantization thresholds $\zeta_b = \{v_0, \dots, v_{2^b}\}$ and a set of 2^b quantization labels $\mathcal{L}_b = \{\ell_0, \dots, \ell_{2^b-1}\}$ where $\ell_i \in (v_i, v_{i+1}]$. Let $\mathcal{B}_b = \mathcal{L}_b \times \mathcal{L}_b$. The b -bit quantization is modeled by the function $Q_b(\cdot) : \mathbb{C}^N \rightarrow \mathcal{B}_b^N$ that maps the received complex vector \mathbf{y} with entries y_n to the quantized output \mathbf{r} with entries $r_n = \ell_k + j\ell_l$ if and only if $\Re\{y_n\} \in [v_k, v_{k+1})$ and $\Im\{y_n\} \in [v_l, v_{l+1})$. $\Re\{\cdot\}$ and $\Im\{\cdot\}$ denote the real and imaginary parts of a complex scalar, respectively.

For simplicity, we consider the ADCs as symmetric uniform quantizers with step size Δ . We further assume that the output of the quantizer is scaled by a constant $\vartheta \in \mathbb{R}$ as in [24], to ensure that the variance of each entry of the quantized output \mathbf{r} is $K\rho + 1$. The entries ℓ_i of the quantization labels \mathcal{L} are

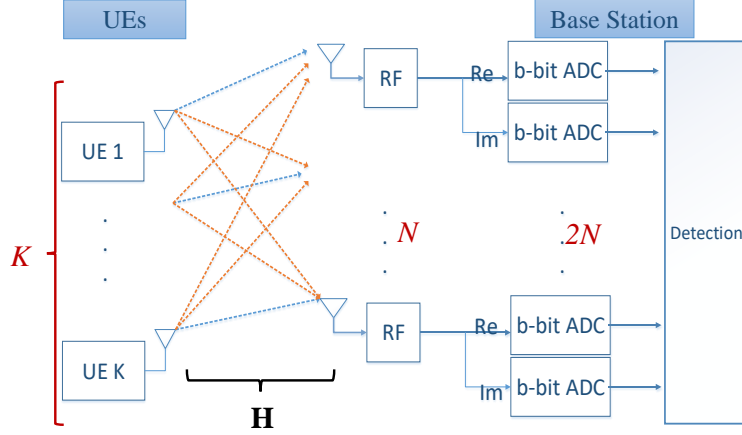


Figure 6.1: Uplink quantized massive MIMO system model

defined as

$$\ell_i = \vartheta \Delta \left(i - \frac{L-1}{2} \right), \quad i = 0, \dots, L-1. \quad (6.2)$$

where $\vartheta = \sqrt{\frac{K\rho+1}{2 \sum_{i=0}^{L-1} \ell_i^2 \left(\Phi\left(\sqrt{\frac{2v_{i+1}^2}{K\rho+1}}\right) - \Phi\left(\sqrt{\frac{2v_i^2}{K\rho+1}}\right) \right)}}$ and $\Phi(x)$ is the CDF of a standard normal random variable.

Considering uniform quantizers, the quantization thresholds are given by $v_i = \Delta \left(i - \frac{L}{2} \right)$, $i = 1, \dots, L-1$, where the step size Δ of the quantizers is chosen to minimize the distortion between the quantized and unquantized signal and can be found numerically (see e.g., [124] for details).

The b -bit quantized received signal can then be written as

$$\mathbf{r} \triangleq Q_b(\mathbf{y}) = Q_b(\sqrt{\rho}\mathbf{H}\mathbf{s} + \mathbf{w}). \quad (6.3)$$

In the 1-bit case (i.e., $b = 1$), we can write the quantized received signal r_n at the n th antenna as follows:

$$Q_1(y_n) = \sqrt{\frac{K\rho+1}{2}} (\text{sgn}(\Re\{y_n\}) + j\text{sgn}(\Im\{y_n\})), \quad (6.4)$$

where $\text{sgn}(\cdot)$ is the signum function defined as $\text{sgn}(x) = -1$ if $x < 0$ and $\text{sgn} =$

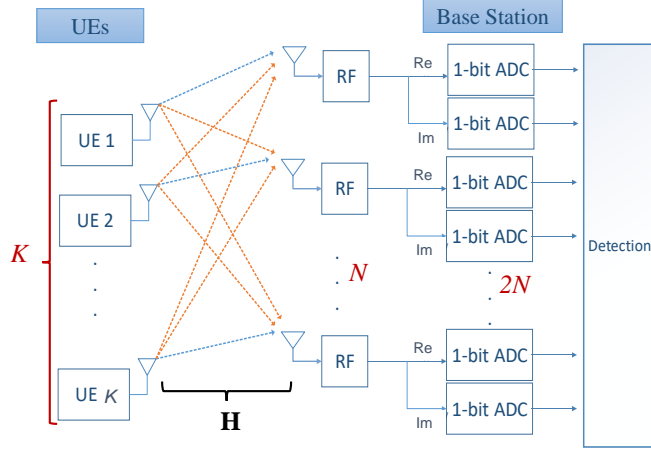


Figure 6.2: Uplink 1-bit quantized massive MIMO system model

1 if $x \geq 0$, and the quantized signal $Q_1(y_n)$ is scaled such that its variance is $K\rho + 1$.

Bussgang decomposition for Gaussian inputs: The crosscorrelation of a Gaussian signal before and after applying a non-linear operation (quantization) are equal up to a constant [125]. When the input to the quantizer is Gaussian, Bussgang's theorem [125] can be used to decompose the quantized signal into a convenient form. Using Theorem 1 in [24] and assuming $\mathbf{y} \sim \mathcal{CN}(\mathbf{0}_N, \mathbf{C}_y)$ where $\mathbf{C}_y \in \mathbb{C}^{N \times N}$, the quantized vector \mathbf{r} is linearly related to \mathbf{y} through some diagonal matrix \mathbf{G}_b

$$\mathbf{r} = \mathbf{G}_b \mathbf{y} + \mathbf{d}, \quad (6.5)$$

where the excess quantization distortion $\mathbf{d} \in \mathbb{C}^N$ and \mathbf{y} are uncorrelated. The entries of the diagonal matrix $\mathbf{G}_b = G_b \mathbf{I}_N$ are real and given by

$$G_b = \sum_{i=0}^{2^b-1} \frac{\ell_i}{\sqrt{\pi(K\rho+1)}} \left(e^{-\frac{v_i^2}{K\rho+1}} - e^{-\frac{v_{i+1}^2}{K\rho+1}} \right), \quad (6.6)$$

and the covariance matrix of \mathbf{y} satisfies $\mathbf{C}_y = (K\rho + 1)\mathbf{I}_N$.

Both the Gaussian assumption and the diagonal structure of $\mathbf{C}_y = (K\rho+1)\mathbf{I}_N$ are accurate at low SNR or when the number of UEs is large [24]. Moreover, due to the power normalization in (6.4), the covariance matrix \mathbf{C}_r of \mathbf{r} becomes $\mathbf{C}_r = (K\rho + 1)\mathbf{I}_N$, and hence, the covariance matrix of the distortion \mathbf{d} is $\mathbf{C}_d = \mathbf{C}_r - G_b^2\mathbf{C}_y = (1 - G_b^2)(K\rho + 1)\mathbf{I}_N$.

For the infinite-resolution case ($b = \infty$), it can be deduced that $G_\infty = 1$, and that for the 1-bit-ADC case ($b = 1$), we have $G_1 = \sqrt{2/\pi}$, which is a well-known result from [126] used to analyze the achievable rate with 1-bit ADCs.

6.1.2 Channel Estimation

In the channel estimation step, we assume that the coherence interval is divided into two parts: one dedicated for training and the other for data transmission. During the training phase, all K users simultaneously transmit their ($P \geq K$) sized pilot sequences to the BS. All pilot sequences used by different users are assumed to be pairwise orthogonal. Let $\Phi \in \mathbb{C}^{K \times P}$ denote the pilot matrix transmitted from the K users such that $\Phi\Phi^H = P\rho\mathbf{I}_K$. Furthermore, let $\mathbf{Y}_p = \mathbf{H}\Phi + \mathbf{W}_p$ and $\mathbf{R}_b = Q_b(\mathbf{Y}_b)$, where $\mathbf{Y}_p, \mathbf{R}_p$ and $\mathbf{W}_p \in \mathbb{C}^{N \times P}$, denote the unquantized pilot sequences, quantized pilots sequences received from the K users at the BS during the training phase and the additive noise, respectively. The linear MMSE channel estimator [24] is given by

$$\hat{\mathbf{H}} = \frac{G_b\mathbf{R}_p\Phi^H}{G_b^2P\rho + G_b^2 + (1 - G_b^2)(K\rho + 1)}. \quad (6.7)$$

Let $\mathbf{H} = \hat{\mathbf{H}} + \tilde{\mathbf{H}}$ where $\tilde{\mathbf{H}}$ represents the estimation error. The variance of the channel estimate and of the estimation error are given by:

$$\hat{\sigma}^2 = \frac{G_b^2 P \rho}{G_b^2 P \rho + G_b^2 + (1 - G_b^2)(K\rho + 1)}$$

and

$$\tilde{\sigma}^2 = \frac{G_b^2 + (1 - G_b^2)(K\rho + 1)}{G_b^2 P \rho + G_b^2 + (1 - G_b^2)(K\rho + 1)}.$$

For the unquantized case ($b = \infty, G_\infty = 1$), linear MMSE channel estimation defaults back to its original form [127].

6.1.3 Data Detection

We consider the case when the BS employs an MMSE receiver. A soft estimate \hat{s}_k of the transmitted symbol s_k from the k th user is obtained as $\hat{s}_k = \mathbf{a}_k^H \mathbf{r}$, where $\mathbf{a}_k \in \mathbb{C}^N$ denotes the linear (MMSE) receive filter for the k th user. Using (6.5), we obtain

$$\hat{s}_k = \mathbf{a}_k^H (G_b \mathbf{y} + \mathbf{d}) = \sqrt{\rho} G_b \mathbf{a}_k^H \mathbf{H} \mathbf{s} + \mathbf{a}_k^H \mathbf{n}, \quad (6.8)$$

where we have defined $\mathbf{n} = G_b \mathbf{w} + \mathbf{d}$. Note that the noise \mathbf{n} and the input vector \mathbf{s} are uncorrelated such that $\mathbf{C}_y = (K\rho + 1)\mathbf{I}_N$ holds.

We employ an MMSE-based receiver while considering the b -quantization in which the detector matrix \mathbf{A} is given by

$$\mathbf{A}^H = \left(\hat{\mathbf{H}}^H \hat{\mathbf{H}} + \frac{\tilde{\beta}_b}{G_b^2 \rho} \mathbf{I}_K \right)^{-1} \hat{\mathbf{H}}^H, \quad (6.9)$$

where $\tilde{\beta}_b = G_b^2 + (1 - G_b^2)(K\rho + 1) + K\rho G_b^2 \tilde{\sigma}^2$ represents the variance of \mathbf{n} that accounts the additive noise, the quantization effect and the estimation error.

Therefore, the k th column of \mathbf{A} can be written as

$$\mathbf{a}_k = \left(\hat{\mathbf{H}}\hat{\mathbf{H}}^H + \frac{\tilde{\beta}_b}{G_b^2\rho} \mathbf{I}_N \right)^{-1} \hat{\mathbf{h}}_k = \frac{\boldsymbol{\Upsilon}_k^{-1} \hat{\mathbf{h}}_k}{\hat{\mathbf{h}}_k^H \boldsymbol{\Upsilon}_k^{-1} \hat{\mathbf{h}}_k + 1}, \quad (6.10)$$

where, as shown in [128] but with low resolution quantization, $\boldsymbol{\Upsilon}_k \triangleq \sum_{i=1, i \neq k}^K \hat{\mathbf{h}}_i \hat{\mathbf{h}}_i^H + \frac{\tilde{\beta}_b}{G_b^2\rho} \mathbf{I}_N$.

One can note that for the case of full resolution ($b = \infty, G_\infty = 1$), the detector matrix \mathbf{A} for the linear MMSE defaults back to its original form

$$\mathbf{A}^H = \left(\hat{\mathbf{H}}^H \hat{\mathbf{H}} + \frac{1}{\rho} \mathbf{I}_K \right)^{-1} \hat{\mathbf{H}}^H. \quad (6.11)$$

6.2 Analysis of Uplink Achievable Rate

We characterize the rate achievable in a quantized massive MIMO uplink system for Gaussian inputs.

6.2.1 Sum-Rate Approximation for Gaussian Inputs

Furthermore, while the quantizer noise \mathbf{d} is **non-Gaussian**, we can obtain a lower bound on the achievable rate by making the worst-case assumption [24, 28, 29, 126, 127, 129, 130] that in fact it is Gaussian with the same covariance matrix in $\mathbf{C}_d = (1 - G_b^2) (K\rho + 1) \mathbf{I}_N$.

The paper [129] finds the worst additive noise for a communication channel under a covariance constraint. As shown in [129], for low signal powers, the worst additive noise is Gaussian with a covariance matrix in a convex set which depends on the signal power. And as shown in [127], the worst uncorrelated additive noise, wherein the noise is uncorrelated with the signal, is the Gaussian additive noise.

Using the above findings and knowing that $\hat{s}_k = \mathbf{a}_k^H \mathbf{r} = \sqrt{\rho} G_b \mathbf{a}_k^H \hat{\mathbf{H}} \mathbf{s} + \sqrt{\rho} G_b \mathbf{a}_k^H \tilde{\mathbf{H}} \mathbf{s} + \mathbf{a}_k^H \mathbf{n}$, the achievable rate can be approximated by treating the additive noise $\mathbf{a}_k^H \mathbf{n}$ in (6.8) and the channel input as Gaussian random variables. We then have the following general form for the achievable rate:

$$R_k(\rho) \approx \mathbb{E}_{\hat{\mathbf{H}}} \left[\log_2 \left(1 + \frac{\rho |\mathbf{a}_k^H \hat{\mathbf{h}}_k|^2}{\rho \sum_{j \neq k} |\mathbf{a}_k^H \hat{\mathbf{h}}_j|^2 + \tilde{\beta}_b \|\mathbf{a}_k\|^2} \right) \right] \quad (6.12)$$

where the terms in the denominator correspond to the interference, the estimation error and the quantization distortion.

Achievable rate of the proposed MMSE-based detector

Using (6.10), the signal-to-interference-plus-noise ratio can be written $\text{SINR}_{\text{MMSE}} = \hat{\mathbf{h}}_k^H \boldsymbol{\Upsilon}_k^{-1} \hat{\mathbf{h}}_k$, and by applying some straight-forward linear algebraic calculations,

$$\begin{aligned} \hat{\mathbf{H}}^H \left(\frac{\tilde{\beta}_b}{G_b^2 \rho} \mathbf{I}_N + \hat{\mathbf{H}} \hat{\mathbf{H}}^H \right)^{-1} \hat{\mathbf{H}} &= \left(\frac{\tilde{\beta}_b}{G_b^2 \rho} \mathbf{I}_K + \hat{\mathbf{H}}^H \hat{\mathbf{H}} \right)^{-1} \hat{\mathbf{H}}^H \hat{\mathbf{H}} \\ &= \mathbf{I}_K - \left(\mathbf{I}_K + \frac{G_b^2 \rho}{\tilde{\beta}_b} \hat{\mathbf{H}}^H \hat{\mathbf{H}} \right)^{-1}. \end{aligned} \quad (6.13)$$

We obtain the following approximation:

$$\begin{aligned} R_k^{\text{MMSE}}(\rho) &= \mathbb{E}_{\hat{\mathbf{H}}} \left[\log_2(1 + \hat{\mathbf{h}}_k^H \boldsymbol{\Upsilon}_k^{-1} \hat{\mathbf{h}}_k) \right] \\ &= \mathbb{E}_{\hat{\mathbf{H}}} \left[\log_2 \left(\frac{1}{1 - \hat{\mathbf{h}}_k^H \left(\frac{\tilde{\beta}_b}{G_b^2 \rho} \mathbf{I}_N + \hat{\mathbf{H}} \hat{\mathbf{H}}^H \right)^{-1} \hat{\mathbf{h}}_k} \right) \right] \\ &= \mathbb{E}_{\hat{\mathbf{H}}} \left[\log_2 \left(\frac{1}{1 - \left[\hat{\mathbf{H}}^H \left(\frac{\tilde{\beta}_b}{G_b^2 \rho} \mathbf{I}_N + \hat{\mathbf{H}} \hat{\mathbf{H}}^H \right)^{-1} \hat{\mathbf{H}} \right]_{k,k}} \right) \right] \end{aligned}$$

$$= -\mathbb{E}_{\hat{\mathbf{H}}} \left[\log_2 \left[\left(\mathbf{I}_K + \frac{G_b^2 \rho}{\hat{\beta}_b} \hat{\mathbf{H}}^H \hat{\mathbf{H}} \right)^{-1} \right]_{k,k} \right] \quad (6.14)$$

Using Jensen's inequality, we obtain the following lower bound on the approximate achievable uplink rate in (6.12):

$$R_k^{\text{MMSE}}(\rho) \geq \tilde{R}_k^{\text{MMSE}}(\rho) = \log_2 \left(1 + \frac{1}{\mathbb{E}[1/\gamma_k]} \right) \quad (6.15)$$

where $\gamma_k = \frac{1}{\left[\left(\mathbf{I}_K + \frac{G_b^2 \rho}{\hat{\beta}_b} \hat{\mathbf{H}}^H \hat{\mathbf{H}} \right)^{-1} \right]_{k,k}} - 1$.

Using a similar methodology as in [131] while considering the b -bit quantization, we approximate the exact distribution of γ_k with a Gamma distribution which has an analytically tractable form. Hence, the PDF of γ_k is given by [132]:

$$p_{\gamma_k}(\gamma) = \frac{\gamma^{\hat{\alpha}_b - 1} e^{-\gamma/\hat{\theta}_b}}{\Gamma(\hat{\alpha}_b) \hat{\theta}_b^{\hat{\alpha}_b}} \quad (6.16)$$

where $\hat{\alpha}_b = \frac{(N-K+1+(K-1)\mu)^2}{N-K+1+(K-1)\mu}$, $\hat{\theta}_b = \frac{N-K+1+(K-1)\mu}{N-K+1+(K-1)\mu} \frac{G_b^2 \rho \hat{\sigma}^2}{\hat{\beta}_b}$, and $\Gamma(\cdot)$ is the Gamma function. Moreover, μ and κ are obtained by solving following equations:

$$\begin{aligned} \mu &= \frac{1}{N \frac{G_b^2 \rho \hat{\sigma}^2}{\hat{\beta}_b} (1 - \frac{K-1}{N} + \frac{K-1}{N} \mu) + 1} \\ \kappa \left(1 + \frac{(K-1)G_b^2 \rho \hat{\sigma}^2}{\hat{\beta}_b} \mu^2 \right) &= \frac{(K-1)G_b^2 \rho \hat{\sigma}^2}{\hat{\beta}_b} \mu^3 + (K-1)\mu^2 \end{aligned}$$

Proposition 3. *Using the approximate PDF of γ_k given by (6.16), and the proposed linear MMSE-based detector, the lower bound on the achievable rate for the k th user is*

$$\tilde{R}_k^{\text{MMSE}}(\rho) = \log_2(1 + (\hat{\alpha}_b - 1)\hat{\theta}_b). \quad (6.17)$$

Proof. Substituting (6.16) into (6.15) and using the identity $\Gamma(\hat{\alpha}_b) = (\hat{\alpha}_b - 1)\Gamma(\hat{\alpha}_b - 1)$, the result follows. \square

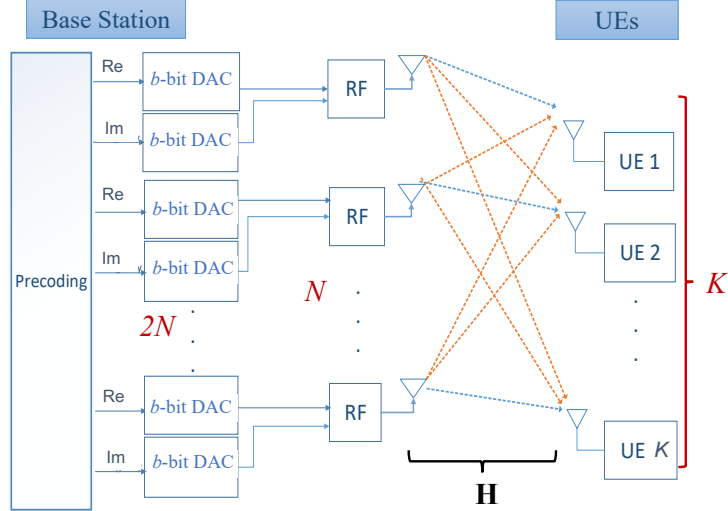


Figure 6.3: Downlink quantized massive MIMO system model

Remark: From (6.12), the achievable rate $R_k(\rho)$ can be rewritten as

$$\begin{aligned}
R_k(\rho) &= \mathbb{E}_{\hat{\mathbf{H}}} \left[\log_2 \left(1 + \frac{|\mathbf{a}_k^H \hat{\mathbf{h}}_k|^2}{\mathbf{a}_k^H \mathbf{\Upsilon}_k \mathbf{a}_k} \right) \right] \\
&\leq \mathbb{E}_{\hat{\mathbf{H}}} \left[\log_2 \left(1 + \frac{\|\mathbf{a}_k^H \mathbf{\Upsilon}_k^{1/2}\|^2 \|\mathbf{\Upsilon}_k^{-1/2} \hat{\mathbf{h}}_k\|^2}{\mathbf{a}_k^H \mathbf{\Upsilon}_k \mathbf{a}_k} \right) \right] \\
&= \mathbb{E}_{\hat{\mathbf{H}}} \left[\log_2(1 + \hat{\mathbf{h}}_k^H \mathbf{\Upsilon}_k^{-1} \hat{\mathbf{h}}_k) \right] = R_k^{\text{MMSE}}(\rho). \tag{6.18}
\end{aligned}$$

The inequality is obtained by using Cauchy-Schwarz' inequality, which holds with equality when using the proposed detector in (6.14) with $\mathbf{a}_k = \alpha \mathbf{\Upsilon}_k^{-1} \hat{\mathbf{h}}_k$, for any $\alpha \in \mathbb{C}$. Therefore, the proposed MMSE-based linear detector is optimal in the sense that it maximizes the achievable rate given by (6.12).

6.3 Extended study for downlink (DL) quantized massive MIMO

We consider the downlink of a single-cell massive MIMO system as illustrated in Fig. 6.3. The system consists of a BS with M antennas that serves K

single-antenna UEs simultaneously and in the same time-frequency resource. For simplicity, we assume that all RF hardware (e.g., local oscillators, mixers, power amplifiers, etc.) are ideal and that the ADCs at the UEs have infinite resolution. However, the BS is equipped with low resolution digital-to-analog converters (DACs). The input-output relation of the downlink channel can be modeled as

$$\mathbf{y} = \rho \mathbf{H} \mathbf{x} + \mathbf{n}. \quad (6.19)$$

The vector $\mathbf{y} = [y_1, \dots, y_K]^T$ contains the received signals at all users, with $y_k \in \mathbb{C}$ representing the signal received at the k th UE. The channel matrix $\mathbf{H} \in \mathbb{C}^{K \times N}$ models the downlink channel. We shall also assume that the entries of \mathbf{H} are independent circularly-symmetric complex Gaussian random variables with unit variance, i.e., $h_{k,n} = [\mathbf{H}]_{k,n} \sim \mathcal{CN}(0, 1)$, for $k = 1, \dots, K$, and $n = 1, \dots, N$. The vector $\mathbf{n} \in \mathbb{C}^K$ in (6.19) models additive noise. We assume the noise to be i.i.d. circularly-symmetric complex Gaussian with variance σ_n^2 per complex entry, i.e., $n_u \sim \mathcal{CN}(0, \sigma_n^2)$, for $k = 1, \dots, K$. We shall also assume that the noise level is known perfectly at the BS.

For linear-quantized precoders, the precoded vector $\mathbf{x} \in \mathcal{X}^B$ is given by

$$\mathbf{x} = Q_b(\mathbf{P}\mathbf{s}) = \mathbf{G}_b \mathbf{P}\mathbf{s} + \mathbf{d}. \quad (6.20)$$

Here, $Q_b(\cdot) : \mathbb{C}^B \rightarrow \mathcal{X}^B$ denotes the quantizer-mapping function, which is a nonlinear function that describes the joint operation of the $2N$ DACs at the BS. The precoded vector \mathbf{x} must satisfy the average power constraint

$$\mathbb{E}_{\mathbf{s}} [\|\mathbf{x}\|_2^2] \leq \rho. \quad (6.21)$$

We use the Wiener filter (WF) precoder [29, 133]:

$$\mathbf{P}^{\text{WF}} = \frac{1}{\beta^{\text{WF}}} \hat{\mathbf{H}}^{\text{H}} \left(\hat{\mathbf{H}} \hat{\mathbf{H}}^{\text{H}} + \frac{K \sigma_n^2}{\rho} \mathbf{I}_K \right)^{-1} \quad (6.22)$$

where

$$\beta^{\text{WF}} = \frac{1}{\sqrt{\rho}} \text{tr} \left(\left(\hat{\mathbf{H}} \hat{\mathbf{H}}^{\text{H}} + \frac{K \sigma_n^2}{\rho} \mathbf{I}_K \right)^{-1} \hat{\mathbf{H}} \hat{\mathbf{H}}^{\text{H}} \left(\hat{\mathbf{H}} \hat{\mathbf{H}}^{\text{H}} + \frac{K \sigma_n^2}{\rho} \mathbf{I}_K \right)^{-1} \right)^{-1/2}. \quad (6.23)$$

As shown in [29], coherent transmission of data using multiple BS antennas leads to an array gain, which depends on the realization of the fading channel. We shall assume that the k th UE is able to rescale the received signal y_k by a factor $\beta_k = (\mathbf{h}_k^T \mathbf{G}_b \mathbf{p}_k)^{-1} \in \mathbb{R}$ to compute an estimate $\hat{s}_k \in \mathbb{C}$ of the transmitted symbol s_k as follows:

$$\hat{s}_k = \beta_k y_k = s_k + \beta_k (e_k + n_k). \quad (6.24)$$

The nonlinearity introduced by the DACs prevents one to characterize the probability distribution of the error term e_k in closed form, which makes it difficult to compute the achievable rates. One can, however, lower-bound the achievable rate using the so-called ‘‘auxiliary-channel lower bound’’ [134]. As auxiliary channel, we assume that [29]

$$\tilde{s}_k = s_k + \beta_k (\tilde{e}_k + n_k), \quad (6.25)$$

where $\tilde{e}_k \sim \mathcal{CN}(0, \mathbb{E}_{\mathbf{s}}[|e_k|^2])$ has the same variance as the actual error term e_k but is Gaussian distributed. Assuming Gaussian inputs, by standard manipulations of the mutual information, we can bound the downlink achievable rate R_k^{DL} for

UE $k = 1, 2, \dots, K$ while considering the imperfect channel estimation as follows:

$$R_k^{\text{DL}} = \mathbb{E}_{\hat{\mathbf{H}}} \left[\mathcal{I} \left(s_k; \hat{s}_k \mid \hat{\mathbf{H}} \right) \right] \quad (6.26)$$

$$= \mathbb{E}_{s_k, \hat{s}_k, \hat{\mathbf{H}}} \left[\log_2 \left(\frac{f_{\hat{s}_k | s_k, \hat{\mathbf{H}}}(\hat{s}_k | s_k, \hat{\mathbf{H}})}{f_{\hat{s}_k | \hat{\mathbf{H}}}(\hat{s}_k | \hat{\mathbf{H}})} \right) \right] \quad (6.27)$$

$$\geq \mathbb{E}_{s_k, \hat{s}_k, \hat{\mathbf{H}}} \left[\log_2 \left(\frac{f_{\tilde{s}_k | s_k, \hat{\mathbf{H}}}(\hat{s}_k | s_k, \hat{\mathbf{H}})}{f_{\tilde{s}_k | \hat{\mathbf{H}}}(\hat{s}_k | \hat{\mathbf{H}})} \right) \right] \quad (6.28)$$

$$= \mathbb{E}_{\hat{\mathbf{H}}} [\log_2(1 + \gamma_k)], \quad (6.29)$$

where

$$\gamma_k = \frac{\left| \hat{\mathbf{h}}_k^T \mathbf{G} \mathbf{p}_k \right|^2}{\sum_{v \neq k} \left| \hat{\mathbf{h}}_k^T \mathbf{G} \mathbf{p}_v \right|^2 + \mathbf{h}_k^T \mathbf{C}_d \mathbf{h}_k^* + \tilde{\sigma}^2 \sum_{k=1}^K \|\mathbf{p}_k\|^2 + \sigma_n^2} \quad (6.30)$$

is the signal-to-interference-noise-and-distortion ratio (SINDR) at the k th UE, and $\mathbf{C}_d = \mathbb{E}[\mathbf{d}\mathbf{d}^H]$ denotes the covariance of the distortion \mathbf{d} . Using (6.20), the covariance of the distortion \mathbf{C}_d is obtained:

$$\mathbf{C}_d = \mathbf{C}_x - \mathbf{G} \mathbf{P} \mathbf{P}^H \mathbf{G}^H \quad (6.31)$$

where $\mathbf{C}_x = \mathbb{E}_s[\mathbf{x}\mathbf{x}^H]$ is the covariance matrix of the quantized signal $\mathbf{x} = Q_b(\mathbf{P}\mathbf{s})$, and we obtain it through Monte Carlo simulations.

6.4 Experimental Simulation Results

6.4.1 Simulation Setup

For our simulation, we consider a single-cell 1-bit massive MIMO uplink with $K = \{8, 16, 32\}$ users and $N = \{128, 256\}$ BS antennas for QPSK and Gaussian

inputs. We assume that the pilots are generated based on the Fast Fourier transform (FFT) matrix which ensures orthogonality (i.e. $\mathbf{\Phi}\mathbf{\Phi}^H = P\rho\mathbf{I}_K$) where $P = 3K$.

1. In order to compute the achievable rate for the QPSK inputs, the achievable rate is $R_k(\rho) = I(s_k; \hat{s}_k | \hat{\mathbf{H}})$ as shown in [135]. We expand the mutual information $I(s_k; \hat{s}_k | \hat{\mathbf{H}})$ as follows:

$$I(s_k; \hat{s}_k | \hat{\mathbf{H}}) = \mathbb{E}_{s_k, \hat{s}_k, \hat{\mathbf{H}}} \left[\log_2 \frac{P_{\hat{s}_k | s_k, \hat{\mathbf{H}}}(\hat{s}_k | s_k, \hat{\mathbf{H}})}{P_{\hat{s}_k | \hat{\mathbf{H}}}(\hat{s}_k | \hat{\mathbf{H}})} \right]. \quad (6.32)$$

Here, the conditional probability mass functions $P_{\hat{s}_k | s_k, \hat{\mathbf{H}}}(\hat{s}_k | s_k, \hat{\mathbf{H}})$ and $P_{\hat{s}_k | \hat{\mathbf{H}}}(\hat{s}_k | \hat{\mathbf{H}}) = E_{s_k} [P_{\hat{s}_k | s_k, \hat{\mathbf{H}}}(\hat{s}_k | s_k, \hat{\mathbf{H}})]$ are needed to compute (6.32). We use Monte-Carlo simulations to estimate them since no closed-form expressions are available for these quantities. In particular, we simulate many noise and interference realizations, and map the resulting \hat{s}_k to points over a rectangular grid in the complex plane.

2. A conventional MIMO system with higher-order modulation can be developed that uses near ML detection and achieves capacity that is upper bounded by [135]:

$$R^{\text{conventional}}(\rho) = \mathbb{E}_{\mathbf{H}} \left[\log_2(\det\{\mathbf{I}_N + \frac{\rho}{K}\mathbf{H}\mathbf{H}^H\}) \right], \quad (6.33)$$

where $\det\{\cdot\}$ corresponds to the determinant of a matrix.

6.4.2 Achievable Rates with perfect and imperfect CSI

Moreover, we evaluate the validity of our closed-form expression for the achievable rate for the MMSE-based linear detector given in (6.17) for Gaussian inputs with

perfect and imperfect CSI. In Fig. 6.4, we show the exactness of the proposed closed form of the MMSE-based detector (6.17) with the simulated form (6.12). One can notice that, the closed form achievable rate perfectly matches with the simulated rates for perfect and imperfect CSI. This indicates that our derived expression (6.17) is a valid predictor for the performance of 1-bit massive MIMO system.

Furthermore, in Fig. 6.5, we show the accuracy of the proposed closed form of the MMSE-based detector (6.17) with the simulated form (6.12) for low bit resolution ADCs ($b = \{1, 2, 3\}$). One can notice that the closed form achievable rate perfectly matches with Monte Carlo simulated rates for perfect and imperfect CSI. This indicates that our derived expression (6.17) is a valid predictor for the performance of b -bit massive MIMO system.

In addition, we compare the sum rate between the 1-bit massive MIMO with linear detection and the conventional MIMO systems with near ML detection. Figure 6.6 shows the sum rate versus the SNR for the two systems. It can be seen that the proposed MMSE-based detector outperform the ZF detector as the number of antennas at the BS decrease for both QPSK and Gaussian inputs. The curves illustrate that the SNR regimes are bifurcated into two regions in which for the low SNR regime the massive MIMO system can out perform the conventional MIMO even with imperfect channel estimation; however for high SNR the conventional MIMO system with a near ML detector can out perform the massive MIMO system. For instance, to achieve a sum rate of 62 bits/channel use for the one bit massive MIMO case with $N = 256$ antennas at BS and $K = 32$ users the needed SNR is -3 dB with just QPSK modulation; however, for a classical large MIMO (e.g., 16×16) system with near ML detection the needed SNR is 15 dB, and for an 8×8 MIMO system the needed SNR is around

25 dB. Therefore, Fig. 6.6 shows that the 1-bit massive MIMO achieves higher rates than the conventional MIMO at low SNR values taking into account the imperfect channel estimation.

Moreover, figure 6.7 compares the sum rate between the uplink b -bit quantized massive MIMO with linear detection against the conventional MIMO systems with near ML detection, assuming imperfect channel estimation. For the $b = 1$ bit quantization case, the SNR regimes are bifurcated into two regions: for the low SNR regime, the massive MIMO system can outperform the conventional MIMO even with imperfect channel estimation; however, for high SNR, the conventional MIMO system with a near-ML detector can outperform the massive MIMO system. For instance, to achieve a sum rate of 62 bits/channel use for the one bit massive MIMO case with $N = 256$ antennas at BS and $K = 32$ users the needed SNR is -6 dB with just QPSK modulation; however, for a large MIMO (e.g., 16×16) system with near-ML detection the needed SNR is 15 dB, and for an 8×8 MIMO system the needed SNR is around 25 dB. Furthermore, it can be seen that for few bits (i.e. 2 or 3 bits) of quantization, the proposed MMSE-based detector with massive MIMO deployment outperforms the conventional MIMO.

Finally, to complete the comparison study, figure 6.8 compares the sum rate between the downlink b -bit quantized massive MIMO with linear detection against the conventional MIMO systems with near ML detection, assuming imperfect channel estimation. The same conclusions are formed as the uplink case, wherein similarly for the $b = 1$ bit quantization case, the SNR regimes are bifurcated into two regions: for the low SNR regime, the downlink massive MIMO system can outperform the conventional MIMO even with imperfect channel estimation; however, for high SNR, the conventional MIMO system with a near-ML detector can outperform the massive MIMO system. Furthermore, it can be seen that

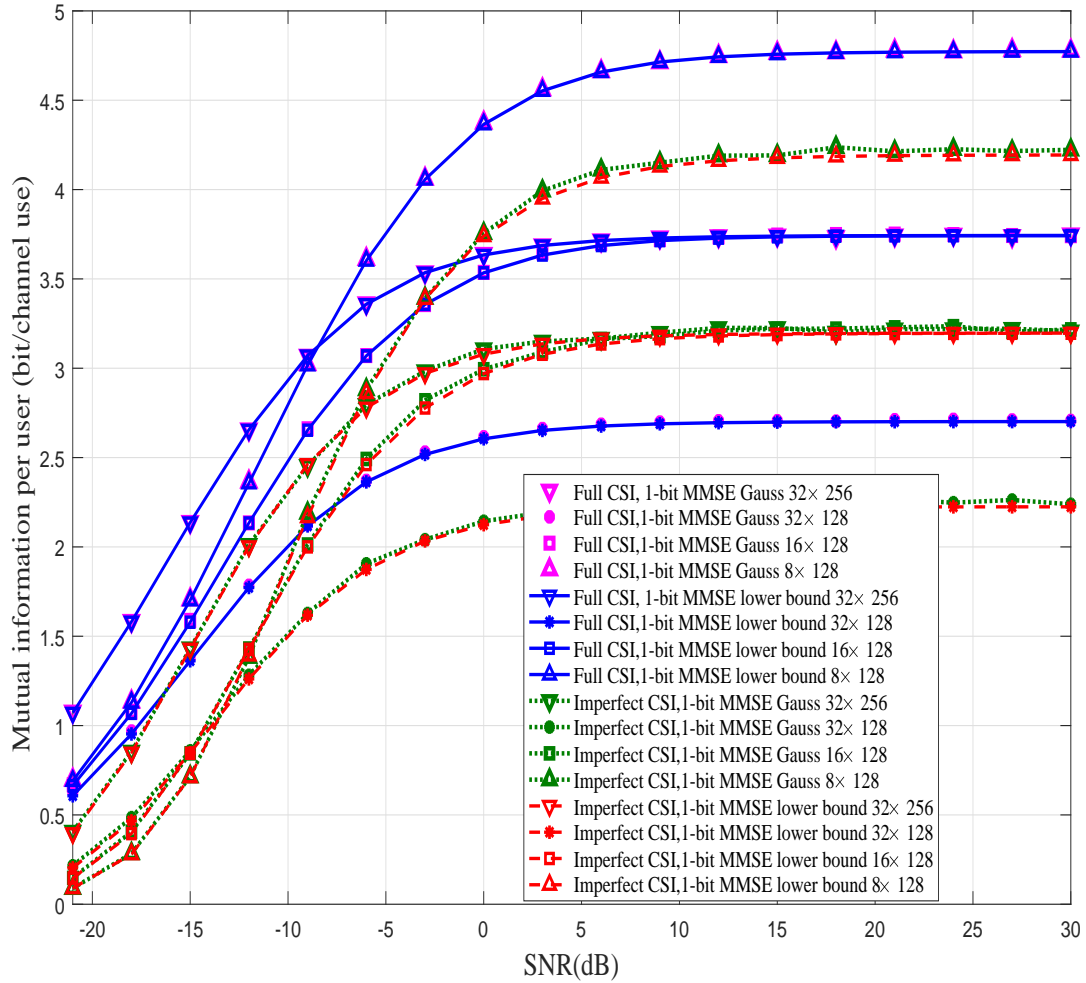


Figure 6.4: Mutual information per user versus SNR for a $K \times N$ massive MIMO system where $K = 8, 16, 32$ users and $N = \{128, 256\}$ BS antennas.

for few bits (i.e. 2 or 3 bits) of quantization, the quantized massive MIMO deployment outperforms the conventional MIMO.

6.5 Conclusion

In this work, a quantized massive MIMO system is considered. Using the Busgang decomposition, a new MMSE-based linear detection scheme, that incorporates the non-linear effects of quantization and the pilot-based channel estimation,

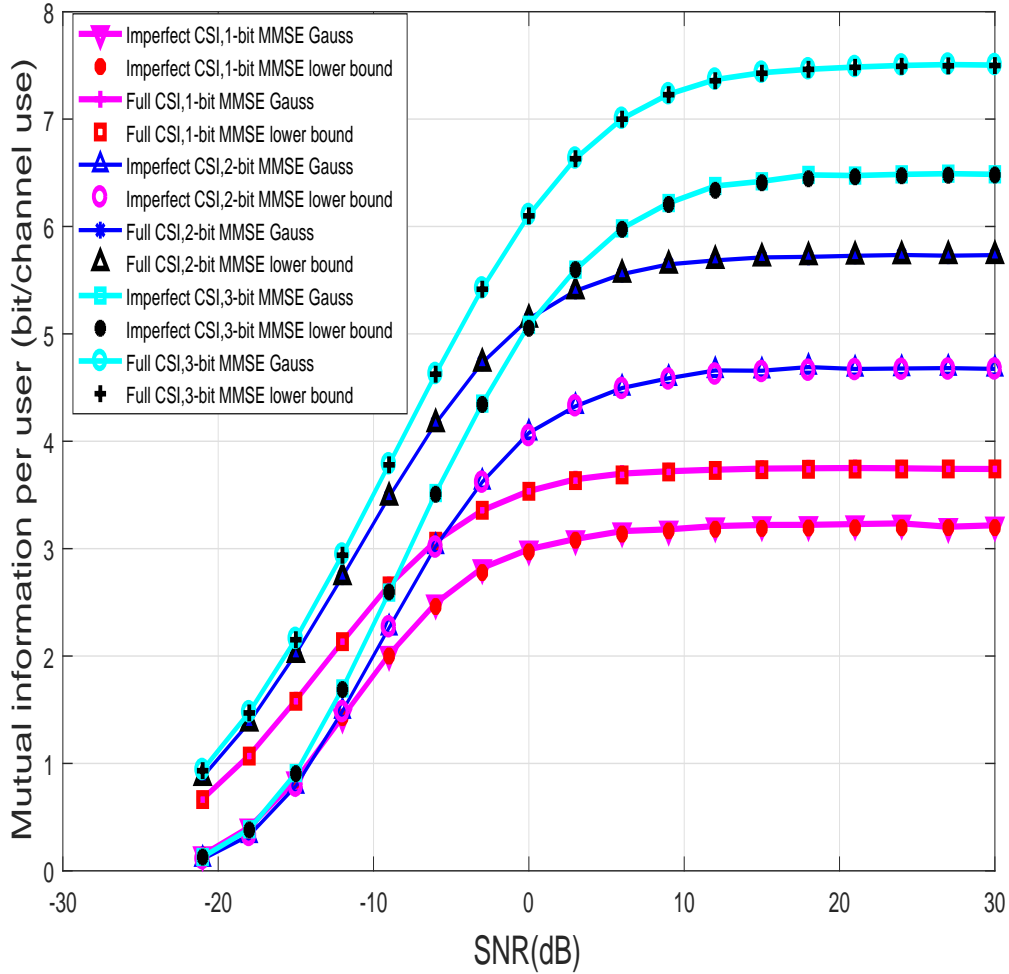


Figure 6.5: Mutual information per user versus SNR for a $K \times N$ massive MIMO system where $K = 16$ users and $N = 128$ BS antennas and $b = \{1, 2, 3\}$ quantization bits; analytical versus simulated for the proposed MMSE-based detection with imperfect channel estimation.

has been derived for the uplink case. A closed form expression for the uplink achievable rate has been derived, and used to analyze and compare the performance of 1-bit massive MIMO system with perfect and imperfect CSI against a large MIMO system that employs higher-order modulation. In particular, it has been shown the SNR is bifurcated into regions where, for low SNR regions, a 1-bit massive MIMO system with channel estimation error can achieve a higher throughput compared to a large MIMO system, while for high SNR regions, a

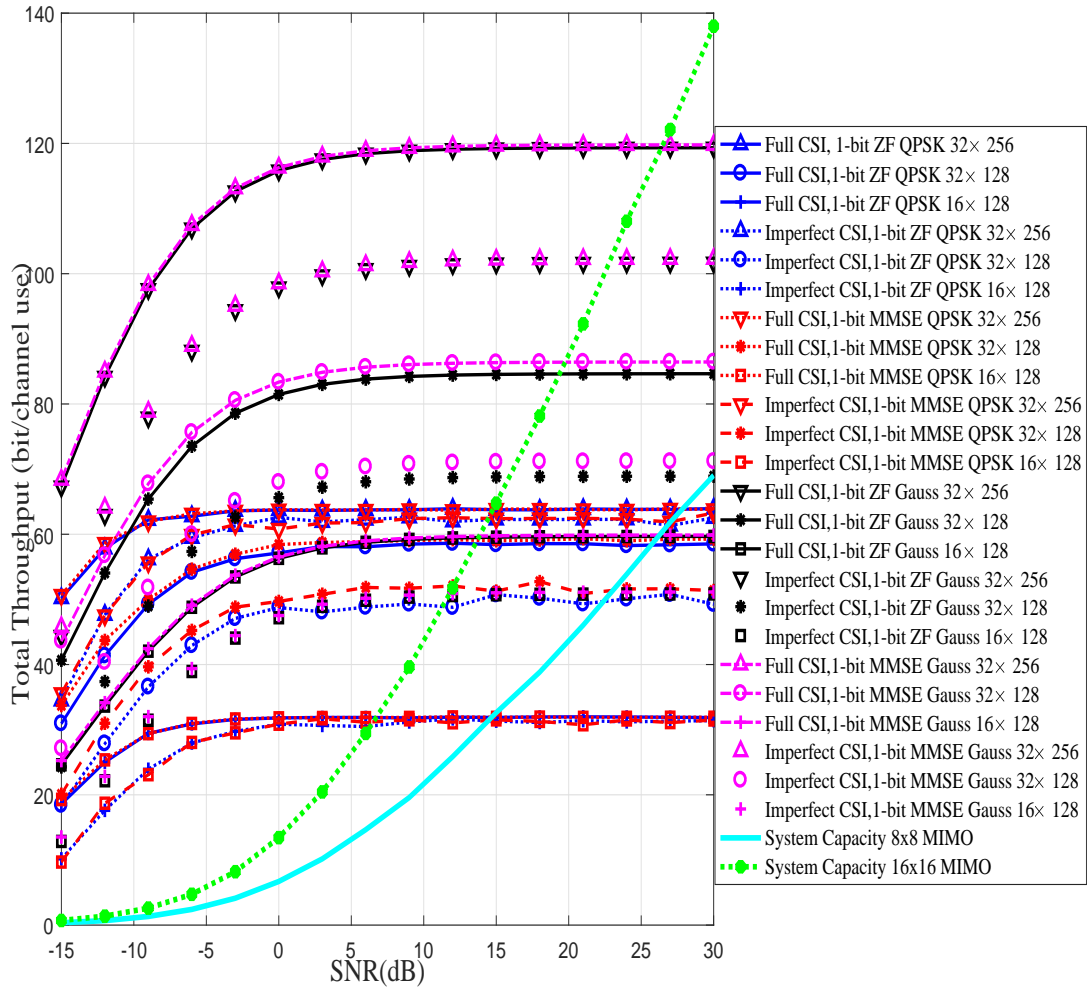


Figure 6.6: A comparison of the total system throughput for a $K \times N$ quantized Massive MIMO where where $K = \{8, 16, 32\}$ users and $N = \{128, 256\}$ versus Conventional MIMO (8×8 and 16×16) systems.

large MIMO system with a near-ML detector can outperform a massive MIMO system. Moreover, it has been shown that for a few bits of quantization (e.g., 2 or 3 bits), the quantized massive MIMO can still outperform the conventional MIMO.

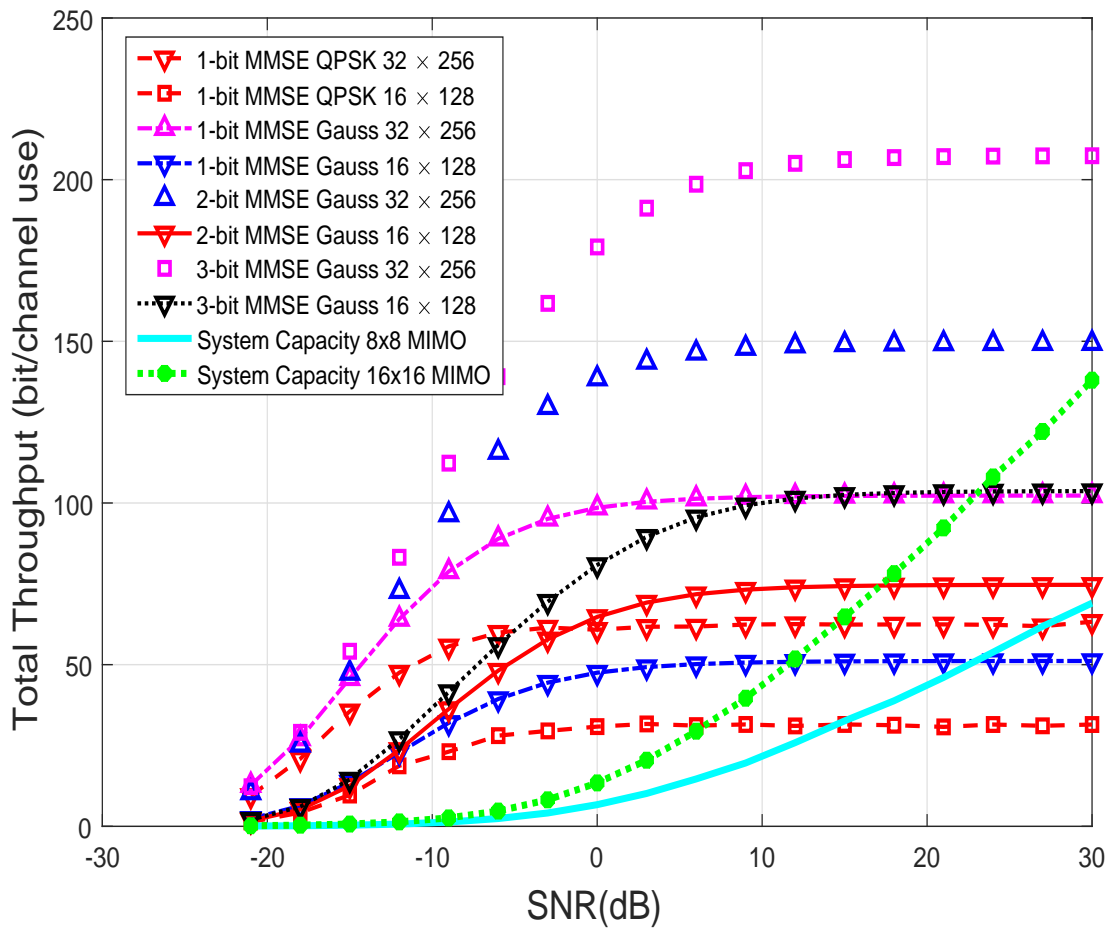


Figure 6.7: Comparison of total system throughput for a $K \times N$ quantized b -bit UL massive MIMO with $K = \{16, 32\}$ users and $N = \{128, 256\}$ with imperfect channel estimation, vs. two conventional 8×8 and 16×16 MIMO systems.

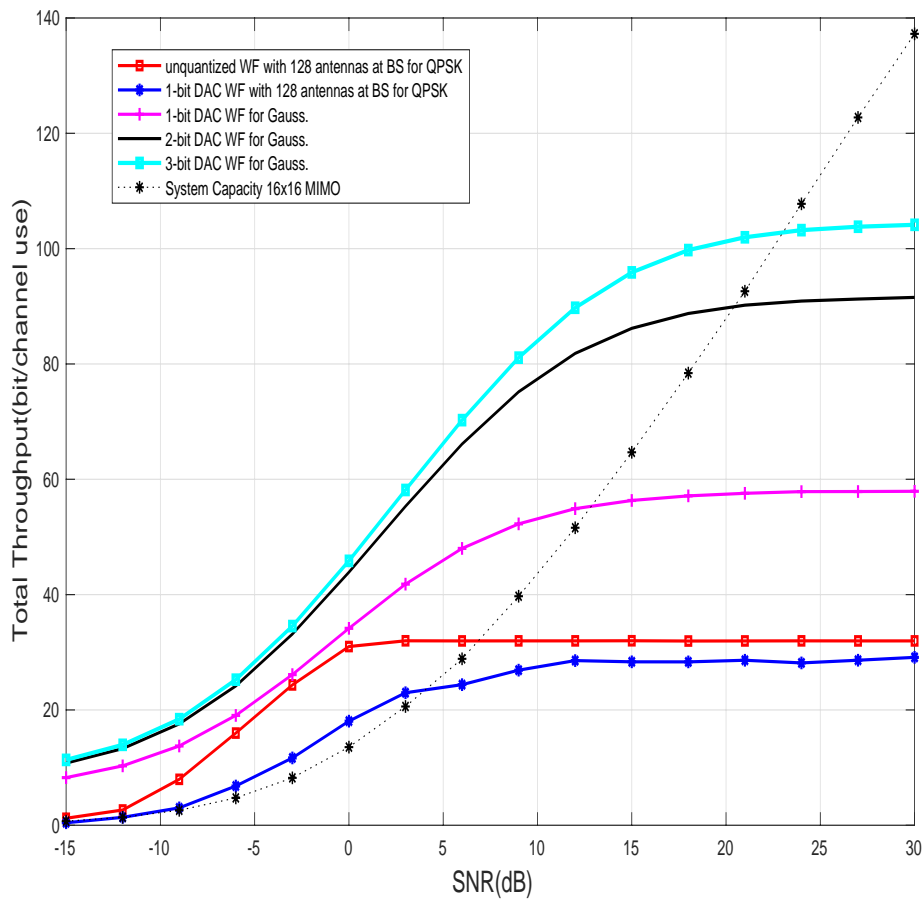


Figure 6.8: Comparison of total system throughput for a $K \times N$ quantized b -bit DL massive MIMO with $K = 16$ users and $N = 128$ with imperfect channel estimation, vs. conventional 16×16 MIMO systems.

Chapter 7

Array Signal Processing For FDD-based Cell Free Massive MIMO

In this chapter, we consider a cell-free massive MIMO system with multiple antennas at each AP operating in FDD mode that do not require any feedback from the user. By exploiting the angle reciprocity and angle coherence time, we propose a multipath component estimation for the AoA and large scale fading coefficients based on DFT operation and log likelihood function with reduced overhead. We further derive a closed form expression for the MSE of the AoA estimation and large scale fading estimation. Both theoretical and numerical results are provided to verify the effectiveness of the proposed methods. In addition, we propose linear angle-based beamforming/combining techniques for the downlink/uplink transmission that incorporate the estimated AoA and large-scale fading components. Interestingly, the proposed schemes scale only with the number of served users rather than the total number of serving antennas, and need to be updated every angle coherence time. Therefore, the impact of signaling

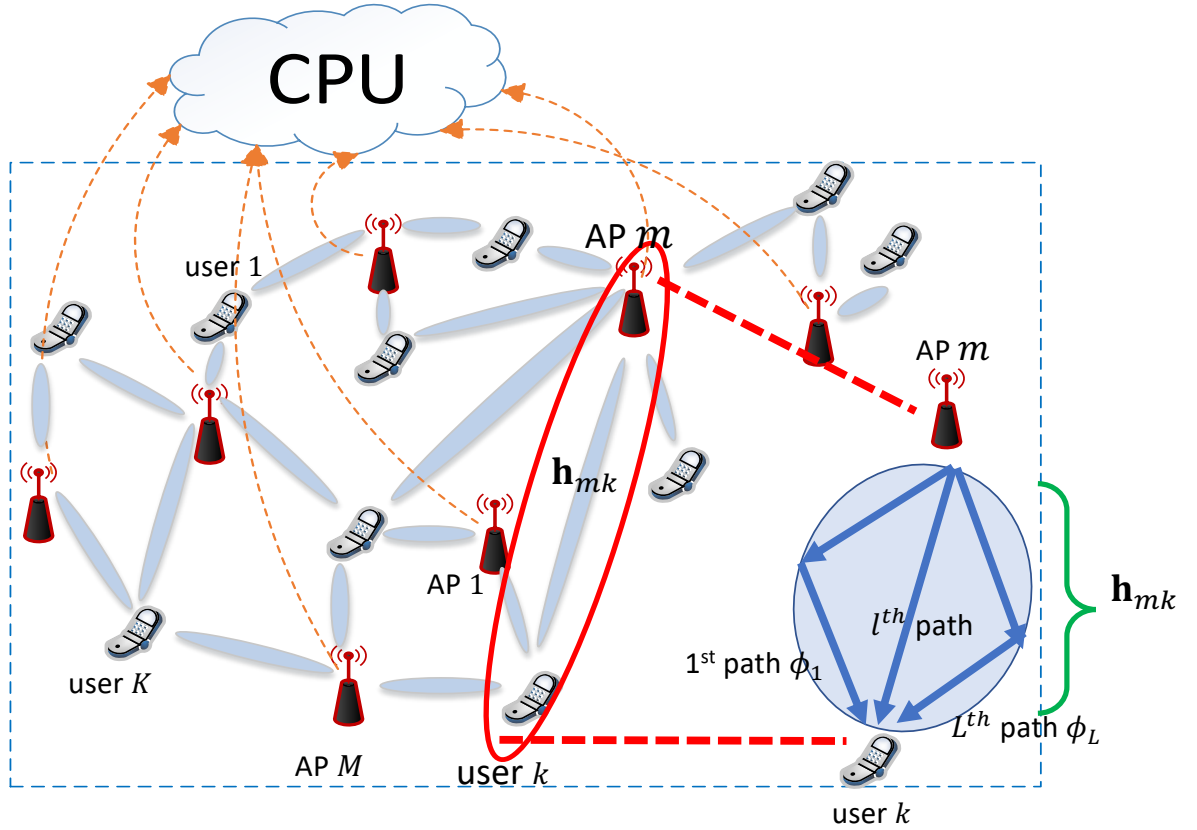


Figure 7.1: Cell-free massive MIMO system model

overhead is substantially reduced with the proposed schemes. The corresponding results have been published in parts in [50, 51].

7.1 System Model

As shown in Fig. 7.1, we consider an FDD-based cell-free massive MIMO system having M APs, each equipped with a uniform linear array (ULA) of N antennas, serving K users with single antennas. We assume a geometric channel model with L propagation paths [114, 116]. Moreover, AoAs (or angle-of-departures (AoDs)), large-scale fading and small-scale fading coefficients are called the multipath components of the channel. Due to angle reciprocity in FDD

systems [114], and frequency in-dependency, we assume that 1) the uplink AoA and downlink AoD are similar, and 2) the uplink and downlink large-scale fading coefficients (slow fading and distant-dependent path loss components) are similar [136, 137]. However, uplink and downlink small-scale fading coefficients in FDD systems are distinct since they are frequency dependent [136, 137]. Therefore, the $N \times 1$ channel vectors can be expressed as [114, 116]

$$\mathbf{h} = \sqrt{\frac{1}{L}} \sum_{l=1}^L \sqrt{\beta_l} \alpha_l \mathbf{a}(\phi_l), \quad (7.1)$$

where $\alpha_l \sim \mathcal{CN}(0, 1)$ is the complex gain of the l th path that represents the small-scale Rayleigh fading, and β_l is the large-scale fading coefficient that accounts for path-loss and shadowing effects. The variable $\phi_l \in [0, 2\pi]$ is the angle of arrival of the l th path. The array steering vector $\mathbf{a}(\phi_l)$ is defined a

$$\mathbf{a}(\phi_l) = \frac{1}{\sqrt{N}} [1, e^{j\eta \sin(\phi_l)}, \dots, e^{j(N-1)\eta \sin(\phi_l)}]^\top, \quad (7.2)$$

where $\eta = \frac{2\pi u}{\lambda}$, u is the antenna spacing, and λ is the channel wavelength (Note that we also define $v_l = \eta \sin(\phi_l)$). Equivalently, the channel vector in (7.1) can be expressed in matrix-vector form as

$$\mathbf{h} = \sqrt{\frac{1}{L}} \mathbf{A} \mathbf{B} \boldsymbol{\alpha}, \quad (7.3)$$

where

$$\mathbf{A}_{N \times L} = [\mathbf{a}(\phi_1), \dots, \mathbf{a}(\phi_L)], \quad (7.4)$$

$$\mathbf{B}_{L \times L} = \text{diag}(\sqrt{\beta_1}, \dots, \sqrt{\beta_L}), \quad (7.5)$$

$$\boldsymbol{\alpha}_{L \times 1} = [\alpha_1, \dots, \alpha_L]^\top. \quad (7.6)$$

As mentioned previously, the quantities $\boldsymbol{\alpha}$ are dependent on frequency; however \mathbf{B} and \mathbf{A} are constant with respect to frequency over *angle coherence time* interval (as discussed in subsection 7.2.4).

To model a realistic system where we have non-ideal angle reciprocity, we assume that the differences between uplink and downlink multipath components, $\tilde{v}_l^{\text{u/d}}$ and $\tilde{\beta}_l^{\text{u/d}}$, are i.i.d. random variables with zero mean and variance $\sigma_v^2, \sigma_\beta^2 \ll 1$ [138].

7.1.1 Uplink Training

Let $\mathbf{p}_k \in \mathbb{C}^{1 \times \tau}$ be the uplink (UL) pilot signal sent by the k th user composed of τ symbols with unit norm. All pilot sequences used by different users are assumed to be pairwise orthogonal, since the angle coherence time is much longer than the conventional channel coherence time [43]. Therefore, we can assign a sufficiently large number to τ such that $\tau \geq K$ holds true.

Therefore, the received signal $\mathbf{Y}_{mk} \in \mathbb{C}^{N \times \tau}$ at the m th AP sent by the k th user is given by

$$\mathbf{Y}_{mk} = \sqrt{\rho} \mathbf{h}_{mk} \mathbf{p}_k + \mathbf{N}_{mk}, \quad (7.7)$$

where ρ is the uplink transmit power and the entries $[\mathbf{N}_{mk}]_{n,i}$ of the additive white Gaussian noise matrix $\mathbf{N}_{mk} \in \mathbb{C}^{N \times \tau}$ are independent and identically distributed (i.i.d.) $\mathcal{CN}(0, \sigma_n^2)$ random variables. Multiplying (7.7) by \mathbf{p}_k^H and collecting T samples, we have

$$\begin{aligned} \mathbf{Y}_{mk}(t) \mathbf{p}_k^H &= \sqrt{\frac{\rho}{L}} \mathbf{A}_{mk} \mathbf{B}_{mk} \boldsymbol{\alpha}_{mk}(t) + \mathbf{N}_{mk} \mathbf{p}_k^H \\ &= \sqrt{\rho} \mathbf{A}_{mk} \mathbf{d}_{mk}(t) + \bar{\mathbf{n}}_{mk}, \quad t = 1, \dots, T, \end{aligned} \quad (7.8)$$

where $\mathbf{d}_{mk} = \frac{1}{\sqrt{L}}\mathbf{B}_{mk}\boldsymbol{\alpha}_{mk}$ and $\bar{\mathbf{n}}_{mk} = \mathbf{N}_{mk}\mathbf{p}_k^H \sim \mathcal{CN}(\mathbf{0}_{N \times 1}, \sigma_n^2 \mathbf{I}_N)$. Then, the T samples of (7.8) are collected in a matrix form as

$$\bar{\mathbf{Y}}_{mk} = \sqrt{\rho}\mathbf{H}_{mk} + \bar{\mathbf{N}}_{mk} = \sqrt{\rho}\mathbf{A}_{mk}\mathbf{D}_{mk} + \bar{\mathbf{N}}_{mk}, \quad (7.9)$$

where $\bar{\mathbf{Y}}_{mk} = [\mathbf{Y}_{mk}(1)\mathbf{p}_k^H, \dots, \mathbf{Y}_{mk}(T)\mathbf{p}_k^H]$, $\mathbf{H}_{mk} = [\mathbf{h}_{mk}(1), \dots, \mathbf{h}_{mk}(T)]$, $\mathbf{D}_{mk} = [\mathbf{d}_{mk}(1), \dots, \mathbf{d}_{mk}(T)]$, and $\bar{\mathbf{N}}_{mk} = [\bar{\mathbf{n}}_{mk}(1), \dots, \bar{\mathbf{n}}_{mk}(T)]$.

The multipath components estimation is performed in a distributed fashion, in which each AP *independently* estimates the multipath components to the K users. The APs do not cooperate on the multipath components estimation, and no estimates need to be shared among the APs.

7.1.2 Downlink Payload Data Transmission

The APs, based on the estimated multipath components, independently apply $N \times 1$ beamforming vector $\hat{\mathbf{w}}_{mk}$ to transmit signals to the K users. Moreover, APs do not cooperate on the beamforming vectors. The transmit DL signal from the m th AP is given by

$$\mathbf{x}_m = \sqrt{\rho^d} \sum_{k=1}^K \hat{\mathbf{w}}_{mk} s_k^d, \quad (7.10)$$

where s_k^d is the data symbol for the k th user satisfying $\mathbb{E}[|s_k^d|^2] = 1$, and ρ^d is the maximum transmit power satisfying, $\mathbb{E}[|\mathbf{x}_m|_2^2] \leq \rho^d$. It can be noted here that the multiplexing order is equal to 1.

Then, the received downlink signal at the k th user is given by

$$r_k^d = \sum_{m=1}^M \mathbf{h}_{mk}^H \mathbf{x}_m + n_k^d$$

$$= \underbrace{\sqrt{\rho^d} \sum_{m=1}^M \mathbf{h}_{mk}^H \hat{\mathbf{w}}_{mk} s_k^d}_S + \underbrace{\sqrt{\rho^d} \sum_{j \neq k}^K \sum_{m=1}^M \mathbf{h}_{mj}^H \hat{\mathbf{w}}_{mj} s_j^d}_I + n_k^d, \quad (7.11)$$

where $n_k^d \sim \mathcal{CN}(0, \sigma_n)$ is the additive noise at the k th user. Note that the received signal can be decomposed into three parts: 1) desired signal part (S), 2) interference part (I), and 3) noise n_k^d . Moreover, the k th user can detect signal s_k^d from r_k^d .

7.1.3 Uplink Payload Data Transmission

In the uplink, all K users simultaneously send their data symbols s_k^u , where $\mathbb{E}\{|s_k^u|^2\} = 1$, to the APs. It can be noted here that the multiplexing order is equal to 1. The received UL signal at the m th AP is given by

$$\mathbf{y}_m^u = \sqrt{\rho^u} \sum_{k=1}^K \mathbf{h}_{mk} s_k^u + \mathbf{n}_m^u, \quad (7.12)$$

where ρ^u is the uplink transmit power and \mathbf{n}_m^u is additive noise at the m th AP. The noise entries ($[\mathbf{n}_m^u]_i$) are modeled as i.i.d. $\mathcal{CN}(0, \sigma_n^2)$. The received signal is multiplied by the $N \times 1$ combiner $\hat{\mathbf{v}}_{mk}$ at each AP where the resulting signal is sent to the CPU through a backhaul to detect the signal. The CPU will receive

$$r_k^u = \sum_{m=1}^M \hat{\mathbf{v}}_{mk}^H \mathbf{y}_m^u = \sum_{k'=1}^K \sum_{m=1}^M \sqrt{\rho^u} \hat{\mathbf{v}}_{mk}^H \mathbf{h}_{mk'} s_{k'}^u + \sum_{m=1}^M \hat{\mathbf{v}}_{mk}^H \mathbf{n}_m^u. \quad (7.13)$$

Then, s_k is detected from r_k^u .

The main system parameters are summarized in Table 7.1.

Table 7.1: System Parameters

Number of APs, and number of antennas per AP	M, N
Total number of users	K
Number of paths	L
Channel gain for the m th AP and k th user	\mathbf{h}_{mk}
Angular steering vector for the l th path	$\mathbf{a}(\phi_l)$
Angular steering matrix for the m th AP and k th user	\mathbf{A}_{mk}
Large scale fading matrix	\mathbf{B}_{mk}
Small scale fading vector	$\boldsymbol{\alpha}_{mk}$
$N \times N$ DFT matrix	\mathbf{F}_N

7.2 Proposed Angle information aided channel estimation for FDD systems

In this section, we present the FDD-based cell-free massive MIMO systems that directly acquire multipath components from the uplink pilot signal and use them for the AP cooperation. Using array signal processing, we first present the low complexity DFT-based AoA estimation, and then we propose the large scale fading estimation based on the estimated angle information. Note that we need to estimate both components (AoA, and large scale fading) for every angle coherence interval, in order to apply low complexity beamforming/combining techniques.

7.2.1 AoA Estimation Algorithm

1. **Initial AoA Estimation:** Based on the classical DFT estimation approach, we first define a normalized $N \times N$ DFT matrix \mathbf{F}_N whose (n, q) th element is given by $[\mathbf{F}_N]_{nq} = \frac{1}{\sqrt{N}} e^{-j \frac{2\pi nq}{N}}$. In addition, we define the normalized DFT of the channel matrix \mathbf{h}_{mk} as $\mathbf{h}_{mk}^{\text{DFT}} = \mathbf{F}_N \mathbf{h}_{mk}$ whose q th element is computed as

$$[\mathbf{h}_{mk}^{\text{DFT}}]_q = \frac{1}{\sqrt{N}} \sum_{n=0}^{N-1} [\mathbf{h}_{mk}]_n e^{-j \left(\frac{2\pi}{N} nq \right)}$$

$$\begin{aligned}
&= \frac{1}{\sqrt{NL}} \sum_{l=0}^{L-1} \sum_{n=0}^{N-1} \sqrt{\beta_{l,mk}} \alpha_{l,mk} e^{-j\left(\frac{2\pi}{N}nq - n\eta \sin(\phi_{l,mk})\right)} \\
&= \frac{1}{\sqrt{NL}} \sum_{l=0}^{L-1} \sqrt{\beta_{l,mk}} \alpha_{l,mk} e^{-j\frac{N-1}{2}\left[\frac{2\pi}{N}q - \eta \sin(\phi_{l,mk})\right]} \cdot \frac{\sin\left[\left(\frac{2\pi}{N}q - \eta \sin(\phi_{l,mk})\right)\frac{N}{2}\right]}{\sin\left[\left(\frac{2\pi}{N}q - \eta \sin(\phi_{l,mk})\right)\frac{1}{2}\right]}.
\end{aligned} \tag{7.14}$$

It is noted that with infinite number of antennas in the array, i.e., $N \rightarrow \infty$, there always exist integers $q_l = \frac{Nv_{l,mk}}{2\pi}$ (for $l = 1, \dots, L$), such that $[\mathbf{h}_{mk}^{\text{DFT}}]_{q_l} = \frac{\sqrt{\beta_{l,mk}}\alpha_{l,mk}}{\sqrt{NL}}$ and $v_{l,mk} = \eta \sin(\phi_{l,mk})$, while the other elements of $\mathbf{h}_{mk}^{\text{DFT}}$ are all zero [113, 115]. Hence, all powers are concentrated on the q_l th elements.

However, in practical antenna design, the array aperture cannot be infinitely large in cell-free massive MIMO communication systems. In this case, $\frac{Nv_{l,mk}}{2\pi}$ will not be integer which will lead to channel power leakage from the ($\lfloor \frac{Nv_{l,mk}}{2\pi} \rfloor$)th element to its nearby elements. In fact, the leakage of channel power is proportional to the deviation $\frac{Nv_{l,mk}}{2\pi} - \lfloor \frac{Nv_{l,mk}}{2\pi} \rfloor$, but is inversely proportional to N as shown in (7.14).

However, $[\mathbf{h}_{mk}^{\text{DFT}}]$ can still be approximated as a sparse vector with most power concentrated around the ($\lfloor \frac{Nv_{l,mk}}{2\pi} \rfloor$)th element [113, 115]. Hence, it is still useful to extract initial AoA information from the peak power position of $[\mathbf{h}_{mk}^{\text{DFT}}]$.

Moreover, we can express the DFT of the estimated channel matrix $\hat{\mathbf{h}}_{mk}$ with its q th element

$$[\hat{\mathbf{h}}_{mk}^{\text{DFT}}]_q = [\mathbf{h}_{mk}^{\text{DFT}}]_q + [\mathbf{n}_{mk}^{\text{DFT}}]_q. \tag{7.15}$$

We denote L largest peaks in L bins of $[\mathbf{h}_k^{\text{DFT}}]$ as $(q_1^{\text{ini}}, \dots, q_L^{\text{ini}})$. Then the

initial AoA estimates for the k th user can be calculated from

$$\hat{\phi}_{l,mk}^{\text{ini}} = \sin^{-1} \left(\frac{\lambda q_l^{\text{ini}}}{Nd} \right). \quad (7.16)$$

2. **Fine-Grain Estimation:** The resolution of $(\hat{\phi}_{l,mk}^{\text{ini}})$ via directly applying DFT is still limited by half of the DFT interval, i.e., $(\frac{1}{2N})$. To improve the AoA estimation accuracy, an angle rotation operation from [113, 115] is applied; however applying the estimation technique from [113, 115] is not applicable as is, since we need to further consider and estimate large scale fading coefficients, and apply the extended estimation technique on the proposed FDD-based cell-free massive MIMO system. The angle rotation of the original channel matrix is defined as

$$\mathbf{h}_{l,mk}^{\text{f}} = \mathbf{\Phi}_N(\Delta\phi_{l,mk})\mathbf{h}_{mk}, \quad (7.17)$$

where the diagonal matrix $\mathbf{\Phi}_N(\Delta\phi_{l,mk})$ is given by

$$\mathbf{\Phi}(\Delta\phi_{l,mk}) = \text{diag} \{ [1, e^{j\Delta\phi_{l,mk}}, \dots, e^{j(N-1)\Delta\phi_{l,mk}}] \}, \quad (7.18)$$

with $\Delta\phi_l \in [-(\pi/N), \pi/N]$ is the angle rotation parameter with search grid defined as G . After angle rotation, the DFT of the rotated channel model is given by

$$\begin{aligned} & [\mathbf{h}_{mk}^{\text{rDFT}}]_q \\ &= \frac{1}{\sqrt{NL}} \sum_{l=0}^{L-1} \sqrt{\beta_{l,mk}} \alpha_{l,mk} e^{-j\frac{N-1}{2} [\frac{2\pi}{N}q - \nu_{l,mk} - \Delta\phi_{l,mk}]} \cdot \frac{\sin \left[\left(\frac{2\pi}{N}q - \nu_{l,mk} - \Delta\phi_{l,mk} \right) \frac{N}{2} \right]}{\sin \left[\left(\frac{2\pi}{N}q - \nu_{l,mk} - \Delta\phi_{l,mk} \right) \frac{1}{2} \right]}. \end{aligned} \quad (7.19)$$

It can be deduced that the entries of $[\mathbf{h}_{mk}^{\text{rDFIT}}]$ have only L non-zero elements when the angle shifter satisfies

$$\Delta\phi_{l,mk} = 2\pi q_l/N - v_{l,mk} = 2\pi q_l/N - \eta \sin(\phi_{l,mk}), \quad (7.20)$$

where $\Delta\phi_{l,mk}$ is the optimal phase shifter. Based on the derived phased shifter, the estimated AoA of the l th path for the k th user is given by

$$\hat{\phi}_{l,mk} = \sin^{-1} \left(\frac{2\pi q_l}{N\eta} - \frac{\Delta\phi_{l,mk}}{\eta} \right). \quad (7.21)$$

Therefore, the estimated AoA matrix is given by

$$\hat{\mathbf{A}}_{mk} = [\mathbf{a}(\hat{\phi}_{1,mk}), \dots, \mathbf{a}(\hat{\phi}_{L,mk})]. \quad (7.22)$$

7.2.2 Large Scale Fading Estimation

Based on the AoA estimate and given that $\bar{\mathbf{n}}_{mk} \sim \mathcal{CN}(\mathbf{0}_{N \times 1}, \sigma_n^2 \mathbf{I}_N)$ in (7.9), the probability density function of $\bar{\mathbf{Y}}_{mk}$ for given $\phi_{l,mk}$ and $\beta_{l,mk}$ over all $l=1, \dots, L$ can be expressed as

$$f(\bar{\mathbf{Y}}_{mk} | \phi_{l,mk}, \beta_{l,mk}) = \frac{\exp \left\{ -\frac{1}{\sigma_n^2} \|\bar{\mathbf{Y}}_{mk} - \sqrt{\rho} \mathbf{A}_{mk} \mathbf{D}_{mk}\|_{\mathbb{F}}^2 \right\}}{(\pi \sigma_n^2)^N}. \quad (7.23)$$

The log-likelihood function can be applied to (7.23) to give

$$\mathcal{L}(\mathbf{D}_{mk}, \sigma_n^2) = -N \ln \pi - N \ln \sigma_n^2 - \frac{\|\bar{\mathbf{Y}}_{mk} - \sqrt{\rho} \mathbf{A}_{mk} \mathbf{D}_{mk}\|_{\mathbb{F}}^2}{\sigma_n^2}. \quad (7.24)$$

Knowing that \mathcal{L} is a concave function of σ_n^2 and \mathbf{D}_{mk} , the optimal estimates $\hat{\sigma}_n^2$

Algorithm 4 Extended DFT and angle rotation based multipath component estimation

- 1: **Input:** $\bar{\mathbf{Y}} \in \mathbb{C}^{N \times T}$, L , G and λ
 - 2: **Output:** $\hat{\boldsymbol{\phi}} \in \mathbb{R}^{L \times 1}$, $\hat{\boldsymbol{\beta}} \in \mathbb{C}^{L \times 1}$
 - 3: // AoA Estimation
 - 4: **for** $l = 1 : L$ **do**
 - 5: **for** $t = 1 : T$ **do**
 - 6: Find the central point (q_l^{ini}) of each bin in $\hat{\mathbf{h}}_{mk}^{\text{DFT}} = \mathbf{F}_N \bar{\mathbf{y}}_{mk}^{\text{p}}(t)$ where
 $(q_l^{\text{ini}}) = \arg \max_{(q) \in \text{bin}(l)} \|[\hat{\mathbf{h}}_{mk}^{\text{DFT}}]_q\|^2$, $l = 1, \dots, L$.
 - 7: $(\Delta \hat{\phi}_l) = \arg \max_{\Delta \phi \in [-\frac{\pi}{N}, \frac{\pi}{N}]} \|\mathbf{f}_{Nq_l^{\text{ini}}} \boldsymbol{\Phi}(\Delta \phi) \bar{\mathbf{y}}_{mk}^{\text{p}}(t)\|^2$, where $\mathbf{f}_{Nq_l^{\text{ini}}}$ is the
 q_l^{ini} th column of \mathbf{F}_N .
 - 8: $\hat{\theta}_l(t) = \hat{\theta}_l(t-1) + \sin^{-1} \left(\frac{2\pi q_l^{\text{ini}}}{N\eta} - \frac{\Delta \hat{\phi}_l}{\eta} \right)$
 - 9: **end**
 - 10: $\hat{\phi}_{l,mk} = \frac{1}{T} \hat{\theta}_l(T)$
 - 11: **end**
 - 12: // Large scale fading Estimation
 - 13: $\hat{\mathbf{D}}_{mk} = \frac{1}{\sqrt{\rho}} \left(\hat{\mathbf{A}}_{mk}^{\text{H}} \hat{\mathbf{A}}_{mk} \right)^{-1} \hat{\mathbf{A}}_{mk}^{\text{H}} \bar{\mathbf{Y}}_{mk}$
where $\hat{\mathbf{A}}_{mk} = [\mathbf{a}(\hat{\phi}_{1,mk}), \dots, \mathbf{a}(\hat{\phi}_{L,mk})]$
 - 14: $\hat{\mathbf{R}}_d = \frac{L}{T} [\hat{\mathbf{D}}_{mk} \hat{\mathbf{D}}_{mk}^{\text{H}}]$
 - 15: $\hat{\boldsymbol{\beta}}_{mk} = [\hat{\beta}_{1,mk}, \dots, \hat{\beta}_{L,mk}]^{\text{T}} = \text{diag}(\hat{\mathbf{R}}_d)$
 - 16: **end**
-

and $\hat{\mathbf{D}}_{mk}$ can be obtained by taking a partial derivative with respect to σ_n^2 and \mathbf{D}_{mk} . Hence, $\hat{\sigma}_n^2 = \frac{1}{N} \|\bar{\mathbf{Y}}_{mk} - \sqrt{\rho} \hat{\mathbf{A}}_{mk} \hat{\mathbf{D}}_{mk}\|_{\mathbb{F}}^2$, and

$$\begin{aligned}\hat{\mathbf{D}}_{mk} &= \frac{1}{\sqrt{\rho}} \left(\hat{\mathbf{A}}_{mk}^{\text{H}} \hat{\mathbf{A}}_{mk} \right)^{-1} \hat{\mathbf{A}}_{mk}^{\text{H}} \bar{\mathbf{Y}}_{mk} \\ &= \frac{1}{\sqrt{\rho}} \hat{\mathbf{A}}_{mk}^{\dagger} \bar{\mathbf{Y}}_{mk},\end{aligned}\tag{7.25}$$

where $\hat{\mathbf{A}}_{mk} = [\mathbf{a}(\hat{\phi}_{1,mk}), \dots, \mathbf{a}(\hat{\phi}_{L,mk})]$ is the estimate of \mathbf{A}_{mk} which is obtained using array signal processing (DFT operation with angle rotation). Once $\hat{\mathbf{A}}_{mk}$ is obtained, we next estimate the large-scale fading coefficients $\beta_{l,mk}$. From (7.25), we can estimate \mathbf{D}_{mk} and the covariance matrix $\hat{\mathbf{R}}_{mk,d} = \frac{L}{T} \mathbb{E}[\hat{\mathbf{D}}_{mk} \hat{\mathbf{D}}_{mk}^{\text{H}}]$. Note that the original covariance matrix $\mathbf{R}_{mk,d}$ is given by

$$\begin{aligned}\mathbf{R}_{mk,d} &= L \times \mathbb{E}[\mathbf{d}_{mk} \mathbf{d}_{mk}^{\text{H}}] = \mathbf{B}_{mk} \mathbb{E}[\boldsymbol{\alpha}_{mk} \boldsymbol{\alpha}_{mk}^{\text{H}}] \mathbf{B}_{mk}^{\text{H}} \\ &= \text{diag}(\beta_{1,mk}, \dots, \beta_{L,mk}).\end{aligned}\tag{7.26}$$

Hence, we can obtain the estimates of the large-scale fading coefficients as

$$\hat{\boldsymbol{\beta}}_{mk} = [\hat{\beta}_{1,mk}, \dots, \hat{\beta}_{L,mk}]^T = \text{diag}(\hat{\mathbf{R}}_{mk,d}).\tag{7.27}$$

The proposed multipath component estimation is shown in Algorithm 4, where \mathcal{G} is the search grid within $[-\frac{\pi}{N}, \frac{\pi}{N}]$ needed for angle estimation.

Note that the search grid parameter \mathcal{G} determines the complexity and accuracy of the algorithm. The complexity of the whole algorithm is of the order $O(N \log N + \mathcal{G}NL)$ where the factor $N \log N$ comes from the DFT operation and $\mathcal{G}NL$ comes from rotation operation over a search grid \mathcal{G} for all paths L over N antennas. Moreover, the complexity of the proposed algorithm is less than that of the

classical subspace ESPRIT algorithm of complexity $O(N^3 + UN^2)$, with $U \gg \mathcal{G}$ being the number of snapshots required during blind estimation [139].

7.2.3 Performance Analysis

Using the same methodology as in [113, 115] in addition to estimating the large-scale fading parameter, we derive the theoretical MSE of the AoA estimates and the large-scale fading coefficients for the cell-free massive MIMO system. In general, a closed-form solution of the MSE for multiple AoA estimations is hard to obtain [113]. An alternative approach is to consider the single user and single propagation path and derive corresponding MSE of ϕ and β as benchmark [113]. For a single propagation path according to (7.9), the received training signal at the m th AP transmitted by the k th user is given by

$$\begin{aligned}
\bar{\mathbf{y}}_{mk} &= \mathbf{Y}_{mk} \mathbf{p}_k^H \\
&= \sqrt{\rho} \mathbf{h}_{mk} + \bar{\mathbf{n}}_{mk} \\
&= \sqrt{\rho} \mathbf{a}(\phi) d_{mk} + \bar{\mathbf{n}}_{mk} \\
&= \sqrt{\rho} \sqrt{\beta_{mk} \alpha_{mk}} \mathbf{a}(\phi) + \bar{\mathbf{n}}_{mk}, \tag{7.28}
\end{aligned}$$

where $\mathbf{a}(\phi)$ is the $N \times 1$ steering vector with its q th entry given by $[\mathbf{a}(\phi)]_q = \frac{1}{\sqrt{N}} e^{(q-1)v_{mk}}$.

For brevity, we henceforth omit the subscript mk representing the link between the m th AP and the k th user. The proposed angle estimator can be expressed as

$$\begin{aligned}
\hat{v} &= \arg \max_v \left\| \frac{1}{\|\mathbf{a}(\phi)\|^2} \mathbf{a}(\phi)^H \bar{\mathbf{y}} \right\|^2 \\
&= \arg \max_v \left\| \mathbf{a}(\phi)^H \bar{\mathbf{y}} \right\|^2
\end{aligned}$$

$$= \arg \max_v \bar{\mathbf{y}}^H \mathbf{a}(\phi) \mathbf{a}(\phi)^H \bar{\mathbf{y}}, \quad (7.29)$$

where $\mathbf{a}(\phi) = \mathbf{\Phi}(\Delta\phi) \mathbf{f}_{N_q}$, $\|\mathbf{a}(\phi)\|^2 = 1$, \mathbf{f}_{N_q} is the q th column of \mathbf{F}_N , and q is the nearest integer to $\frac{Nv}{2\pi}$.

Moreover, using (7.25), the ML estimate of d is obtained as

$$\begin{aligned} \hat{d}_{\text{ML}} &= \frac{1}{\sqrt{\rho}} (\mathbf{a}(\hat{\phi})^H \mathbf{a}(\hat{\phi}))^{-1} \mathbf{a}(\hat{\phi})^H \bar{\mathbf{y}} \\ &= \frac{1}{\sqrt{\rho} \|\mathbf{a}(\hat{\phi})\|^2} \mathbf{a}(\hat{\phi})^H \bar{\mathbf{y}} \\ &= \frac{1}{\sqrt{\rho} \|\mathbf{a}(\hat{\phi})\|^2} \mathbf{a}(\hat{\phi})^H \mathbf{a}(\phi) d + \frac{1}{\sqrt{\rho} \|\mathbf{a}(\hat{\phi})\|^2} \mathbf{a}(\hat{\phi})^H \bar{\mathbf{n}} \\ &= \frac{1}{\sqrt{\rho} \|\mathbf{a}(\hat{\phi})\|^2} \mathbf{a}(\hat{\phi})^H \mathbf{a}(\phi) \sqrt{\beta} \alpha + \frac{1}{\sqrt{\rho} \|\mathbf{a}(\hat{\phi})\|^2} \mathbf{a}(\hat{\phi})^H \bar{\mathbf{n}}. \end{aligned} \quad (7.30)$$

The joint ML estimates of v and d can be obtained from

$$[\hat{v}_{\text{ML}} \hat{d}_{\text{ML}}] = \arg \min_{v,d} \|\bar{\mathbf{y}} - \mathbf{a}(\phi) d\|^2, \quad (7.31)$$

where $\hat{v}_{\text{ML}}, \hat{d}_{\text{ML}}$ are the optimizing variables.

Therefore, using (7.30), the ML estimate of v is given by

$$\hat{v}_{\text{ML}} = \arg \max_v \bar{\mathbf{y}}^H \mathbf{P}_{\mathbf{a}} \bar{\mathbf{y}} = \arg \max_v g(v), \quad (7.32)$$

where $g(v)$ is the cost function of v . For the single-path case, $\mathbf{P}_{\mathbf{a}} = \mathbf{a}(\phi) \mathbf{a}(\phi)^H$ is the projection matrix onto the subspace spanned by $\mathbf{a}(\phi)$, and $\mathbf{a}(\phi)$ represents the steering vector given in (7.1). For the multi-path case, $\mathbf{P}_{\mathbf{A}} = \mathbf{A} \mathbf{A}^\dagger = \mathbf{A} (\mathbf{A}^H \mathbf{A})^{-1} \mathbf{A}^H$ represents the projection matrix onto the subspace spanned by \mathbf{A} , and \mathbf{A} is the steering matrix given in (7.4). As shown in [115] while including the large scale path-loss parameter β , the MSE (7.29) of the considered DFT estimator coincides

with that of the ML estimator (7.31). Using Lemma 1 in [115] while including the large-scale fading parameter and $\mathbf{p}_k \mathbf{p}_k^H = 1$, the MSE of v is expressed as

$$\mathbb{E}[\Delta v^2] = \mathbb{E}[(\hat{v} - v)(\hat{v} - v)^H] = \frac{\sigma_n^2}{2\rho\beta\mathbf{a}(\hat{\phi})^H \mathbf{E} \mathbf{P}_a^\perp \mathbf{E} \mathbf{a}(\hat{\phi})}, \quad (7.33)$$

where $\mathbb{E}[\Delta v] = 0$, $\mathbf{P}_a^\perp = \mathbf{I} - \mathbf{P}_a$ is the projection matrix onto the orthogonal space spanned by $\mathbf{a}(\phi)$ and \mathbf{E} is the diagonal matrix given by $\mathbf{E} = \text{diag}\{0, \dots, (N-1)\}$. Based on the fact that $v = \eta \sin \phi$ and $\phi = \sin^{-1}(\frac{v}{\eta})$, we further examine the MSE of ϕ

$$\mathbb{E}[\Delta \phi^2] = \frac{(\frac{1}{\eta})^2}{1 - (\frac{v}{\eta})^2} \times \frac{\sigma_n^2}{2\beta\mathbf{a}(\hat{\phi})^H \mathbf{E} \mathbf{P}_a^\perp \mathbf{E} \mathbf{a}(\hat{\phi})}. \quad (7.34)$$

Using Taylor series expansion, a first-order approximation of $\mathbf{a}(\phi)$ is given by

$$\mathbf{a}(\phi) = \mathbf{a}(\hat{\phi}) + j\mathbf{E}\mathbf{a}(\hat{\phi})\Delta v. \quad (7.35)$$

Substituting (7.35) into (7.30) and after collecting T samples, we rewrite $\hat{\mathbf{d}}$ as

$$\begin{aligned} \hat{\mathbf{d}} &= [\hat{d}_1, \dots, \hat{d}_T] \\ &= \mathbf{d} + j\frac{1}{\|\mathbf{a}(\hat{\phi})\|^2} \mathbf{a}(\hat{\phi})^H \mathbf{E} \mathbf{a}(\hat{\phi}) \Delta v \mathbf{d} + \frac{1}{\sqrt{\rho}\|\mathbf{a}(\hat{\phi})\|^2} \mathbf{a}(\hat{\phi})^H \bar{\mathbf{N}}, \end{aligned} \quad (7.36)$$

where $\bar{\mathbf{N}} = [\bar{\mathbf{n}}_1, \dots, \bar{\mathbf{n}}_T]$.

Moreover,

$$\begin{aligned} \hat{\beta} &= \frac{L}{T} \mathbb{E}[\hat{\mathbf{d}}\hat{\mathbf{d}}^H] = \beta + \beta \mathbb{E}[(\Delta v)^2] \left| \frac{1}{\|\mathbf{a}(\hat{\phi})\|^2} \mathbf{a}(\hat{\phi})^H \mathbf{E} \mathbf{a}(\hat{\phi}) \right|^2 + \\ &\quad \frac{1}{\sqrt{\rho}\|\mathbf{a}(\hat{\phi})\|^2} \mathbf{a}(\hat{\phi})^H \mathbb{E}[\mathbf{nn}^H] \left(\frac{1}{\sqrt{\rho}\|\mathbf{a}(\hat{\phi})\|^2} \mathbf{a}(\hat{\phi})^H \right)^H \\ &= \beta + \frac{\sigma_n^2 |\mathbf{a}(\hat{\phi})^H \mathbf{E} \mathbf{a}(\hat{\phi})|^2}{2\rho\mathbf{a}(\hat{\phi})^H \mathbf{E} \mathbf{P}_a^\perp \mathbf{E} \mathbf{a}(\hat{\phi})} + \frac{\sigma_n^2}{\rho}. \end{aligned} \quad (7.37)$$

Therefore, the MSE of β can be obtained

$$\begin{aligned}\mathbb{E}[\Delta\beta^2] &= \mathbb{E}\left[(\hat{\beta} - \beta)(\hat{\beta} - \beta)^{\text{H}}\right] \\ &= \left(\frac{\sigma_n^2 |\mathbf{a}(\hat{\phi})^{\text{H}} \mathbf{E} \mathbf{a}(\hat{\phi})|^2}{2\rho \mathbf{a}(\hat{\phi})^{\text{H}} \mathbf{E} \mathbf{P}_{\mathbf{a}}^{\perp} \mathbf{E} \mathbf{a}(\hat{\phi})} + \frac{\sigma_n^2}{\rho}\right)^2.\end{aligned}\quad (7.38)$$

Furthermore, the MSE expressions of the estimated AoA and large-scale fading components derived in (7.33) and (7.38) give important insights when assessing the impact of beamforming/combining techniques on the spectral efficiency of the proposed FDD-based cell-free massive MIMO system.

7.2.4 Angle Coherence Time

Different from the conventional channel coherence time, the angle coherence time is defined as typically an order of magnitude longer, during which the AoDs can be regarded as static [43]. Specifically, the path AoD in (7.1) mainly depends on the surrounding obstacles around the BS, which may not physically change their positions often. On the contrary, the path gain of the k th user depends on a number of unresolvable paths, each of which is generated by a scatter surrounding the user. Therefore, path gains vary much faster than the path AoDs [43]. Accordingly, the angle coherence time is much longer than the conventional channel coherence time. Therefore, we can leverage from this fact and perform multipath estimation in every angle coherence time instead of the much shorter channel coherence time as the impact of the overhead is substantially reduced.

7.3 Proposed Beamforming and Combining Techniques

We next propose the angle-based matched-filtering, angle-based zero-forcing and angle-based minimum-mean-square-error beamforming/combining that incorporate the estimated angle information, and the large-scale fading components.

The APs are connected via a backhaul network to a CPU, which sends to the APs the data-symbols to be transmitted to the end-users and receives soft-estimates of the received data-symbols from all the APs. Neither multipath estimates nor beamforming/combining vectors are transmitted through the backhaul network.

7.3.1 Angle-Based Beamforming

The angle-based beamforming (or precoding) vector $\hat{\mathbf{w}}_{mk}$ for the m th AP and the k th user is defined as

$$\hat{\mathbf{w}}_{mk} = \sum_{l=1}^L \gamma_{mk,l} \hat{\mathbf{g}}_{mk,l} = \frac{\hat{\mathbf{G}}_{mk}}{\|\hat{\mathbf{G}}_{mk}\|} \boldsymbol{\gamma}_{mk}, \quad (7.39)$$

where $\hat{\mathbf{g}}_{mk,l}$ is the l th column of $\hat{\mathbf{G}}_{mk} = [\hat{\mathbf{g}}_{mk,1}, \dots, \hat{\mathbf{g}}_{mk,L}]$ defined below for the proposed angle-based beamforming techniques. In addition, $\gamma_{mk,l}$ is the normalized complex weight for the l th propagation path that satisfies $\sum_{l=1}^L |\gamma_{mk,l}|^2 = 1$ and $\boldsymbol{\gamma}_{mk} = [\gamma_{mk,1}, \dots, \gamma_{mk,L}]^T$. Moreover, using (7.10),

$$\mathbb{E}[\|\mathbf{x}_m\|^2] = \rho_d \sum_{k=1}^K \frac{\|\hat{\mathbf{G}}_{mk} \boldsymbol{\gamma}_{mk}\|^2}{\|\hat{\mathbf{G}}_{mk}\|^2} \leq \rho_d \quad (7.40)$$

will satisfy the maximum transmit power ρ_d .

Angle-Based Matched-Filtering Beamforming (A-MF)

The precoder matrix based on the angle information is given by

$$\hat{\mathbf{G}}_{mk}^{\text{A-MF}} = \hat{\mathbf{A}}_{mk} \hat{\mathbf{B}}_{mk}, \quad (7.41)$$

where $\hat{\mathbf{A}}_{mk} = [\mathbf{a}(\hat{\phi}_{1,mk}), \dots, \mathbf{a}(\hat{\phi}_{L,mk})]$ and $\hat{\mathbf{B}}_{mk} = \text{diag}(\sqrt{\hat{\beta}_{1,mk}}, \dots, \sqrt{\hat{\beta}_{L,mk}})$ are the estimated AoA and large-scale fading matrices according to (7.22) and (7.27). Moreover, A-MF is a simple beamforming approach that only requires the channel multipath components (AoA and large-scale fading) of the direct link between the m th AP and the k th user. However, the inter user interference is ignored.

Angle-Based Zero-Forcing Beamforming (A-ZF)

We use A-ZF beamforming as a means to efficiently suppress interference. To do so, the conventional ZF beamforming employs all the downlink CSI from the users. However, the angle-based ZF beamforming used in this work is distinct from the conventional ZF beamforming in the sense that only the angle information and large-scale fading coefficients of the channel are required in the beamforming design. We collect the corresponding array steering vectors into $\hat{\mathbf{A}}_m = [\hat{\mathbf{A}}_{m1}, \dots, \hat{\mathbf{A}}_{mK}]$ and similarly for $\hat{\mathbf{B}}_m = \text{diag}([\hat{\mathbf{B}}_{m1}, \dots, \hat{\mathbf{B}}_{mK}]^T)$. Then, the precoder matrix is given by

$$\hat{\mathbf{G}}_m^{\text{A-ZF}} = \hat{\mathbf{A}}_m \hat{\mathbf{B}}_m \left(\hat{\mathbf{B}}_m^H \hat{\mathbf{A}}_m^H \hat{\mathbf{A}}_m \hat{\mathbf{B}}_m \right)^{-1}, \quad (7.42)$$

where beamforming vector is $\hat{\mathbf{g}}_{mk,l}$ defined as the $((k-1)L+l)$ th column of $\hat{\mathbf{G}}_m^{\text{A-ZF}}$.

A key property of the angle-based ZF beamforming is that the beamforming

vector is orthogonal to all other array steering vectors as given below:

$$\hat{\mathbf{h}}_{mk}^H \hat{\mathbf{w}}_{mi}^{\text{A-ZF}} = \begin{cases} \mathbf{s}_{mk}^T \gamma_{mk} & \text{if } i = k; \\ 0 & \text{if } i \neq k. \end{cases} \quad (7.43)$$

The pseudo-inverse in A-ZF is more complex than A-MF, but the interference is suppressed.

Angle-Based MMSE Beamforming (A-MMSE)

We use an angle-based MMSE beamforming design that can efficiently suppress interference, noise and channel estimation error. The A-MMSE strikes a balance between attaining the best signal amplification and reducing the interference. The proposed angle-based MMSE beamforming matrix is given by

$$\mathbf{G}_{mk}^{\text{A-MMSE}} = \left(\sum_{k=1}^K ((\hat{\mathbf{A}}_{mk} \hat{\mathbf{B}}_{mk} \hat{\mathbf{B}}_{mk}^H \hat{\mathbf{A}}_{mk}^H + \Upsilon_{m,k}) + \sigma_n^2 \mathbf{I}_N) \right)^{-1} \hat{\mathbf{A}}_{mk} \hat{\mathbf{B}}_{mk}, \quad (7.44)$$

where $\Upsilon_{m,k} = \tilde{\sigma}_v^2 (\mathbf{E} \hat{\mathbf{A}}_{mk} \hat{\mathbf{B}}_{mk}) (\mathbf{E} \hat{\mathbf{A}}_{mk} \hat{\mathbf{B}}_{mk})^H + \tilde{\sigma}_v^2 \tilde{\sigma}_\beta^2 (\mathbf{E} \hat{\mathbf{A}}_{mk}) (\mathbf{E} \hat{\mathbf{A}}_{mk})^H + \tilde{\sigma}_\beta^2 \hat{\mathbf{A}}_{mk} \hat{\mathbf{A}}_{mk}^H$,

such that $\tilde{\sigma}_v^2 = \sigma_v^2 + \mathbb{E}[\Delta v^2]$ and $\tilde{\sigma}_\beta^2 = \sigma_\beta^2 + \mathbb{E}[\Delta \beta^2]$, where σ_v^2 and σ_β^2 account for non-ideal DL angle reciprocity, and $\mathbb{E}[\Delta v^2]$, $\mathbb{E}[\Delta \beta^2]$ are the MSEs as defined in (7.33) and (7.38), respectively.

Therefore, for A-ZF/A-MMSE, the only overhead for DL channel acquisition at each AP comes from UL training, which only scales with the number of served users. In addition, one can note that A-ZF is suitable for high signal-to-noise ratio (SNR) conditions since it is expected that A-ZF and A-MMSE would have

the same performance when the effect of noise is low.

7.3.2 Angle-Based Combining

Similarly, the combining vector $\hat{\mathbf{v}}_{mk}$ for the m th AP and the k th user is defined as

$$\hat{\mathbf{v}}_{mk} = \sum_{l=1}^L \gamma_{mk,l} \hat{\mathbf{c}}_{mk,l} = \hat{\mathbf{C}}_{mk} \boldsymbol{\gamma}_{mk}, \quad (7.45)$$

where $\hat{\mathbf{c}}_{mk,l}$ is the $((k-1)L+l)$ th column of $\hat{\mathbf{C}}_m$ which corresponds to $\hat{\mathbf{C}}_{mk} = [\hat{\mathbf{c}}_{mk,1}, \dots, \hat{\mathbf{c}}_{mk,L}]$, and $\gamma_{mk,l} = \frac{1}{L}$ and $\boldsymbol{\gamma}_{mk} = [\gamma_{mk,1}, \dots, \gamma_{mk,L}]^T$.

Using UL-DL duality [140], the combining vectors of the uplink case for A-MF combining, A-ZF combining and A-MMSE combining are also defined as

$$\hat{\mathbf{C}}_{mk} = \begin{cases} \mathbf{G}_{mk}^{\text{A-MF}} & \text{for A-MF combining;} \\ \mathbf{G}_{mk}^{\text{A-ZF}} & \text{for A-ZF combining;} \\ \mathbf{G}_{mk}^{\text{A-MMSE}} & \text{for A-MMSE combining.} \end{cases} \quad (7.46)$$

such that $\tilde{\sigma}_v^2 = \mathbb{E}[\Delta v^2]$ and $\tilde{\sigma}_\beta^2 = \mathbb{E}[\Delta \beta^2]$. The corresponding combining matrices were defined in (7.41), (7.42) and (7.44).

The benefits of relying on only the angle information and large-scale fading are: (i) the need for downlink training is avoided; (ii) the beamforming/combining matrices can be updated every angle coherence time, and (iii) a simple closed-form expression for the spectral efficiency can be derived which enables us to obtain important insights.

Chapter 8

Power Control and AP selection For FDD-based Cell Free Massive MIMO

In this chapter, closed-form expressions are derived for the spectral efficiencies for the FDD-based cell-free massive MIMO downlink and uplink with finite numbers of APs and users.

Our analysis takes into account the proposed beamforming/combining techniques and the effect of multipath estimation errors. Finally, we propose a solution to the max-min power control problem by formulating it as a standard semi-definite programming (SDP) approach. The proposed max-min power control maximizes the smallest rate of all users within the angle-coherence time-scale. In addition, we present a user-centric AP selection scheme to further enhance the energy efficiency of the system.

Simulation results are presented to demonstrate the effectiveness of the proposed schemes. The corresponding results have been published in parts in [50, 51].

8.1 Spectral and Energy efficiency Analysis

In this section, we derive closed-form expressions for the spectral efficiencies per user for DL and UL transmissions using the analysis technique from [32, 33, 116]. Then, we define the total energy efficiency of the system.

8.1.1 Spectral Efficiency

The downlink spectral efficiency per user using the proposed beamforming schemes is given by

$$R_k^d = \log_2 (1 + \text{SINR}_k^d) \simeq \log_2 \left(1 + \frac{\rho^d S_k^d}{\rho^d I_{jk}^d + \rho^d BU_k^d + \sigma_n^2} \right), \quad (8.1)$$

where

$$\begin{aligned} S_k^d &= \sum_{m=1}^M \mathbb{E} \left[\|\hat{\mathbf{h}}_{mk}^H \hat{\mathbf{w}}_{mk}\|^2 \right], \\ I_{jk}^d &= \sum_{j \neq k}^K \sum_{m=1}^M \mathbb{E} \left[\|\hat{\mathbf{h}}_{mk}^H \hat{\mathbf{w}}_{mj}\|^2 \right], \text{ and} \\ BU_k^d &= \sum_{j=1}^K \sum_{m=1}^M \mathbb{E} \left[\|\tilde{\mathbf{h}}_{mk}^H \hat{\mathbf{w}}_{mj}\|^2 \right], \end{aligned}$$

represent the strength of the desired signal of the k th user (S_k^d), the interference generated by the j th user (I_{jk}^d), and the beamforming gain uncertainty (BU_k^d), respectively. The elements inside the norm of S_k^d , I_{jk}^d and BU_k^d are uncorrelated zero mean random variables. In addition, $\hat{\mathbf{h}}_{mk} = \mathbf{h}_{mk} - \tilde{\mathbf{h}}_{mk} = \hat{\mathbf{A}}_{mk} \hat{\mathbf{B}}_{mk} \mathbf{s}_{mk}$ and the channel uncertainty is $\tilde{\mathbf{h}}_{mk} = \Delta \tilde{v} (\mathbf{E} \hat{\mathbf{A}}_{mk} \hat{\mathbf{B}}_{mk}) \mathbf{s}_{mk} + \Delta \tilde{\beta} \hat{\mathbf{A}}_{mk} \mathbf{s}_{mk} + \Delta \tilde{\beta} \Delta \tilde{v} \mathbf{E} \hat{\mathbf{A}}_{mk} \mathbf{s}_{mk}$, where $\Delta \tilde{v}$ and $\Delta \tilde{\beta}$ differ in the DL and UL directions due to un-ideal angle reciprocity such that $\Delta \tilde{v}^d = v^u - \hat{v}^u - \tilde{v}^{u/d}$, $\Delta \tilde{\beta}^d = \beta^u - \hat{\beta}^u - \tilde{\beta}^{u/d}$, $\Delta \tilde{v}^u = v^u - \hat{v}^u$,

$$R_k^d \simeq \log_2 \left(1 + \frac{\rho^d \sum_{m=1}^M \|\hat{\mathbf{B}}_{mk}^H \hat{\mathbf{A}}_{mk}^H \hat{\mathbf{w}}_{mk}\|^2}{\rho^d \sum_{j \neq k}^K \sum_{m=1}^M \|\hat{\mathbf{B}}_{mk}^H \hat{\mathbf{A}}_{mk}^H \hat{\mathbf{w}}_{mj}\|^2 + \rho^d \sum_{j=1}^K \sum_{m=1}^M \Omega_{m,j} + \sigma_n^2} \right), \quad (8.3)$$

where $\Omega_{m,j} = \tilde{\sigma}_v^2 \|(\hat{\mathbf{B}}_{mk}^H \hat{\mathbf{A}}_{mk}^H \mathbf{E}) \hat{\mathbf{w}}_{mj}\|^2 + \tilde{\sigma}_\beta^2 \|(\hat{\mathbf{A}}_{mk}^H \hat{\mathbf{w}}_{mj})\|^2 + \tilde{\sigma}_\beta^2 \tilde{\sigma}_v^2 \|(\hat{\mathbf{A}}_{mk}^H \mathbf{E} \hat{\mathbf{w}}_{mj})\|^2$.

$$R_k^u \simeq \log_2 \left(1 + \frac{\rho^u \sum_{m=1}^M \|\hat{\mathbf{B}}_{mk}^H \hat{\mathbf{A}}_{mk}^H \hat{\mathbf{v}}_{mk}\|^2}{\rho^u \sum_{j \neq k}^K \sum_{m=1}^M \|\hat{\mathbf{B}}_{mk}^H \hat{\mathbf{A}}_{mk}^H \hat{\mathbf{v}}_{mj}\|^2 + \rho^u \sum_{j=1}^K \sum_{m=1}^M \Lambda_{m,j} + \sigma_n^2 \sum_{m=1}^M \|\hat{\mathbf{v}}_{mk}\|^2} \right), \quad (8.4)$$

where $\Lambda_{m,j} = \tilde{\sigma}_v^2 \|(\hat{\mathbf{B}}_{mk}^H \hat{\mathbf{A}}_{mk}^H \mathbf{E}) \hat{\mathbf{v}}_{mj}\|^2 + \tilde{\sigma}_\beta^2 \|(\hat{\mathbf{A}}_{mk}^H \hat{\mathbf{v}}_{mj})\|^2 + \tilde{\sigma}_\beta^2 \tilde{\sigma}_v^2 \|(\hat{\mathbf{A}}_{mk}^H \mathbf{E} \hat{\mathbf{v}}_{mj})\|^2$.

and $\Delta \tilde{\beta}^u = \beta^u - \hat{\beta}^u$.

Similarly for the uplink case, the uplink spectral efficiency per user using the proposed combining schemes is given by

$$R_k^u \simeq \log_2 \left(1 + \frac{\rho^u S_k^u}{\rho^u I_{jk}^u + \rho^u BU_k^u + \sigma_n^2 \sum_{m=1}^M \|\hat{\mathbf{v}}_{mk}\|^2} \right), \quad (8.2)$$

where uplink desired signal power (S_k^u), the interference caused by the j th user (I_{jk}^u), and the combining gain uncertainty (BU_k^u) are defined similarly as the downlink case but by substituting $\hat{\mathbf{w}}_{mj}$ with the combining vector $\hat{\mathbf{v}}_{mj}$.

Using the fact that $\alpha_l \sim \mathcal{CN}(0, 1)$ as well as the fact that angle of arrival and the large-scale fading remain unchanged during the angle coherence time, we can further reduce the DL and UL spectral efficiencies into closed forms as shown in (8.3) and (8.4) at the top of the next page.

8.1.2 Energy Efficiency

The total energy efficiency (bit/Joule) is defined as the sum throughput (bit/s) divided by the total power consumption (Watt) in the network:

$$\text{EE} \triangleq \frac{B \cdot \sum_{k=1}^K \kappa R_k}{P_{\text{total}}}, \quad (8.5)$$

where R_k is the spectral efficiency (expressed in bit/s/Hz) for the k th user, B is defined as the system bandwidth, P_{total} is the total power consumption, $\kappa = \left(1 - \frac{\tau}{\tau_c}\right)$, and $\tau = K$ is length of pilot training sequence in samples, τ_c is the angle coherence interval in samples. Furthermore, we consider the power consumption model defined in [33]

$$P_{\text{total}} = \sum_{m=1}^M P_m + \sum_{m=1}^M P_{\text{bh},m}, \quad (8.6)$$

where P_m is the power consumed at the m th AP which includes the amplifier and the circuit power consumption and the power consumption of the transceiver chains and the power consumed for signal processing, and $P_{\text{bh},m}$ represents the power consumed by the backhaul link that transfers data between the CPU and the m th AP. The power consumption term P_m can be defined as

$$P_m = \frac{1}{\vartheta_m} \rho^{\text{d}} \sigma_n^2 \left(N \sum_{k=1}^K \|\hat{\mathbf{w}}_{mk}\|^2 \right) + N P_{\text{tc},m}, \quad (8.7)$$

where $0 < \vartheta_m \leq 1$ is the power amplifier efficiency, ρ^{d} is the downlink SNR, σ_n^2 is the noise power, $\hat{\mathbf{w}}_{mk}$ is the angle based beamforming vector for the m th AP and the k th user (defined in (7.39)), N is the number of antennas at the AP, and $P_{\text{tc},m}$ is the internal power required to operate the circuit components (e.g., converters, mixers, and filters) per antenna at the m th AP.

Moreover, the power consumption of the backhaul is proportional to the sum

spectral efficiency and can be modeled as,

$$P_{\text{bh},m} = P_{0,m} + B \cdot \sum_{k=1}^K \kappa R_k \cdot P_{\text{bt},m}, \quad (8.8)$$

where $P_{0,m}$ is defined as a fixed power consumption of each backhaul (traffic-independent power) which may depend on the distances between the APs and the CPU and the system topology, and $P_{\text{bt},m}$ is defined as the traffic-dependent power (in Watt per bit/s).

8.2 Proposed Max-Min Power control

To obtain good system performance, the available power resources must be efficiently managed. In this section, we propose a solution to the max-min user-fairness problem in the proposed cell-free Massive MIMO system, where the minimum rates of all users are maximized while satisfying a per-user power constraint. We show that the FDD-based cell-free massive MIMO system can provide uniformly good service to all users, regardless of their geographical location, by adopting a max-min power/weight control strategy. The proposed power control algorithm is done at the CPU, and importantly, is carried only at the *angle-coherence* time-scale. Hence the impact of the signaling overhead is substantially reduced. Moreover, we present a user centric AP selection approach to further enhance the energy efficiency of the CF massive MIMO system.

8.2.1 Downlink Power Control

In the downlink, given realizations of the large-scale fading and the array steering vectors, we find the power control coefficients γ_{mk} , $m = 1, \dots, M$, $k =$

$1, \dots, K$, that maximize the minimum of the downlink rates of all users, under the power constraint (7.40). At the optimum point, all users attain the same rate. Mathematically, this is formulated as:

$$\begin{aligned}
& \max_{\{\gamma_{mk,l}\}} \min_{k=1, \dots, K} R_k^d \\
& \text{subject to } \sum_{k=1}^K \frac{\|\hat{\mathbf{G}}_{mk} \gamma_{mk}\|^2}{\|\hat{\mathbf{G}}_{mk}\|^2} \leq 1, \quad m = 1, \dots, M \\
& \gamma_{mk,l} \geq 0, \quad \forall k, \forall m, \forall l.
\end{aligned} \tag{8.9}$$

Then, using (8.3), we can reformulate (8.9) into a max-min SINR problem as follows:

$$\begin{aligned}
& \max_{\{\gamma_{mk,l}\}} \min_{k=1, \dots, K} \\
& \frac{\rho^d \sum_{m=1}^M \|\hat{\mathbf{B}}_{mk}^H \hat{\mathbf{A}}_{mk}^H \hat{\mathbf{w}}_{mk}\|^2}{\rho^d \sum_{j \neq k}^K \sum_{m=1}^M \|\hat{\mathbf{B}}_{mj}^H \hat{\mathbf{A}}_{mj}^H \hat{\mathbf{w}}_{mj}\|^2 + \rho^d \sum_{j=1}^K \sum_{m=1}^M \Omega_{m,j} + \sigma_n^2} \\
& \text{s.t. } \sum_{k=1}^K \frac{\|\hat{\mathbf{G}}_{mk} \gamma_{mk}\|^2}{\|\hat{\mathbf{G}}_{mk}\|^2} \leq 1, \quad \forall m, \\
& \hat{\mathbf{w}}_{mk} = \frac{\hat{\mathbf{G}}_{mk}}{\|\hat{\mathbf{G}}_{mk}\|} \gamma_{mk}, \quad \forall k, \forall m, \text{ and} \\
& \gamma_{mk,l} \geq 0, \quad \forall k, \forall m, \forall l.
\end{aligned} \tag{8.10}$$

One can note that (8.10) is a non-convex separable quadratically-constrained quadratic program (QCQP) in terms of power allocation γ_{mk} , for all k, m . Therefore, this problem cannot be directly solved in an efficient manner using existing convex optimization schemes. While the non-convex QCQP is NP-hard, it can be relaxed into a convex semi-definite program (SDP) using semi-definite relaxation (SDR) [141], in which the following property of a scalar is utilized: $\gamma_{mk}^H \mathbf{Q} \gamma_{mk} = \text{tr}(\gamma_{mk}^H \mathbf{Q} \gamma_{mk}) = \text{tr}(\mathbf{Q} \gamma_{mk} \gamma_{mk}^H)$, for any $\mathbf{Q} \in \mathbb{C}^{L \times L}$. Therefore, by introducing

a new variable $\mathbf{\Gamma}_{mk} = \boldsymbol{\gamma}_{mk}\boldsymbol{\gamma}_{mk}^H$, which is a rank-one symmetric positive semi-definite (PSD) matrix, the quadratic constraints can be transformed into linear constraints in the set of all real symmetric $L \times L$ matrices \mathbb{S}^L . Using SDP, problem (8.10) can be equivalently reformulated as

$$\begin{aligned}
& \max_{\{\mathbf{\Gamma}_{mk}\}} \min_{k=1, \dots, K} \\
& \frac{\rho^d \sum_{m=1}^M \text{tr}(\boldsymbol{\Xi}_{mkk} \boldsymbol{\Xi}_{mkk}^H \mathbf{\Gamma}_{mk})}{\rho^d \sum_{j \neq k}^K \sum_{m=1}^M \text{tr}(\boldsymbol{\Xi}_{mkj} \boldsymbol{\Xi}_{mkj}^H \mathbf{\Gamma}_{mj}) + \rho^d \sum_{j=1}^K \sum_{m=1}^M \Omega_{m,j} + \sigma_n^2} \\
& \text{s.t.} \quad \sum_{k=1}^K \frac{\text{tr}(\hat{\mathbf{G}}_{mk}^H \hat{\mathbf{G}}_{mk} \mathbf{\Gamma}_{mk})}{\|\hat{\mathbf{G}}_{mk}\|^2} \leq 1, \quad \forall m, \\
& \mathbf{\Gamma}_{mk} \succeq 0, \quad \forall k, \quad \forall m, \\
& \text{rank}(\mathbf{\Gamma}_{mk}) = 1, \quad \forall k, \quad \forall m,
\end{aligned} \tag{8.11}$$

where $\boldsymbol{\Xi}_{mkj} = \hat{\mathbf{B}}_{mk}^H \hat{\mathbf{A}}_{mk}^H \frac{\hat{\mathbf{G}}_{mj}}{\|\hat{\mathbf{G}}_{mj}\|}$.

Since the rank constraint of $\mathbf{\Gamma}_{mk}$ is non-convex, we relax it to obtain the feasible SDP formulation of (8.11) as

$$\begin{aligned}
& \max_{\{\mathbf{\Gamma}_{mk}\}} \mu \\
& \text{s.t.} \\
& \frac{\rho^d \sum_{m=1}^M \text{tr}(\boldsymbol{\Xi}_{mkk} \boldsymbol{\Xi}_{mkk}^H \mathbf{\Gamma}_{mk})}{\rho^d \sum_{j \neq k}^K \sum_{m=1}^M \text{tr}(\boldsymbol{\Xi}_{mkj} \boldsymbol{\Xi}_{mkj}^H \mathbf{\Gamma}_{mj}) + \rho^d \sum_{j=1}^K \sum_{m=1}^M \Omega_{m,j} + \sigma_n^2} \geq \mu, \\
& \sum_{k=1}^K \frac{\text{tr}(\hat{\mathbf{G}}_{mk}^H \hat{\mathbf{G}}_{mk} \mathbf{\Gamma}_{mk})}{\|\hat{\mathbf{G}}_{mk}\|^2} \leq 1, \quad \forall m, \text{ and } \mathbf{\Gamma}_{mk} \succeq 0, \quad \forall k, \quad \forall m.
\end{aligned} \tag{8.12}$$

The relaxed problem (8.12) is a convex SDP and can be solved by standard convex optimization tools such as CVX [142]. Once the optimal variables $\hat{\mathbf{\Gamma}}_{mk}$ ($\forall m, \forall k$) are obtained, we can find the rank-one approximations of $\hat{\mathbf{\Gamma}}_{mk}$ which are feasible for the original problem (8.10) by applying eigen-value decomposition

Algorithm 5 SDR-based Bisection Algorithm for Solving (8.12)

- 1: **Initialization:** Define the initial values μ_{\max} , μ_{\min} that represent the range of relevant values of the objective function in (8.12), and Choose a tolerance $\epsilon > 0$
- 2: **Set:** $\mu = \frac{\mu_{\max} + \mu_{\min}}{2}$,
- 3: **Solve the following convex SDP feasibility program:**
- 4:

$$\left\{ \begin{array}{l} \rho^d \sum_{m=1}^M \text{tr}(\mathbf{\Xi}_{mkk} \mathbf{\Xi}_{mkk}^H \mathbf{\Gamma}_{mk}) \geq \\ \mu \left(\rho^d \sum_{j \neq k}^K \sum_{m=1}^M \text{tr}(\mathbf{\Xi}_{mkj} \mathbf{\Xi}_{mkj}^H \mathbf{\Gamma}_{mj}) + \rho^d \sum_{j=1}^K \sum_{m=1}^M \Omega_{m,j} + \sigma_n^2 \right), \forall k, \\ \sum_{k=1}^K \frac{\text{tr}(\hat{\mathbf{G}}_{mk}^H \hat{\mathbf{G}}_{mk} \mathbf{\Gamma}_{mk})}{\|\hat{\mathbf{G}}_{mk}\|^2} \leq 1, \forall m, \text{ and } \mathbf{\Gamma}_{mk} \succeq 0, \forall k, \forall m, \end{array} \right. \quad (8.13)$$

- 5: **if** problem (8.13) is feasible, **then**
 - 6: set $\mu_{\min} = \mu$
 - 7: **else** set $\mu_{\max} = \mu$.
 - 8: **end if**
 - 9: Stop **if** $\mu_{\max} - \mu_{\min} < \epsilon$. **Otherwise**, go to Step 2.
 - 10: $[\mathbf{U}_{mk}, \mathbf{V}_{mk}] = \text{EVD}(\mathbf{\Gamma}_{mk})$, $\forall k, \forall m$, where $\mathbf{V}_{L \times L}$ is the diagonal matrix of eigenvalues, and $\mathbf{U}_{L \times L}$ is a full matrix whose columns are the corresponding eigenvectors (\mathbf{u}).
 - 11: $\gamma_{mk} = \sqrt{\max(\mathbf{V}_{mk}) \mathbf{u}_{m,k}^{\max}}$, $\forall k, \forall m$, where \mathbf{u}^{\max} is the corresponding eigenvector to the maximum eigenvalue in \mathbf{V} .
 - 12: **end**
-

(EVD) on $\hat{\mathbf{\Gamma}}_{mk}$, and extracting the largest eigen-value and the corresponding eigen-vector to construct $\hat{\gamma}_{mk}$. Consequently, (8.12) can be solved efficiently via a bisection search, in which each step involves solving a sequence of convex SDP feasibility sub problems [143]. The proposed max-min power control algorithm is summarized in Algorithm 5.

Complexity Analysis: Here, we provide the computational complexity analysis for the proposed Algorithm 5, which uses iterative bisection search to solve the convex optimization problem (8.12) at each iteration. The complexity of (8.12) is $\mathcal{O}((MK)^4 L^{1/2})$ in each iteration [144]. Note that the total number of iterations to solve the SDR Problem via a bisection search method is given by $\log(\frac{\mu_{\max} - \mu_{\min}}{\epsilon})$, where ϵ refers to a predetermined threshold [143]. Hence, the total complexity of solving (8.12) is $\mathcal{O}((MK)^4 L^{1/2}) \log(\frac{\mu_{\max} - \mu_{\min}}{\epsilon})$.

8.2.2 Uplink Weight Control

Similarly in the uplink, given realizations of the large-scale fading and the array steering vectors, we find the weight control coefficients γ_{mk} , $m = 1, \dots, M$, $k = 1, \dots, K$, that maximize the minimum of the uplink rates of all users, under the weight constraint. At the optimum point, all users attain the same rate. So,

$$\begin{aligned} & \max_{\{\gamma_{mk,l}\}} \min_{k=1, \dots, K} R_k^u \\ & \text{subject to } \sum_{k=1}^K \frac{\|\hat{\mathbf{C}}_{mk} \gamma_{mk}\|^2}{\|\hat{\mathbf{C}}_{mk}\|^2} \leq 1, \quad m = 1, \dots, M, \\ & \gamma_{mk,l} \geq 0, \quad \forall k, \quad \forall m, \quad \forall l. \end{aligned} \tag{8.14}$$

Moreover, (8.14) can be solved following the same steps as shown in subsection (8.2.1) in the DL case.

8.2.3 User-Centric (UC) AP Selection Method

As noted from the last term in (8.6) that represents the total power consumption of the backhaul, cell-free massive MIMO systems require more backhaul connections to transfer data between the APs and the CPU when compared to the co-located massive MIMO. Moreover, the second term of (8.8) has a significant effect on the energy efficiency, especially when M increases in (8.6). To improve the total energy efficiency, we can further decrease the denominator of the energy efficiency in (8.5). We present an AP selection for the user-centric case which can reduce the backhaul power consumption, and hence, increase the energy efficiency. The AP selection scheme is based on choosing for each user k a subset of APs \mathcal{M}_k that forms ($\delta\%$) of the total channel power. For a particular user, there are many

APs which are located very far away. These APs will not impact the overall spatial diversity gains. Hence, not all APs actually contribute in serving this user. Furthermore, \mathcal{M}_k is chosen based on the following:

$$\sum_m^{\mathcal{M}_k} \frac{\|\mathbf{A}_{mk}^* \mathbf{B}_{mk}^*\|^2}{\sum_m^M \|\mathbf{A}_{mk} \mathbf{B}_{mk}\|^2} \geq \delta\% \quad (8.15)$$

where $\{\|\mathbf{A}_{1k}^* \mathbf{B}_{1k}^*\|, \dots, \|\mathbf{A}_{Mk}^* \mathbf{B}_{Mk}^*\|\}$ represents the sorted (in descending order) set of the set $\{\|\mathbf{A}_{1k} \mathbf{B}_{1k}\|, \dots, \|\mathbf{A}_{Mk} \mathbf{B}_{Mk}\|\}$. Therefore, by applying the presented AP selection scheme, each access point m serves a subset \mathcal{K}_m of K users. Hence, the power allocation schemes proposed in the preceding subsections will allocate power $\gamma_{mk}^* = \gamma_{mk}$ if $k, m \in \mathcal{K}_m, \mathcal{M}_k$, respectively, and $\gamma_{mk}^* = \mathbf{0}_{L \times 1}$ otherwise. Therefore, Algorithm 5 can be directly applied where $\mathbf{\Gamma}_{mk}$ is replaced by $\mathbf{0}_{L \times L}$ when $m \notin \mathcal{M}_k$ for $k \in \mathcal{K}_m$.

8.3 Experimental Simulation Results

In this section, we study the performance of the proposed multipath components estimation compared to conventional schemes, and we provide numerical results to quantitatively study the performance of FDD cell-free massive MIMO in terms of downlink and uplink spectral efficiency for all the proposed beamforming and combining techniques.

8.3.1 Experimental Setup and Parameters

The APs and the users are located within a square of 1×1 km². The square is wrapped around at the edges to avoid boundary effects. Furthermore, for simplicity, random pilot assignment is used. With random pilot assignment, each

Table 8.1: Simulation Parameters

Parameter	Value
Cell radius (D)	1 km
System Bandwidth (B)	100 MHz
Uplink/Downlink Frequencies	49.8/50 GHz
Uplink pilot training transmit power ρ	200 mW
Uplink transmit power ρ^u	200 mW
Downlink transmit power ρ^d	1000 mW
Power amplifier parameter ϑ	0.2
Internal power consumption/each backhaul, $P_{tc,m}\forall m$ [33]	0.2 W
Fixed power consumption/each backhaul, $P_{0,m}\forall m$ [33]	0.825 W
Traffic dependent backhaul power, $P_{bt,m}\forall m$ [33]	0.25 W/(Gbits/s)
User Centric threshold (δ)	95%
Angle coherence interval (τ_c)	200 samples
Monte-Carlo Simulations	1000

user randomly chooses a pilot sequence from a predefined set of orthogonal pilot sequences of length $\tau = K$. The large-scale fading coefficient $\beta_{l,mk}$ is modeled as the product of path loss and shadow fading as in [116]:

$$10 \log_{10}(\beta_{l,mk}) = \begin{cases} P - 37.6 \log_{10}(u_{mk}) + z_{mk,l} - 15 \log_{10}(u_1), & \text{if } u_{mk} > u_1; \\ P - 35 \log_{10}(u_{mk}) + z_{mk,l}, & \text{if } u_{mk} \leq u_1. \end{cases}$$

where u_{mk} is the distance between the m th AP and k th user in kilometers, $z_{mk,l} \sim \mathcal{N}(0, \sigma_z^2)$ is the shadow fading variable with $\sigma_z = 8$ dB, $u_1 = 0.05$ km and $P = -148$ dB for line-of-sight (LOS) and $P = -158$ dB for non-line-of-sight (NLOS) propagation.

Moreover, for the AP selection schemes, we choose $\delta = 95\%$. The system parameters used throughout the experimental simulations are summarized in Table 8.1.

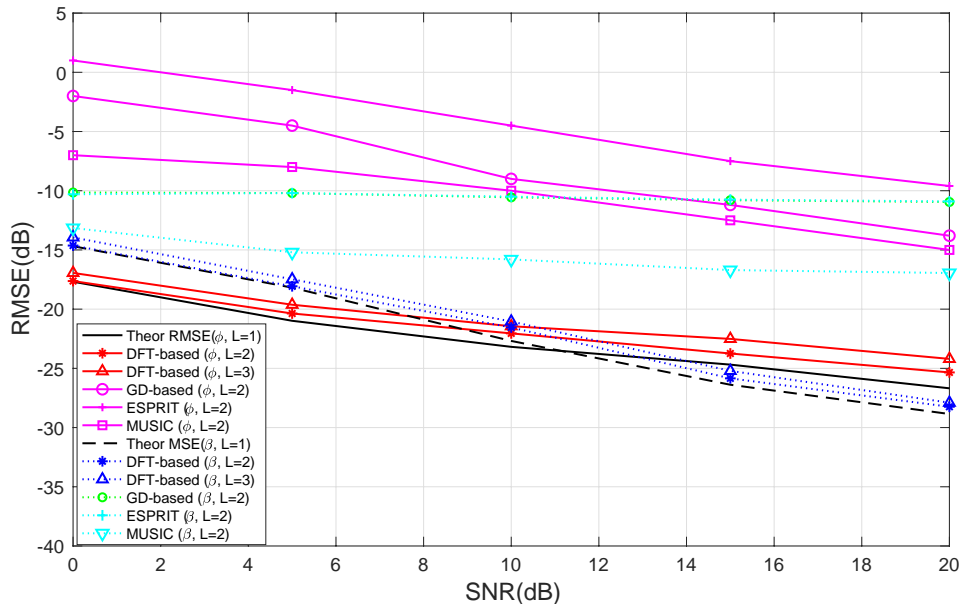


Figure 8.1: RMSE performance of the multipath component estimation versus SNR for $N = 32$ and $T = 16$ compared with the gradient-descent based estimation and subspace-based estimation.

8.3.2 Results and Discussions

Performance of Multipath Component Estimation

In Fig. 8.1, the root mean-square error (RMSE) of the presented multipath component estimation technique is evaluated for $N = 32$ and $T = 16$. We compare the performance of the presented method with that of MUSIC and ESPRIT algorithms, which are subspace-based multipath component estimation techniques that depend on the correlation matrix of the received data [106, 107] and the gradient-descent-based algorithm [116]. The plots demonstrate that the proposed DFT-based technique outperforms the conventional approaches in [106, 107] and [116]. Also, the normalized RMSE performance of the proposed large-scale fading coefficient estimation outperforms that of conventional subspace-based estimation [106, 107] and gradient-descent-based estimation [116]. The large scale fading estimation in [106, 107, 116] cannot work well when number of

samples (snapshots) T is small.

Moreover, it can be seen that the presented AoA estimation and the large-scale fading estimation method performs slightly worse than that of theoretical bound in (7.33) since the search grid is large enough ($\mathcal{G} = 100$).

Performance of Spectral Efficiency

We compare the performance of the proposed angle-based beamforming and combining schemes (A-MF/A-ZF and A-MMSE) for the FDD-based cell-free massive MIMO with the conventional ideal beamforming and combining schemes (MF/ZF and MMSE) in terms of spectral efficiency for the case of $M = 10$ APs with $N = 32$ antennas and $K = 20$ users. We consider the conventional full-channel-based beamforming and combining schemes (MF/ZF and MMSE) as benchmarks, but they are inapplicable in a realistic FDD cell-free massive MIMO system since complete channel knowledge requires large amount of signaling overhead and feedback.

For the downlink scenario in Fig. 8.2(a), and for the uplink scenario in Fig. 8.2(b), the spectral efficiency of the proposed beamforming/combining schemes with imperfect multipath component estimation is shown. As shown in the figures, the A-MMSE beamforming/combining outperforms A-ZF and A-MF beamforming/combining, due to their ability to suppress interference and noise. In addition, at high SNR (low noise) the A-ZF matches A-MMSE in performance as both of the schemes are able to suppress interference. Moreover at moderate to high SNR values, A-MMSE, A-ZF, and A-MF lead to about 10 – 40% sum rate loss compared to the conventional ideal beamforming/combining schemes (MF/ZF and MMSE). However, with the proposed angle-based beamforming schemes, the DL CSI signaling overhead is avoided.

Finally, we evaluate the validity of our closed-form expression for the downlink achievable rate for the proposed angle based beamformers given in (8.3) with imperfect multipath component estimation. In Fig. 8.2(a), we show the accuracy of the proposed closed form of the proposed angle based beamformers (8.3) with the simulated form (8.16)

$$\tilde{R}^d = \sum_{k=1}^K \mathbb{E} \left[\log_2 \left(1 + \frac{\rho^d \sum_{m=1}^M \|\mathbf{h}_{mk}^H \hat{\mathbf{w}}_{mk}\|^2}{\rho^d \sum_{j \neq k}^K \sum_{m=1}^M \|\mathbf{h}_{mj}^H \hat{\mathbf{w}}_{mj}\|^2 + \sigma_n^2} \right) \right]. \quad (8.16)$$

Moreover, (8.16) represents the achievable rate for genie-aided users that know the instantaneous channel gain [32].

In Fig. 8.2(b), we also validate the closed-form expression for the uplink achievable rate for the proposed angle based combining given in (8.4) for imperfect multipath component estimation with simulated form (8.17)

$$\tilde{R}^u = \sum_{k=1}^K \mathbb{E} \left[\log_2 \left(1 + \frac{\rho^u \sum_{m=1}^M \|\mathbf{h}_{mk}^H \hat{\mathbf{v}}_{mk}\|^2}{\rho^u \sum_{j \neq k}^K \sum_{m=1}^M \|\mathbf{h}_{mj}^H \hat{\mathbf{v}}_{mj}\|^2 + \Upsilon_\sigma} \right) \right]. \quad (8.17)$$

where $\Upsilon_\sigma = \sigma_n^2 \sum_{m=1}^M \|\hat{\mathbf{v}}_{mk}\|^2$.

One can notice that the closed form achievable rate perfectly matches with Monte Carlo simulated rates. This indicates that our derived expressions (8.3) and (8.4) are valid performance predictors of the proposed FDD-based cell-free massive MIMO system.

Effect of the Number of APs M for a Fixed Total Number of Service Antennas (NM)

Furthermore, we examine the performance of the proposed FDD-based cell-free massive MIMO system with different numbers of APs for the downlink case.

For fair comparison, the total transmit power in the network is the same, and the number of total service antennas is fixed, i.e. $NM = 320$. Figure 8.3(a) shows the average spectral efficiency ($\kappa \times \sum_k^K R_k^d$ where $\kappa = 1 - \frac{\tau}{\tau_c}$, $\tau = K$ corresponds to the length of pilot training sequence in samples, and τ_c corresponds to the angle coherence interval in samples) as a function of the number of APs. We are able to compare the spectral efficiency of cell-free massive MIMO and co-located massive MIMO where the co-located massive MIMO corresponds to the case $M = 1$. It can be seen that the spectral efficiency of the cell-free massive MIMO (for $M = 10$ and $N = 32$) is better than that of the co-located massive MIMO ($M = 1$ and $N = 320$) due to spatial diversity gains. However, as the number of APs increases while decreasing the number of antennas per AP, the performance of the cell-free massive MIMO starts to decay. The main reasons for this decay are: 1) for a particular user, there are many APs which are located very far away. These APs will not add significantly to the overall spatial diversity gains which implies that not all APs really participate in serving this user; and 2) angle-based beamforming performs better for higher number of antennas.

Effect of the Number of Antennas per AP

Finally, to support our findings in Fig. 8.3(a), we study the performance of FDD-based cell-free massive MIMO system with different numbers of antennas per AP for a fixed number of APs ($M = 10$) in Fig. 8.3(b). As the number of antennas increases, the spectral efficiency increases due to the increased array gain in addition to the applied angle-based beamforming. It can be seen that the spectral efficiency saturates for $N \geq 32$ as no further gains are attained.

Performance of the Proposed Power/Weight Control on DL/UL Spectral Efficiency

We compare the DL/UL spectral efficiency performance of the proposed angle-based beamforming and combining schemes (A-ZF and A-MMSE) for the FDD-based cell-free massive MIMO with equal power allocation, water-filling power allocation and the proposed max-min power/weight control for the CF case (AP selection is not applied) and the UC case (AP selection is applied). One can note that the water-filling PC approach is based only on the angle and large-scale fading parameters in which the allocated power is

$$\rho_{mk} = \max\left\{\frac{1}{\mathcal{K}_m} \left(\rho^{\text{tot}} + \sum_{k \in \mathcal{K}_m} \sigma_n^2 (\|\mathbf{A}_{mk} \mathbf{B}_{mk}\|^2)^{-1} \right) - \sigma_n^2 (\|\mathbf{A}_{mk} \mathbf{B}_{mk}\|^2)^{-1}, 0\right\},$$

where $\rho^{\text{tot}} = \mathcal{K}_m \rho^{\text{d}}$ is the total power, and $\mathcal{K}_m = K$ only if the UC AP selection is not applied. Moreover, the water-filling PC approach is applicable in the DL direction, since only the APs have the knowledge of the angle and large scale fading parameters, whereas for the UL direction the users cannot have this information due to the incurred high signaling overhead.

For the downlink scenario in Figs. 8.4(a) and 8.5(a), and for the uplink scenario in Figs. 8.4(b) and 8.5(b), the spectral efficiency using the proposed max-min power/weight control schemes is significantly enhanced compared to the case of equal power control and water-filling power control, especially at high SNR values. In particular, as shown in Fig. 8.4(a), the DL sum-rate of the proposed A-MMSE and A-ZF beamforming using max-min power control is increased by 12%-38% compared to the equal power allocation case. While, in Fig. 8.4(b), the UL sum rate of the proposed A-MMSE and A-ZF combining using max-min weight control is increased by 10%-25% due to the fact that the

downlink uses more power (since $\rho^d > \rho^u$) and has more power control coefficients to choose than the uplink does, hence the DL performance is better than the UL performance. Moreover, as shown in Figs. 8.4, and 8.5, the UC approach has better performance than that of the CF case since the UEs obtain very noisy signals from the far APs, and not all APs actually participate in serving the users.

In addition, the cumulative distribution function (CDF) curve for the proposed max-min power control scheme is plotted in Fig. 8.6(a), and compared with the equal PC and the water-filling PC schemes at SNR= 10 dB. As expected, the max-min PC scheme was able to outperform the rest of the PC schemes and improve the system fairness for both cases CF and UC, respectively.

Energy Efficiency versus Number of APs M and a Fixed Total Number of Service Antennas (NM)

Figure 8.6(b) examines the energy efficiency (8.5) as a function of the number of AP for a fixed total number of service antennas, when the number of AP increases, the number of antennas per AP decreases. As shown, the energy efficiency while applying the proposed max-min power control significantly outperforms that of equal power control by 40%-50%, especially when the UC AP selection scheme is applied. Furthermore, we are able to compare the energy efficiency of cell-free massive MIMO and co-located massive MIMO where the co-located massive MIMO corresponds to the case $M = 1$. It can be seen that the energy efficiency of the cell-free massive MIMO (for $M = 10$ and $N = 32$) is better than that of the co-located massive MIMO ($M = 1$ and $N = 320$) due to spatial diversity gains, and better spectral efficiency as shown in Fig. 8.3(a). Moreover, the number of APs will affect the level of backhaul power consumption; therefore,

as the number of APs increases while decreasing the number of antennas per AP, the performance of the cell-free massive MIMO starts to decay due to the increased backhaul power consumption as shown in (8.8).

Multi-antenna Users extension

In this subsection, we finally study the effect of having multi-antenna users on the proposed FDD cell-free massive MIMO system where each user is equipped with N' antennas. First, the updated channel model is given by

$$\mathbf{H}_{N \times N'} = \sqrt{\frac{1}{L}} \mathbf{A}^{\text{AP}} \mathbf{B} \mathbf{\Lambda}_{\alpha} (\mathbf{A}^{\text{UE}})^{\text{H}}, \quad (8.18)$$

where $\mathbf{A}_{N \times L}^{\text{AP}} = [\mathbf{a}(\phi_1^{\text{AP}}), \dots, \mathbf{a}(\phi_L^{\text{AP}})]$, $\mathbf{B}_{L \times L} = \text{diag}(\sqrt{\beta_1}, \dots, \sqrt{\beta_L})$, $(\mathbf{\Lambda}_{\alpha})_{L \times L} = \text{diag}(\alpha_1, \dots, \alpha_L)$, and $\mathbf{A}_{N' \times L}^{\text{UE}} = [\mathbf{a}(\phi_1^{\text{UE}}), \dots, \mathbf{a}(\phi_L^{\text{UE}})]$. Moreover, the DL spectral efficiency per user is given by

$$\kappa \times \tilde{R}^{\text{d}} = \left(1 - \frac{\tau}{\tau_c}\right) \times \sum_{k=1}^K \mathbb{E} \left[\log_2 \left(1 + \frac{\rho^{\text{d}} \sum_{m=1}^M \|\hat{\mathbf{v}}_{m^*k}^{\text{H}} \mathbf{H}_{mk}^{\text{H}} \hat{\mathbf{w}}_{mk}\|^2}{\rho^{\text{d}} \sum_{j \neq k}^K \sum_{m=1}^M \|\hat{\mathbf{v}}_{m^*k}^{\text{H}} \mathbf{H}_{mj}^{\text{H}} \hat{\mathbf{w}}_{mj}\|^2 + \sigma_n^2} \right) \right], \quad (8.19)$$

where $\hat{\mathbf{v}}_{m^*k}$ corresponds to the combining vector at the multi-antenna k th user that is based on the estimated AoA of the user from the strongest AP m^* . Moreover, the combining vector $\hat{\mathbf{v}}_{m^*k}$ follows the same definition as the combining vector defined in Section 7.3.2 eq. (7.45), but in this case $\hat{\mathbf{C}}_{m^*} = \hat{\mathbf{A}}_{m^*}^{\text{UE}} \left((\hat{\mathbf{A}}_{m^*}^{\text{UE}})^{\text{H}} \hat{\mathbf{A}}_{m^*}^{\text{UE}} \right)^{-1}$, and the beamforming vector $\hat{\mathbf{w}}_{mk}$ follows the same definition as the A-ZF combining vector defined in Section 7.3.1. The strongest AP m^* is the AP that has the best channel quality with k th user. One can note that only the m^* th AP will need to feed back the combining vector $\hat{\mathbf{v}}_{m^*k}$ to the k th user; hence, no

extensive signaling overhead is needed from all the APs to feed back the estimated multipath components to the k th user. Finally, note that $\tau = KN'$ depends on the number of users K and scales linearly with the number of antennas at the users N' . Therefore, the factor $(1 - \frac{\tau}{\tau_c})$ is an important limiting factor when determining the achievable rates for multi-antenna users.

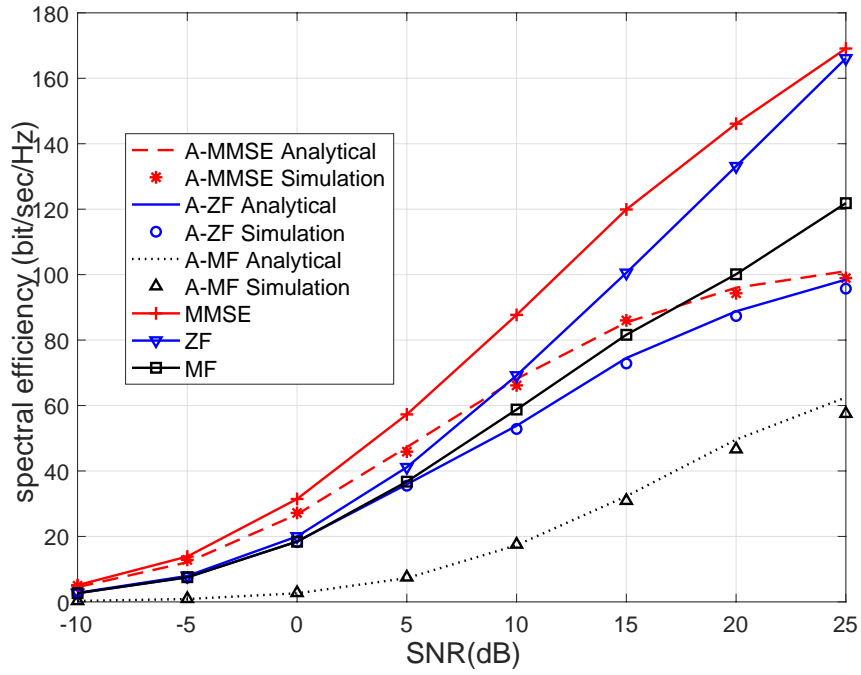
In Fig. 8.7, the performance of the simulated DL spectral efficiency is studied assuming that $\text{RMSE}_{\phi^{\hat{\text{AP}}}} = \text{RMSE}_{\phi^{\hat{\text{UE}}}} = \text{RMSE}_{\hat{\beta}} = -18$ dB. As shown, the DL spectral efficiency first increases when the number of antennas per user increases. However, this spectral efficiency will reach a peak value and then decrease when the number of antennas per user increases. This is due to the fact that although the spatial diversity per user increases, the multipath channel estimation overhead (the training duration relative to the angle coherence interval) also increases. This channel estimation overhead becomes dominant when N' and K are large.

8.4 Conclusion

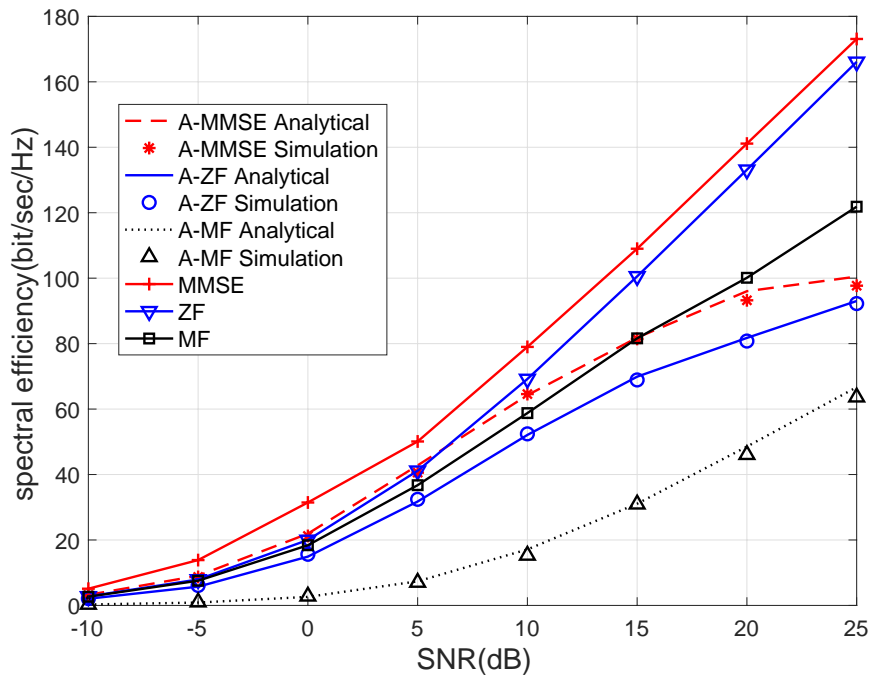
In this work, an FDD-based cell-free massive MIMO system that directly acquires multipath components from the uplink pilot signal and processes them for AP cooperation has been considered. It has been shown that an FDD-based cell-free massive MIMO system is a viable alternative compared to a TDD-based system in which angle reciprocity can be exploited to avoid DL CSI feedback and overhead. A low complexity multipath component (AoA and large-scale fading) estimation technique based on DFT operation, along with angle rotation with very small amount of training overhead and feedback cost, has been presented. To evaluate the benefits of the proposed methods, theoretical bounds on the MSE have been derived and validated. In addition, angle-based beamformers

and combiners, which incur CSI overhead that scales only with the number of served users rather than the total number of serving antennas, have been proposed. Finally, a new max-min power/weight control algorithm and associated AP selection scheme that significantly improve the downlink and uplink sum-rate and energy efficiency compared to equal-power allocation and water-filling power control have been proposed.

The spectral efficiency of the presented FDD-based cell-free massive MIMO system has been shown to outperform that of cell-based systems for an adequate number of antennas at the APs and a small number of APs. Furthermore, when the number of active users in the system is small, the spectral efficiency also improves upon equipping the users with an adequate number of antennas.

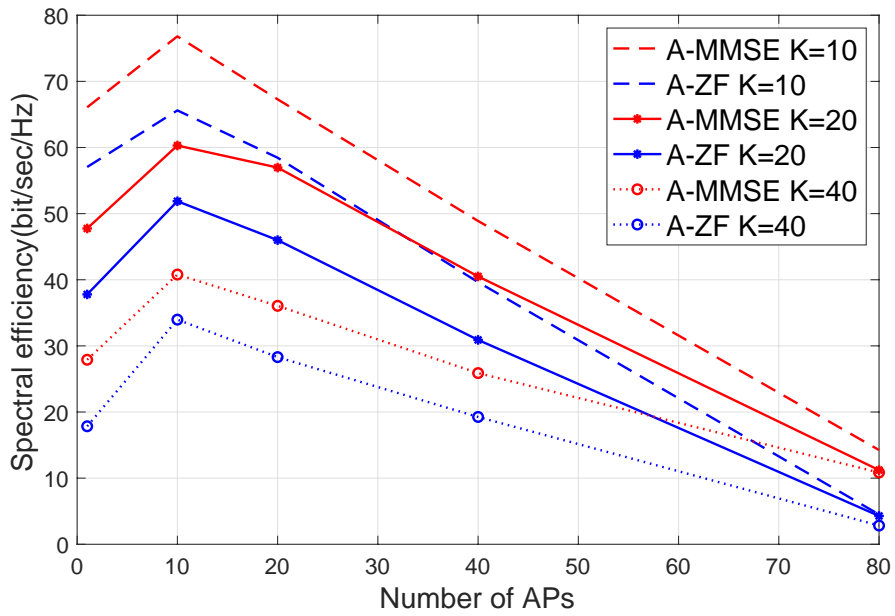


(a)

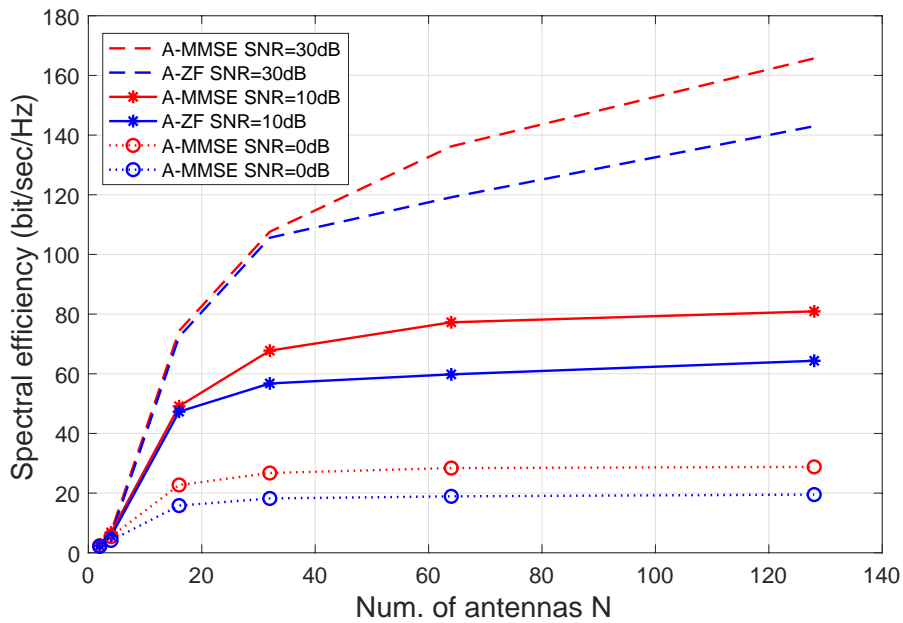


(b)

Figure 8.2: Spectral efficiency of the proposed beamforming schemes versus SNR for $M = 10$ APs with $N = 32$ antennas and $K = 20$ users under imperfect channel estimation: (a) for DL, and (b) UL.

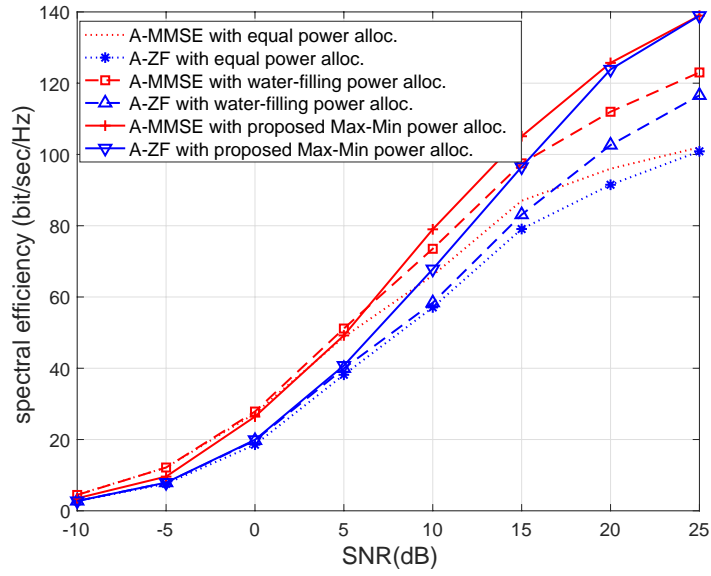


(a)

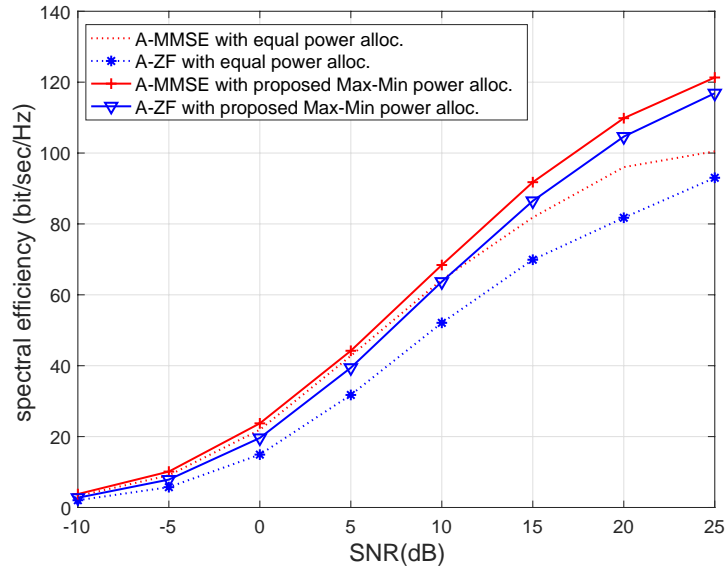


(b)

Figure 8.3: DL sum-rate of the proposed combining schemes versus (a) number of APs at SNR=10 dB for $MN = 320$ and $K = \{10, 20, 40\}$ users, and (b) versus number of antennas N at various SNR values for $M = 10$ APs and $K = 20$ users.

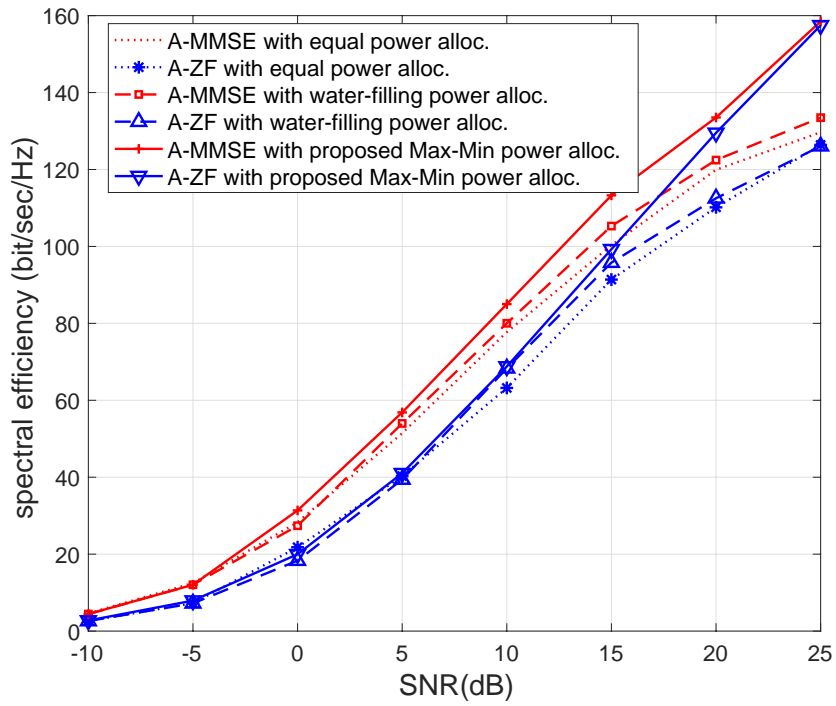


(a)

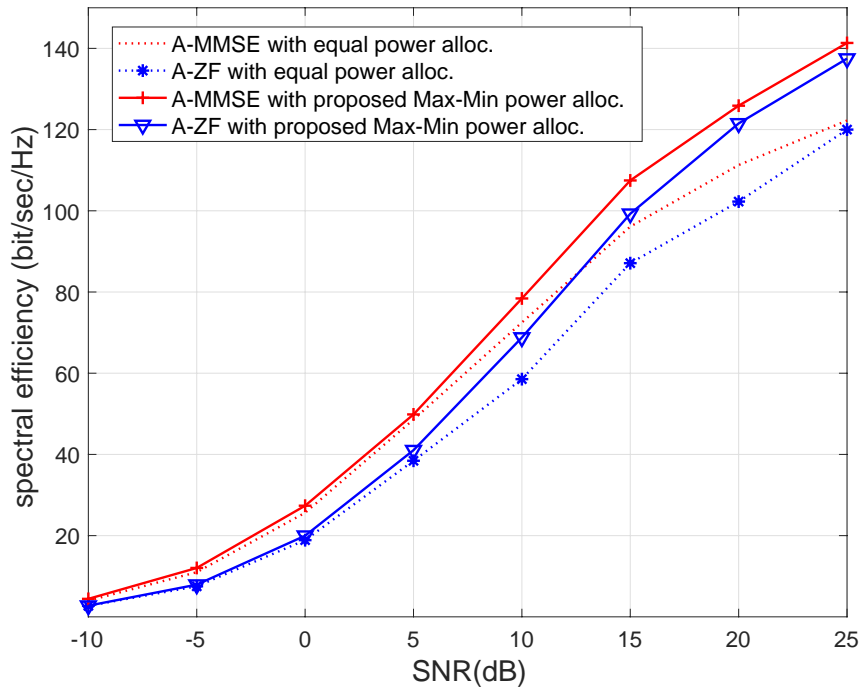


(b)

Figure 8.4: Spectral efficiency of the proposed combining schemes with equal power control, water-filling power control and the proposed max-min power control versus SNR for $M = 10$ APs, and $K = 20$ users for the Cell-Free (CF) massive MIMO (AP selection is not applied): (a) DL and (b) UL.

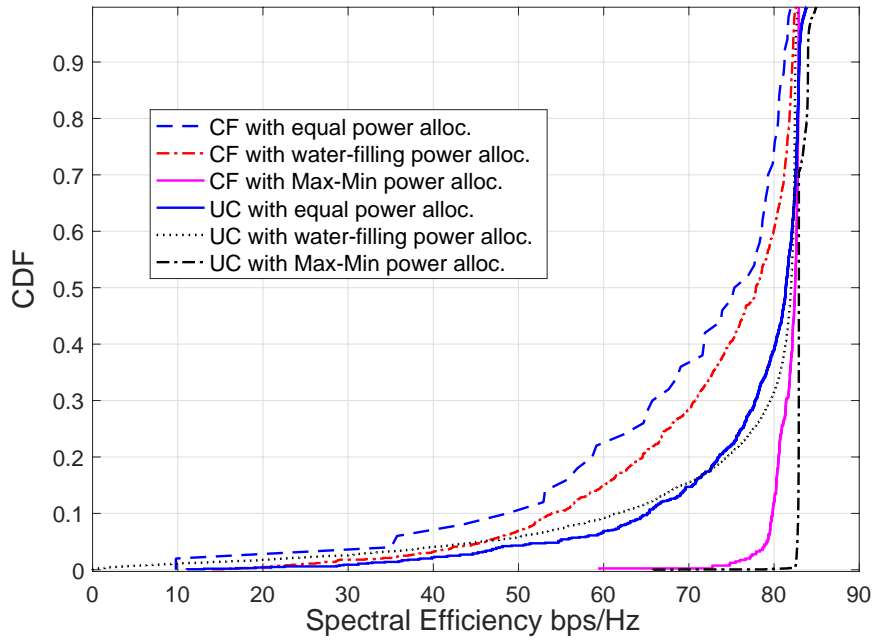


(a)

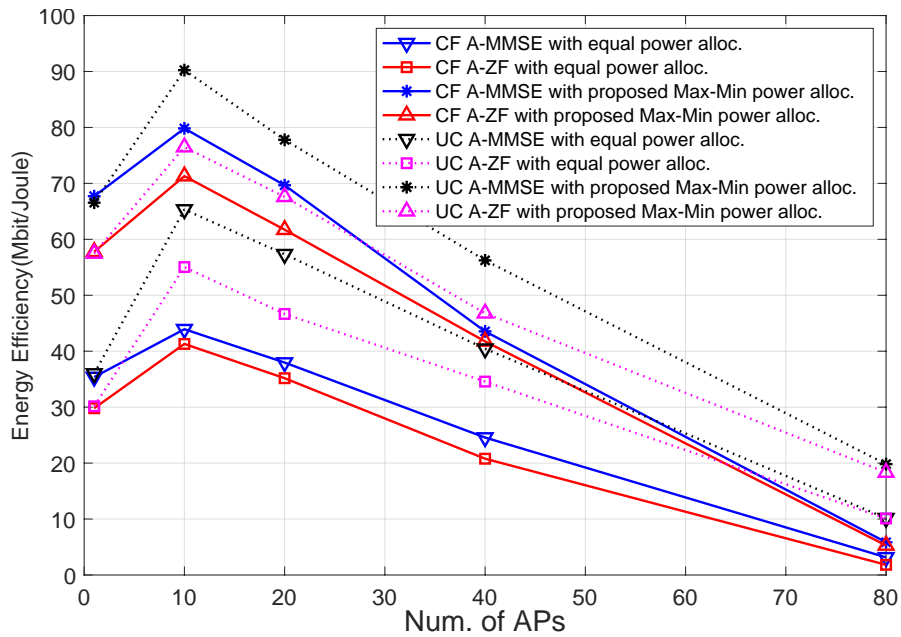


(b)

Figure 8.5: Same as Fig. 8.4 but applying the user centric (UC) AP selection scheme: (a) DL and (b) UL.



(a)



(b)

Figure 8.6: (a) Cumulative distribution of the spectral efficiency for all power control schemes with/without applying the proposed AP selection (CF/UC), and (b) DL energy efficiency of the proposed combining schemes with equal power control and max-min power control versus number of APs. Here, SNR=10 dB for $M = 10$, $N = 32$, and $K = 20$ users.

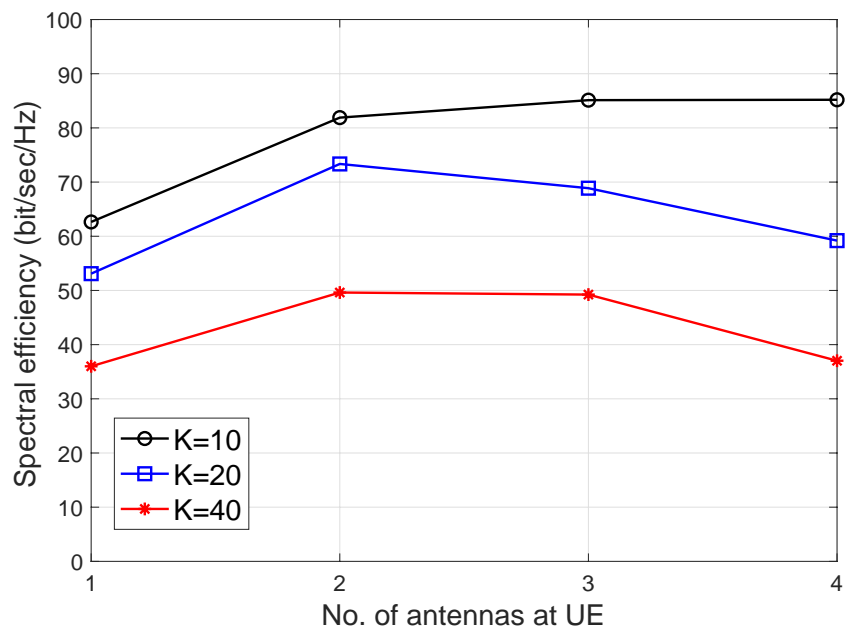


Figure 8.7: DL spectral efficiency versus multiple antenna configurations at the users for $K = \{10, 20, 40\}$, $M = 10$, and $N = 32$.

Chapter 9

Conclusions and Future Work

9.1 Conclusions

The performance of network densification technologies in cellular communications greatly depends on efficient interference mitigation schemes to improve the capacity and spectral efficiency. This dissertation has considered interference mitigation schemes for emerging network densification technologies in 5G communications by proposing and analyzing: 1) channel allocation and power control schemes for D2D and NOMA MIMO systems, 2) baseband processing schemes for quantized massive MIMO systems, 4) angle domain processing techniques for FDD-based cell-free massive MIMO systems, and 5) efficient power control schemes for cell-free massive MIMO while considering the effect of backhaul power consumption.

In the proposed underlaid D2D cellular systems, stochastic geometry has been used to derive closed-form analytical expressions for the coverage probabilities and ergodic sum-rates. These closed form expressions have provided insight into

how the key network parameters such as power allocation, D2D link density, SINR targets affect link performance and quality. It is shown that a channel allocation scheme that allows D2D links to share resources with more than just one cellular user has merit. New power control schemes targeted for D2D link establishment and link maintenance have been shown to adequately control interference levels under various static and dynamic conditions, using distance-based path-loss parameters (with error margin), varying target SINR, and local CSI. It has been shown through experimental simulations that network performance in terms of coverage probability and spectral efficiency is improved by activating more underlaid D2D links while maintaining the quality of cellular links, and at the same time enhancing power efficiency.

In the proposed large MIMO-NOMA system, a low complexity joint clustering and power control scheme has been proposed, that exploits the distance-based path-loss parameter, to guarantee efficient SIC demodulation. An architectural design has been presented, by using the detectors of lower complexity as building blocks in their more complex extensions, and the proposed schemes have been shown to achieve significant computational savings.

Furthermore, using the Bussgang decomposition, a new MMSE-based linear detection scheme that incorporates the non-linear effects of quantization has been proposed. A closed form expression for the uplink achievable rate has been derived, and used to analyze and compare the performance of a quantized massive MIMO system against both a large MIMO system that employs higher-order modulation. In particular, it has been shown that for a few bits of quantization (e.g., 2 or 3 bits), the quantized massive MIMO for the uplink and downlink cases can outperform the conventional MIMO.

And finally, it has been shown that an FDD-based cell-free massive MIMO

system is a viable alternative compared to a TDD-based system in which angle reciprocity can be exploited to avoid DL CSI feedback and overhead. A low complexity multipath component (AoA and large-scale fading) estimation technique based on DFT operation, along with angle rotation with very small amount of training overhead and feedback cost, has been presented. To evaluate the benefits of the proposed methods, theoretical bounds on the MSE have been derived and validated. In addition, angle-based beamformers and combiners, which incur CSI overhead that scales only with the number of served users rather than the total number of serving antennas, have been proposed. Moreover, a new max-min power/weight control algorithm and associated AP selection scheme that significantly improve the downlink and uplink sum-rate and energy efficiency compared to equal-power allocation and water-filling power control have been proposed. The spectral efficiency of the presented FDD-based cell-free massive MIMO system has been shown to outperform that of cell-based systems for an adequate number of antennas at the APs and a small number of APs.

9.2 Open Research Directions and Future work

Network infrastructure densification has been proposed as one of the leading concepts to cope with the growing traffic trends. And, cell-free massive MIMO is a relatively new topic where plenty of directions can be exploited for future work.

There is an endless road of possible improvements and extensions to the results of this dissertation. Deep learning approaches and data-driven algorithm approximation have recently received much attention as key enablers for future wireless networks such as 5G and beyond [145–148]. Signal processing and numerical optimization techniques have been heavily used in addressing wireless

resource management problems such as resource allocation and channel estimation. However, optimization algorithms often require considerable computational complexity and processing overhead, which creates a critical gap between theoretical design/analysis and real-time processing requirements. To overcome these challenges, new learning-based approaches, in the context of channel estimation and resource allocation, need to be studied. The central idea is to treat the input and output of a channel estimation/resource allocation algorithm as an unknown non-linear mapping and use a deep neural network (DNN) to approximate it. Moreover, the deep neural network is trained offline in a time that is fully affordable. Several extensions for future work have been conceived in the process of writing this dissertation:

- Explore deep learning based super-resolution direction of arrivals (DoA) estimation methods in cell-free massive MIMO with low resolution ADCs. A custom-designed DNN can be employed to carry out offline learning and online deployment procedures. This data-driven approximation mechanism can learn the features of the wireless channel efficiently. Our previously proposed channel multipath components estimation algorithm [50, 51] can be used during the training stage to find the optimal training data sets for the considered channel-angle estimation problem. This training procedure can be done under offline setups wherein high complexity algorithms are affordable to train the network. Once the neural network is trained, fewer operations are left to be executed online, i.e., only a few operations need to be repeated sporadically when the system channel realizations vary. This is different from the conventional online channel estimation methods based on the traditional use of optimization theory, which need to be updated every time one or more system channel realizations have changed.

- Investigate deep-learning-based power control approaches for quantized cell-free massive MIMO system. Power control algorithms are needed to conserve energy consumption and to allow scalable implementation in cell-free massive MIMO system [51, 137]. Therefore, deep-learning based power control schemes suitable for interference mitigation shall be studied. Compared with co-located massive MIMO systems, cell-free massive MIMO systems require more backhaul connections to transfer the data between the APs and the CPU. Therefore, the total energy efficiency of the considered cell free massive MIMO system should be studied taking into account the hardware power consumption at the APs and the power consumption of the backhaul links. One can build on our previously proposed optimization-based power control scheme to generate the training data set and perform the offline training of the neural network. The reduced complexity of our proposed semi-definite programming based power control algorithm makes it practical to generate offline large training sets with optimal power allocations.
- Explore beamforming/combining schemes while considering deep learning-based quantized cell-free massive MIMO system. Cell-free massive MIMO systems exhibit remarkably superior achievable rates compared with centralized massive MIMO and conventional small cell systems, especially when the appropriate power control strategy is applied [50, 51, 136, 137]. However, most prior work on distributed MIMO systems equip all nodes with high resolution antennas, which incurs significant costs for distributed cell-free massive MIMO systems, since the hardware cost grows significantly with the quantization bits and sampling rate [106, 107]. To mitigate the hardware cost overhead, the use of low-resolution ADCs is an attractive solution to save both the expenditure and energy at antennas [107–113, 115].

Furthermore, angle-based beamforming and combining schemes shall be studied that incorporate the severity of coarse quantization on cell-free massive MIMO systems. In particular, once the effect of low resolution ADCs is taken into consideration during deep learning-based multipath channel estimation, one can further investigate distributed quantized beamforming/combining schemes and explore performance-complexity tradeoffs. Furthermore, the system performance shall be analyzed by studying the achievable rate.

Appendix A

Proofs

A.1 Proof of Lemma 1

For the case of two cellular users, we have using (3.8):

$$\begin{aligned}
 \mathbb{P}[Q_k = 1] &= \mathbb{P}[\widehat{d_{k,c_1}}^x \geq \widehat{d_{k,c_2}}^y] = \iint_{(x,y;x \geq y)} f_{X,Y}(x,y) dx dy = \int_0^{2R_C} \int_0^x f_Y(y) dy f_X(x) dx \\
 &= \int_0^{2R_C} \underbrace{\int_0^x \frac{2y}{R_C^2} \left(\frac{2}{\pi} \cos^{-1} \left(\frac{y}{2R_C} \right) - \frac{y}{\pi R_C} \sqrt{1 - \frac{y^2}{4R_C^2}} \right) dy}_{\mathcal{A}(x)} f_X(x) dx. \tag{A.1}
 \end{aligned}$$

To solve (A.1), integral $\mathcal{A}(x)$ can be directly computed as follows

$$\mathcal{A}(x) = 1 + \frac{2}{\pi} \left(\frac{x^2}{R_C^2} - 1 \right) \cos^{-1} \left(\frac{x}{2R_C} \right) - \frac{x}{\pi R_C} \left(1 + \frac{x^2}{2R_C} \right) \sqrt{1 - \frac{x^2}{4R_C^2}}.$$

Now using this expression for $\mathcal{A}(x)$, we solve (A.1)

$$\mathbb{P}[d_{k,c_1} \geq d_{k,c_2}] = \int_0^{2R_C} \mathcal{A}(x) \frac{2x}{R_C^2} \left(\frac{2}{\pi} \cos^{-1} \left(\frac{x}{2R_C} \right) - \frac{x}{\pi R_C} \sqrt{1 - \frac{x^2}{4R_C^2}} \right) dx = \frac{1}{2}. \tag{A.2}$$

For the general case of M cellular users, we have:

$$\begin{aligned} \mathbb{P}[\underbrace{d_{k,c_1}}_{y_1} \geq \max\{\underbrace{d_{k,c_2}}_{y_2}, \dots, \underbrace{d_{k,c_M}}_{y_M}\}] &= \int \cdots \int_{(y_1, y_i; y_1 \geq y_i)}^M f_{Y_1, Y_2}(y_1, y_2) \cdots f_{Y_1, Y_M}(y_1, y_M) dy_1 \cdots dy_M \\ &= \frac{1}{M} \end{aligned}$$

A.2 Proof of Proposition 1

Using (3.5), the cellular coverage probability is given by

$$\begin{aligned} \bar{\mathcal{P}}_{\text{cov}, C} &= \mathbb{E} \left[\mathbb{P} \left(|h_{0,c_m}|^2 \geq \beta_0 d_{0,c_m}^\alpha \rho_0^{-1} \left(\sum_{x_k \in \Phi'} |h_{0,k}|^2 d_{0,k}^{-\alpha} \rho_k + \sigma^2 \right) \right) \right] \\ &= \mathbb{E} \left[e^{-\beta_0 d_{0,c_m}^\alpha \rho_0^{-1} (\sum_{x_k \in \Phi'} |h_{0,k}|^2 d_{0,k}^{-\alpha} \rho_k + \sigma^2)} \right] \\ &= \mathbb{E} \left[e^{-\beta_0 \sigma^2 d_{0,c_m}^\alpha \rho_0^{-1}} \right] \mathbb{E} \left[e^{-\beta_0 d_{0,c_m}^\alpha \rho_0^{-1} (\sum_{x_k \in \Phi'} |h_{0,k}|^2 d_{0,k}^{-\alpha} \rho_k)} \right] \end{aligned}$$

For the proposed channel allocation scheme, the Laplace transform $\mathcal{L}_{\Phi'}(s)$ is given as

$$\mathcal{L}_{\Phi'}(s) \triangleq \mathbb{E} \left[e^{-s (\sum_{x_k \in \Phi'} |h_{0,k}|^2 d_{0,k}^{-\alpha} \rho_k)} \right] = e^{-\frac{\pi}{\text{sinc}(2/\alpha)} \mathbb{E}[\rho_k^{2/\alpha}] \mathbb{P}[Q_k=1] \lambda s^{2/\alpha}}$$

where $s = \beta_0 d_{0,c_m}^\alpha \rho_0^{-1}$. The result follows. Furthermore, it turns out that the Laplace transform is easier than determining the distribution functions, and it completely characterizes the distribution of PPP [68, 70].

A.2.1 Proof of Proposition 2

We first need to derive the expectation of the interference term from other D2D users. Using Slivnyak's theorem [70] and considering the proposed channel allocation scheme, the reduced PPP excluding the k th point ($\Phi' \setminus x_k$) remains

the same as the original PPP Φ' . Hence,

$$\mathcal{L}_{\Phi' \setminus \{x_k\}}(s) = \mathbb{E} \left[e^{-s \sum_{x_i \in \Phi' \setminus \{x_k\}} \rho_i |h_{k,i}|^2 \|x_i\|^{-\alpha}} | k \in \Phi' \right] = \mathcal{L}_{\Phi'}(s) = e^{-\frac{\pi \mathbb{P}[Q_k=1] \lambda}{\text{sinc}(2/\alpha)} \mathbb{E}[\rho_k^{2/\alpha}] s^{2/\alpha}}.$$

Therefore, the coverage probability of the D2D links is given by

$$\begin{aligned} \mathbb{P}(\text{SINR}_k \geq \beta_k) &= \mathbb{P} \left(|h_{k,k}|^2 \geq \frac{\beta_k d_{k,k}^\alpha}{\rho_k} \left(\sum_{x_i \in \Phi' \setminus \{x_k\}} \frac{\rho_i |h_{k,i}|^2}{\|x_i\|^\alpha} + \frac{\rho_0 |h_{k,c_m}|^2}{d_{k,c_m}^\alpha} + \sigma^2 \right) \right) \\ &= \mathbb{E} \left[e^{-\beta_k \rho_k^{-1} d_{k,k}^\alpha (\sum_{x_i \in \Phi' \setminus \{x_k\}} \rho_i |h_{k,i}|^2 \|x_i\|^{-\alpha} + \rho_0 |h_{k,c_m}|^2 d_{k,c_m}^{-\alpha} + \sigma^2)} \right] \\ &= \mathbb{E}_Z \left[e^{-\sigma^2 \beta_k \rho_k^{-1} d_{k,k}^\alpha} \mathcal{L}_{\Phi'}(\beta_k \rho_k^{-1} d_{k,k}^\alpha) \mathcal{L}_Y(\beta_k \rho_k^{-1} d_{k,k}^\alpha) \right], \end{aligned}$$

where $Z = d_{k,k}^\alpha \rho_k^{-1}$, $Y = |h_{k,c_m}|^2 d_{k,c_m}^{-\alpha} \rho_0$, and $\mathcal{L}_Y(\beta_k Z) = \mathbb{E}_Y[e^{-(\beta_k Z)Y}]$.

A.3 Proof of Corollary 1

For simplicity, we derive the expressions for d_{k,c_1} . The same approach can be used for d_{k,c_2} . We set $D_{c_1} = d_{k,c_1}$ as the distance from any k th D2D transmitter to the cellular UE c_1 such that $d_{k,c_1} \geq d_{k,c_2}$; in other words, $D_{c_1} = d_{k,c_1} \mathbb{1}_{\{d_{k,c_1} \geq d_{k,c_2}\}}$, where $\mathbb{1}$ is the indicator function.

Let $X_1 = d_{k,c_1}$, $X_2 = d_{k,c_2}$ with pdfs $f_{X_1}(x)$ and $f_{X_2}(y)$ as given in (3.8). We can then express the pdf of D_{c_1} as follows:

$$\begin{aligned} f_{D_{c_1}}(x) &= \int_0^x \frac{f_{X_1|X_2}(x|y) \mathbb{P}[X_1 \geq y] f_{X_2}(y)}{\mathbb{P}[X_1 \geq X_2]} dy = \int_0^x \frac{f_{X_1|X_2}(x|y) \mathbb{P}[X_1 \geq y] \frac{2y}{R_C^2} \left(\frac{2}{\pi} \cos^{-1} \left(\frac{y}{2R_C} \right) - \frac{y}{\pi R_C} \sqrt{1 - \frac{y^2}{4R_C^2}} \right)}{\mathbb{P}[\{d_{k,c_1} \geq d_{k,c_2}\}]} dy \\ &= \frac{1}{\mathbb{P}[\{d_{k,c_1} \geq d_{k,c_2}\}]} \left(\frac{2x}{R_C^2} \left(\frac{2}{\pi} \cos^{-1} \left(\frac{x}{2R_C} \right) - \frac{x}{\pi R_C} \sqrt{1 - \frac{x^2}{4R_C^2}} \right) \right) \\ &\quad \times \left(1 + \frac{2}{\pi} \left(\frac{x^2}{R_C^2} - 1 \right) \cos^{-1} \left(\frac{x}{2R_C} \right) - \frac{x}{\pi R_C} \left(1 + \frac{x^2}{2R_C} \right) \sqrt{1 - \frac{x^2}{4R_C^2}} \right). \end{aligned}$$

The n th moment of X_1 is obtained by computing $\int_0^{2R_C} x^n f_{D_{c_1}}(x)$, from which we deduce that $\mathbb{E}[d_{k,c_1}] \approx \frac{512R_C}{45\pi^2}$.

Remark: When no resource allocation is applied so that all active D2D users share resources with one CUE, the first moment of the distance between two uniformly distributed points is $\mathbb{E}[d_{k,c_1}] = 128R_C/(45\pi)$ [118].

A.4 Proof of Theorem 1

To calculate $\mathbb{E}\left[\rho_k^{\frac{2}{\alpha}}\right] = \mathbb{E}\left[\min(U^{\frac{2}{\alpha}}d_{k,k}^2, V^{\frac{2}{\alpha}}d_{0,k}^2)\right]$, we let $A = U^{\frac{2}{\alpha}}d_{k,k}^2$ and $B = V^{\frac{2}{\alpha}}d_{0,k}^2$. Using the Jacobian transformation [149], we have $f_A(a) = \frac{1}{R_D^2 U^{\frac{2}{\alpha}}}$, $F_A(a) = \frac{a}{R_D^2 U^{\frac{2}{\alpha}}}$, $f_B(b) = \frac{1}{R_C^2 V^{\frac{2}{\alpha}}}$ and $F_B(b) = \frac{b}{R_C^2 V^{\frac{2}{\alpha}}}$. Then,

$$\begin{aligned} \mathbb{E}\left[\rho_k^{\frac{2}{\alpha}}\right] &= \int_{-\infty}^{\infty} \int_{-\infty}^{\infty} \min(a, b) f_A(a) f_B(b) da db \\ &= \int_{-\infty}^{\infty} a f_A(a) \left(\int_a^{\infty} f_B(b) db \right) da + \int_{-\infty}^{\infty} b f_B(b) \left(\int_b^{\infty} f_A(a) da \right) db \\ &= \int_{-\infty}^{\infty} a f_A(a) (1 - F_B(a)) da + \int_{-\infty}^{\infty} b f_B(b) (1 - F_A(b)) db \\ &= \int_{-\infty}^{\infty} a f_A(a) da + \int_{-\infty}^{\infty} b f_B(b) db - \left(\int_{-\infty}^{\infty} a f_A(a) F_B(a) da + \int_{-\infty}^{\infty} b f_B(b) F_A(b) db \right) \\ &= \mathbb{E}[A] + \mathbb{E}[B] - \mathbb{E}[\max(A, B)]. \end{aligned}$$

A.5 Proof of Lemma 2

Let A and B be two random variables with pdfs $f_A(a)$ and $f_B(b)$, and cdfs $F_A(a)$ and $F_B(b)$, respectively. Then,

$$\mathbb{E}[\max(A, B)] = \int_{-\infty}^{\infty} \int_{-\infty}^{\infty} \max(a, b) f_A(a) f_B(b) da db$$

$$= \int_{-\infty}^{\infty} a f_A(a) \left(\int_{-\infty}^a f_B(b) db \right) da + \int_{-\infty}^{\infty} b f_B(b) \left(\int_{-\infty}^b f_A(a) da \right) db$$

from which the result follows.

A.6 Proof of Corollary 2

To calculate $\mathbb{E}[\max(A, B)]$, we consider two cases.

Case 1: If $R_D^2 U^{2/\alpha} \triangleq a' > b' \triangleq R_C^2 V^{2/\alpha}$. Then, applying (4.15), we have

$$\begin{aligned} \mathbb{E}[\max(A, B)] &= \int_0^{b'} a f_A(a) F_B(a) da + \int_{b'}^{a'} a f_A(a) \times 1 da + \int_0^{b'} b f_B(b) F_A(b) db \\ &= \frac{b'^2}{3a'} + \frac{a'^2 - b'^2}{2a'} + \frac{b'^2}{3a'} = \frac{b'^2}{6a'} + \frac{a'}{2} \\ &= \frac{R_C^4 V^{4/\alpha}}{6R_D^2 U^{2/\alpha}} + \frac{R_D^2 U^{2/\alpha}}{2} \end{aligned}$$

Case 2: If $a' \leq b'$, then following the same approach, we obtain

$$\mathbb{E}[\max(A, B)] = \frac{a'^2}{6b'} + \frac{b'}{2} = \frac{R_D^4 U^{4/\alpha}}{6R_C^2 V^{2/\alpha}} + \frac{R_C^2 V^{2/\alpha}}{2}$$

A similar expression for $\mathbb{E}[\min(A, B)]$ can be easily derived by applying Theorem 1.

Appendix B

Abbreviations

1G	First generation
2D-DFT	Two dimensional discrete Fourier transform
3GPP	Third Generation Partnership Project
4G	Fourth generation
5G	Fifth generation
A-MF	A-MF Angle based Matched Filter
A-MMSE	Angle-Based MMSE Beamforming
A-ZF	Angle-Based Zero-Forcing Beamforming
ADC	Analog-to-digital converter
AoA	Angle of Arrival
AoD	Angle of Departure
AP	Access points
BER	Bit error rate
BS	Base station
CA	Channel allocation

CD	Chase detector
CDF	Commulative distribution function
CF	Cell-free
CLPC	Closed loop PC
CPU	Central processing unit
CSI	Channel state information
CUE	Cellular User Equipment
D2D	Device-to-device
DAC	Digital-to-analog converter
DFT	Discrete Fourier transform
DL	Downlink
DNN	Deep neural network
DoA	direction of arrivals
DPCC	Distance-based Path-loss Power Control
EDPCC	Extended Distance-based Path-loss Power Control
eNB	E-Node B
ESPRIT	Estimation of signal parameters via rotational invariance technique
FDD	Frequency-division duplexing
FFT	Fast Fourier transform
GAD	Geographical area description
HetNet	Heterogeneous Network
ICI	Inter-cell interference
JDCP	Joint distance-based path-loss clustering and power control scheme
LORD	Layered orthogonal lattice detector
LOS	Line-of-sight
LR	Lattice reduction

LTE	Long Term Evolution
MIMO	Multiple-input and multiple-output
ML	Maximum likelihood
MMSE	Minimum mean square error
mmWave	Millimeter wave
MRC	Maximal ratio combining
MSE	Mean Square Error
MUSIC	Multiple signal classification
NC	Nulling-and-cancellation
NLOS	Non-line-of-sight
NOMA	Non-orthogonal multiple access
OLPC	Open loop PC
OMA	Orthogonal multiple access
PC	Power control
PCD	Punctured CD
PNC	Punctured NC
PPP	Poison point process
PRB	Physical resource block
PSBCH	Physical Sidelink Broadcast Channel
PSCCH	Physical Sidelink Control Channel
PSD	Positive semidefinite
QCQP	Quadratically-constrained quadratic program
QoS	Quality of service
QRD	QR decomposition
RF	Radio-frequency
RMSE	Root mean-square error

RSRP	Reference signal received power
RX	Receiver
SD	Sphere decoders
SD	Superposition coding
SDDPC	Soft Dropping Distance-based Power Control
SDP	Semi-definite program
SDR	Semi-definite relaxation
SIC	Successive interference cancellation
SINR	Signal-tointerference-plus-noise ratio
SNR	Signal-to-noise ratio
SSD	Subspace detector
SVD	Singular value decomposition
TDD	Time-division duplex
TTI	Transmission time interval
TX	Transmitter
UC	User-Centric
UE	User Equipment
UL	Uplink
ULA	Uniform linear array
WRD	WR decomposition
ZF	Zero forcing

Appendix C

Notations

$\mathbb{E}[\cdot]$	Expectation of an event
$\mathbb{P}[\cdot]$	Probability of an event
\mathcal{L}_X	Laplace transform of a variable X
$\mathcal{P}_{\text{cov},L}$	Coverage probability of link L
$F_X(\cdot)$	Cumulative distribution function (cdf) of variable X
$f_X(\cdot)$	Probability density function (pdf) of variable X
x	Scalar
\mathbf{x}	Vector
\mathbf{X}	Matrix
$ \cdot $	Scalar norms
$\ \cdot\ $	Vector L_2 norm
$\ \cdot\ _F$	Frobenius norms
$(\cdot)^\top$	Transpose of a vector or matrix
$(\cdot)^*$	Complex conjugate
$(\cdot)^H$	Hermitian

\mathbf{P}^\perp	Orthogonal projection matrix
$\text{tr}(\cdot)$	Trace of a matrix
\mathbf{X}^\dagger	Pseudo-inverse $(\mathbf{X}^H \mathbf{X})^{-1} \mathbf{X}^H$
$\mathbf{X} \succeq \mathbf{0}$	\mathbf{X} is a positive semi-definite matrix
$[\mathbf{x}]_i$	i th element of a vector \mathbf{x}
$[\mathbf{X}]_{ij}$	(i, j) th element is given by \mathbf{X}
$\mathcal{CN}(0, \sigma^2)$	Circularly-symmetric complex Gaussian distribution with zero mean and variance σ^2
$\text{diag}\{\mathbf{X}\}$	Diagonal of a matrix \mathbf{X} .
$\mathbb{C}^{N \times M}$	The set of complex-valued $N \times M$ matrices
$\forall x$	Means that a statement holds for all x (in the set that x belongs to)
$\Re\{\cdot\}$	Real part of a complex scalar
$\Im\{\cdot\}$	Imaginary part of a complex scalar

Bibliography

- [1] N. Lee, X. Lin, J. G. Andrews, and R. Heath, “Power control for D2D underlaid cellular networks: Modeling, algorithms, and analysis,” *IEEE J. Sel. Areas Commun.*, vol. 33, no. 1, pp. 1–13, Jan. 2015.
- [2] A. Memmi, Z. Rezki, and M. Alouini, “Power control for D2D underlay cellular networks with channel uncertainty,” *IEEE Trans. Wireless Commun.*, vol. 16, no. 2, pp. 1330–1343, Feb. 2017.
- [3] W. R. Young, “Advanced mobile phone service: Introduction, background, and objectives,” *The Bell System Technical Journal*, vol. 58, no. 1, pp. 1–14, Jan 1979.
- [4] H. Viswanathan and M. Weldon, “The past, present, and future of mobile communications,” *Bell Labs Technical Journal*, vol. 19, pp. 8–21, Aug. 2014.
- [5] J. G. Andrews, X. Zhang, G. D. Durgin, and A. K. Gupta, “Are we approaching the fundamental limits of wireless network densification?” *IEEE Commun. Mag.*, vol. 54, no. 10, pp. 184–190, October 2016.
- [6] J. Liu, M. Sheng, L. Liu, and J. Li, “Network densification in 5G: From the short-range communications perspective,” *IEEE Commun. Mag.*, vol. 55, no. 12, pp. 96–102, Dec. 2017.
- [7] K. Doppler *et al.*, “Device-to-device communication as an underlay to LTE-advanced networks,” *IEEE Commun. Mag.*, vol. 47, no. 12, pp. 42–49, Dec. 2009.
- [8] M. S. Corson *et al.*, “Toward proximity-aware internetworking,” *IEEE Trans. Wireless Commun.*, vol. 17, no. 6, pp. 26–33, Dec. 2010.
- [9] G. Fodor *et al.*, “Design aspects of network assisted device-to-device communications,” *IEEE Commun. Mag.*, vol. 50, no. 3, pp. 170–177, Mar. 2012.

- [10] *Feasibility study for Proximity Services (ProSE) (Release 12)*, 3GPP Std. TR 22.803. [Online]. Available: <http://www.3gpp.org>
- [11] X. Lin, J. Andrews, A. Ghosh, and R. Ratasuk, "An overview of 3GPP device-to-device proximity services," *IEEE Commun. Mag.*, vol. 52, no. 4, pp. 40–48, May 2014.
- [12] P. Mach, Z. Becvar, and T. Vanek, "In-band device-to-device communication in OFDMA cellular networks: A Survey and Challenges," *IEEE Commun. Surveys Tuts.*, vol. 17, no. 4, pp. 1885–1922, Jun. 2015.
- [13] *IEEE Standard for local and metropolitan area networks – Part 11: Wireless LAN Medium Access Control (MAC) and Physical Layer (PHY)*, IEEE Std. 802.11, 2012. [Online]. Available: <http://standards.ieee.org/getieee802/802.11.html>
- [14] *IEEE Standard for Air Interface for Broadband Wireless Access Systems*, IEEE Std. 802.16, 2012. [Online]. Available: <http://standards.ieee.org/getieee802/802.16.html>
- [15] *Physical channels and mapping of transport channels onto physical channels*, 3GPP Std. TS 25.211. [Online]. Available: <http://www.3gpp.org>
- [16] *Evolved Universal Terrestrial Radio Access (E-UTRA); Physical Channels and Modulation*, 3GPP Std. TS 36.211. [Online]. Available: <http://www.3gpp.org>
- [17] L. Dai, B. Wang, Y. Yuan, S. Han, C. I, and Z. Wang, "Non-orthogonal multiple access for 5G: solutions, challenges, opportunities, and future research trends," *IEEE Communications Magazine*, vol. 53, no. 9, pp. 74–81, Sep. 2015.
- [18] Z. Ding, X. Lei, G. K. Karagiannidis, R. Schober, J. Yuan, and V. K. Bhargava, "A survey on non-orthogonal multiple access for 5G networks: Research challenges and future trends," *IEEE J. Sel. Areas Commun.*, vol. 35, no. 10, pp. 2181–2195, Oct, 2017.
- [19] A. Benjebbour, Y. Saito, Y. Kishiyama, A. Li, A. Harada, and T. Nakamura, "Concept and practical considerations of non-orthogonal multiple access (NOMA) for future radio access," in *2013 International Symposium on Intelligent Signal Processing and Communication Systems*, Nov. 2013, pp. 770–774.
- [20] L. Dai, B. Wang, Z. Ding, Z. Wang, S. Chen, and L. Hanzo, "A survey of non-orthogonal multiple access for 5G," *IEEE Commun. Surveys Tuts.*, vol. 20, no. 3, pp. 2294–2323, thirdquarter 2018.

- [21] A. Paulraj, R. Nabar, and D. Gore, *Introduction to space-time wireless communications*. Cambridge university press, 2003.
- [22] E. G. Larsson, O. Edfors, F. Tufvesson, and T. L. Marzetta, “Massive MIMO for next generation wireless systems,” *IEEE Commun. Mag.*, vol. 52, no. 2, pp. 186–195, Feb. 2014.
- [23] R. Walden, “Analog-to-digital converter survey and analysis,” *IEEE J. Sel. Areas Commun.*, vol. 17, no. 4, pp. 539–550, Apr. 1999.
- [24] S. Jacobsson, G. Durisi, M. Coldrey, U. Gustavsson, and C. Studer, “Throughput analysis of massive MIMO uplink with low-resolution ADCs,” *IEEE Trans. Wireless Commun.*, vol. 16, no. 6, pp. 4038–4051, Jun. 2017.
- [25] C. Kong, A. Mezghani, C. Zhong, A. L. Swindlehurst, and Z. Zhang, “Multipair massive MIMO relaying systems with one-bit ADCs and DACs,” *IEEE Trans. Signal Process.*, vol. 66, no. 11, pp. 2984–2997, Jun. 2018.
- [26] J. Zhang, L. Dai, Z. He, S. Jin, and X. Li, “Performance analysis of mixed-ADC massive MIMO systems over Rician fading channels,” *IEEE J. Sel. Areas Commun.*, vol. 35, no. 6, pp. 1327–1338, Jun. 2017.
- [27] J. Zhang, L. Dai, S. Sun, and Z. Wang, “On the spectral efficiency of massive MIMO systems with low-resolution ADCs,” *IEEE Commun. Lett.*, vol. 20, no. 5, pp. 842–845, May 2016.
- [28] Y. Li *et al.*, “Downlink achievable rate analysis in massive MIMO systems with one-bit DACs,” *IEEE Commun. Lett.*, vol. 21, no. 7, pp. 1669–1672, Jul. 2017.
- [29] S. Jacobsson, G. Durisi, M. Coldrey, T. Goldstein, and C. Studer, “Quantized precoding for massive MU-MIMO,” *IEEE Trans. Commun.*, vol. 65, no. 11, pp. 4670–4684, Jul. 2017.
- [30] J. Zhang, L. Dai, X. Li, Y. Liu, and L. Hanzo, “On low-resolution ADCs in practical 5G millimeter-wave massive MIMO systems,” *IEEE Commun. Mag.*, vol. 56, no. 7, pp. 205–211, Jul. 2018.
- [31] E. Nayebi, A. Ashikhmin, T. L. Marzetta, and H. Yang, “Cell-free massive MIMO systems,” in *Proc. Asilomar Conf. Signals, Systems and Computers (Asilomar)*, Pacific Grove, CA, USA, Nov. 2015, pp. 695–699.
- [32] H. Q. Ngo, A. Ashikhmin, H. Yang, E. G. Larsson, and T. L. Marzetta, “Cell-free massive MIMO versus small cells,” *IEEE Trans. Wireless Commun.*, vol. 16, no. 3, pp. 1834–1850, Mar. 2017.

- [33] H. Q. Ngo, L. Tran, T. Q. Duong, M. Matthaiou, and E. G. Larsson, "On the total energy efficiency of cell-free massive MIMO," *IEEE Trans. on Green Commun. and Netw.*, vol. 2, no. 1, pp. 25–39, Mar. 2018.
- [34] G. Interdonato, E. Björnson, H. Q. Ngo, P. Frenger, and E. G. Larsson, "Ubiquitous cell-free massive MIMO communications," *arXiv preprint arXiv:1804.03421*, 2018.
- [35] S. Zhou, M. Zhao, X. Xu, J. Wang, and Y. Yao, "Distributed wireless communication system: a new architecture for future public wireless access," *IEEE Commun. Mag.*, vol. 41, no. 3, pp. 108–113, Mar. 2003.
- [36] E. Björnson, R. Zakhour, D. Gesbert, and B. Ottersten, "Cooperative multicell precoding: Rate region characterization and distributed strategies with instantaneous and statistical CSI," *IEEE Trans. Signal Process.*, vol. 58, no. 8, pp. 4298–4310, Aug. 2010.
- [37] T. Marzetta, E. Larsson, H. Yang, and H. Q. Ngo, *Fundamentals of massive MIMO*. Cambridge University Press, 2016.
- [38] J. Vieira, F. Rusek, O. Edfors, S. Malkowsky, L. Liu, and F. Tufvesson, "Reciprocity calibration for massive MIMO: Proposal, modeling, and validation," *IEEE Trans. Wireless Commun.*, vol. 16, no. 5, pp. 3042–3056, May 2017.
- [39] E. Björnson, L. V. der Perre, S. Buzzi, and E. G. Larsson, "Massive MIMO in sub-6 GHz and mmWave: Physical, practical, and use-case differences," *arXiv preprint arXiv:1803.11023*, 2018.
- [40] "FDDTDD Comparison," Qualcomm, Tech. Rep. [Online]. Available: <https://www.qualcomm.com/media/documents/files/fdd-tdd-comparison.pdf>
- [41] B. Lee, J. Choi, J. Seol, D. J. Love, and B. Shim, "Antenna grouping based feedback compression for FDD-based massive MIMO systems," *IEEE Trans. Commun.*, vol. 63, no. 9, pp. 3261–3274, Sep. 2015.
- [42] H. Xie, F. Gao, S. Zhang, and S. Jin, "A unified transmission strategy for TDD/FDD massive MIMO systems with spatial basis expansion model," *IEEE Trans. Veh. Technol.*, vol. 66, no. 4, pp. 3170–3184, Apr. 2017.
- [43] V. Va, J. Choi, and R. W. Heath, "The impact of beamwidth on temporal channel variation in vehicular channels and its implications," *IEEE Trans. Veh. Technol.*, vol. 66, no. 6, pp. 5014–5029, Jun. 2017.
- [44] A. Abdallah, M. M. Mansour, and A. Chehab, "Power control and channel allocation for d2d underlaid cellular networks," *IEEE Transactions on Communications*, vol. 66, no. 7, pp. 3217–3234, July 2018.

- [45] A. Abdallah, M. Mansour, and A. Chehab, “Joint channel allocation and power control for D2D communications using stochastic geometry,” in *IEEE WCNC. Conf. (WCNC)*, Barcelona, Spain, 2018, (to appear).
- [46] —, “A distance-based power control scheme for D2D communications using stochastic geometry,” in *Proc. IEEE Vehicular Technol. Conf. (VTC)*, Toronto, ON, Canada, Sep. 2017, pp. 1–6.
- [47] H. Sardeddeen, M. M. Mansour, and A. Chehab, “Large MIMO detection schemes based on channel puncturing: Performance and complexity analysis,” *IEEE Trans. Commun.*, no. 99, pp. 1–1, Dec. 2017.
- [48] A. Abdallah, M. M. Mansour, L. M. A. Jalloul, and A. Chehab, “When quantized massive mimo meets large mimo with higher order modulation,” *IEEE Communications Letters*, vol. 22, no. 12, pp. 2599–2602, Dec. 2018.
- [49] A. Abdallah, M. M. Mansour, A. Chehab, and L. M. A. Jalloul, “Mmse detection for 1-bit quantized massive mimo with imperfect channel estimation,” in *Proc. IEEE Int. Sig. Process. Advances in Wireless Commun. Workshop (SPAWC)*, Kalamata, Greece, June 2018, pp. 1–5.
- [50] A. Abdallah and M. M. Mansour, “Angle-based multipath estimation and beamforming for fdd cell-free massive mimo,” in *Proc. IEEE Int. Sig. Process. Advances in Wireless Commun. Workshop (SPAWC)*, July 2019, pp. 1–5.
- [51] —, “Efficient angle-domain processing for fdd-based cell-free massive mimo systems,” *IEEE Trans. Commun.*, pp. 1–1, 2020.
- [52] G. Fodor *et al.*, “A comparative study of power control approaches for device-to-device communications,” in *Proc. IEEE Int. Conf. Commun. (ICC)*, Budapest, Hungary, Jun. 2013, pp. 6008–6013.
- [53] R. D. Yates, S. Gupta, C. Rose, and S. Sohn, “Soft dropping power control,” in *Proc. IEEE Vehicular Technol. Conf. (VTC)*, Phoenix, AZ, USA, May 1997, pp. 1694–1698.
- [54] Y. de Melo *et al.*, “Power control schemes for energy efficiency of cellular and device-and-device communications,” in *Proc. IEEE Wireless Commun. and Netw. Conf. (WCNC)*, New Orleans, LA, USA, Mar. 2015, pp. 1690–1694.
- [55] —, “Power control with variable target SINR for D2D communications underlying cellular networks,” in *Proc. European Wireless Conf.*, Barcelona, Spain, May 2014, pp. 1–6.

- [56] —, “Uplink power control with variable target SINR for D2D communications underlying cellular networks,” in *Proc. IEEE Vehicular Technol. Conf. (VTC)*, Glasgow, UK, May 2015, pp. 1–5.
- [57] K. S. Ali, H. ElSawy, and M.-S. Alouini, “On mode selection and power control for uplink D2D communication in cellular networks,” in *Proc. IEEE Int. Commun. Workshop (ICCW)*, London, UK, Jun. 2015, pp. 620–626.
- [58] M. Banagar, B. Maham, P. Popovski, and F. Pantisano, “Power distribution of device-to-device communications in underlaid cellular networks,” *IEEE Wireless Commun. Letters*, vol. 5, no. 2, pp. 204–207, Apr. 2016.
- [59] M. Islam, A. Taha, S. Akl, and S. Choudhury, “A two-phase auction-based fair resource allocation for underlying D2D communications,” in *Proc. IEEE Int. Conf. Commun. (ICC)*, Kuala Lumpur, Malaysia, May 2016, pp. 1–6.
- [60] H. Yousefi, Q. Rahman, and X. Wang, “Delay-tolerant resource allocation for D2D communication using matching theory,” in *Proc. IEEE Vehicular Technol. Conf. (VTC)*, Toronto, ON, Canada, Sep. 2017, pp. 1–6.
- [61] J. Liu, J. Dai, N. Kato, and N. Ansari, “Optimizing uplink resource allocation for D2D overlaying cellular networks with power control,” in *Proc. IEEE Global Commun. Conf. (GLOBECOM)*, Washington, DC, USA, 2016, pp. 1–6.
- [62] J. Liu, J. Dai, Y. Kawamoto, and N. Kato, “Optimizing channel allocation for D2D overlaying multi-channel downlink cellular networks,” in *Proc. IEEE Vehicular Technol. Conf. (VTC)*, Montreal, QC, Canada, Sep. 2016, pp. 1–5.
- [63] Y. Huang, A. A. Nasir, S. Durrani, and X. Zhou, “Mode selection, resource allocation, and power control for D2D-enabled two-tier cellular network,” *IEEE Trans. Commun.*, vol. 64, no. 8, pp. 3534–3547, Aug. 2016.
- [64] L. Wang *et al.*, “Hypergraph-based wireless distributed storage optimization for cellular D2D underlays,” *IEEE J. Sel. Areas Commun.*, vol. 34, no. 10, pp. 2650–2666, Oct. 2016.
- [65] H. Tang and Z. Ding, “Mixed mode transmission and resource allocation for D2D communication,” *IEEE Trans. Wireless Commun.*, vol. 15, no. 1, pp. 162–175, Jan. 2016.
- [66] L. Wang and G. L. Stuber, “Pairing for resource sharing in cellular device-to-device underlays,” *IEEE Netw.*, vol. 30, no. 2, pp. 122–128, Mar. 2016.

- [67] *Evolved Universal Terrestrial Radio Access (E-UTRA); physical layer procedures (Release 13)*, 3GPP Std. TS 36.213. [Online]. Available: <http://www.3gpp.org>
- [68] U. Schilcher *et al.*, “Interference functionals in Poisson networks,” *IEEE Trans. Inf. Theory*, vol. 62, no. 1, pp. 370–383, Jan. 2016.
- [69] D. Stoyan, W. Kendall, and J. Mecke, *Stochastic Geometry and its Applications*, 2nd ed. John Wiley and Sons, 1996.
- [70] F. Baccelli and B. Błaszczyszyn, *Stochastic Geometry and Wireless Networks*. NOW: Foundations and Trends in Networking, 2010.
- [71] X. Zhang and M. Haenggi, “Random power control in Poisson networks,” *IEEE Trans. Commun.*, vol. 60, no. 9, pp. 2602–2611, Sep. 2012.
- [72] N. Jindal, S. Weber, and J. G. Andrews, “Fractional power control for decentralized wireless networks,” *IEEE Trans. Wireless Commun.*, vol. 7, no. 12, pp. 5482–5492, Dec. 2008.
- [73] Y. Huang, C. Zhang, J. Wang, Y. Jing, L. Yang, and X. You, “Signal processing for MIMO-NOMA: Present and future challenges,” *IEEE Wireless Commun.*, vol. 25, no. 2, pp. 32–38, Apr. 2018.
- [74] Q. Sun, S. Han, C. I, and Z. Pan, “On the ergodic capacity of MIMO NOMA systems,” *IEEE Wireless Commun. Lett.*, vol. 4, no. 4, pp. 405–408, Aug. 2015.
- [75] J. Zhu, J. Wang, Y. Huang, S. He, X. You, and L. Yang, “On optimal power allocation for downlink non-orthogonal multiple access systems,” *IEEE J. Sel. Areas Commun.*, vol. 35, no. 12, pp. 2744–2757, Dec. 2017.
- [76] C. Wang, J. Chen, S. Lam, and P. Xiao, “Joint clustering and precoding for a downlink non-orthogonal multiple access system with multiple antennas,” in *Proc. IEEE Vehic. Technol. Conf. (VTC)*, Sep. 2016, pp. 1–5.
- [77] Z. Ding, F. Adachi, and H. V. Poor, “Performance of MIMO-NOMA downlink transmissions,” in *Proc. IEEE Global Commun. Conf. (GLOBECOM)*, Dec. 2015, pp. 1–6.
- [78] —, “The application of MIMO to non-orthogonal multiple access,” *IEEE Trans. Wireless Commun.*, vol. 15, no. 1, pp. 537–552, Jan. 2016.
- [79] Z. Chen and X. Dai, “MED precoding for multiuser MIMO-NOMA downlink transmission,” *IEEE Trans. Veh. Technol.*, vol. 66, no. 6, pp. 5501–5505, Jun. 2017.

- [80] Y. Zhao, W. Xu, and S. Jin, "An minorization-maximization based hybrid precoding in NOMA-mMIMO," in *2017 9th International Conference on Wireless Communications and Signal Processing (WCSP)*, Oct. 2017, pp. 1–6.
- [81] L. Liu, C. Yuen, Y. L. Guan, and Y. Li, "Capacity-achieving iterative lmmse detection for MIMO-NOMA systems," in *Proc. IEEE Int. Conf. Commun. (ICC)*, May 2016, pp. 1–6.
- [82] L. Liu, C. Yuen, Y. L. Guan, Y. Li, and C. Huang, "Gaussian message passing iterative detection for MIMO-NOMA systems with massive access," in *Proc. IEEE Global Commun. Conf. (GLOBECOM)*, Dec. 2016, pp. 1–6.
- [83] L. Bai, J. Choi, and Q. Yu, *Low complexity MIMO receivers*. Springer, 2014.
- [84] E. Viterbo and J. Boutros, "A universal lattice code decoder for fading channels," *Information Theory, IEEE Transactions on*, vol. 45, no. 5, pp. 1639–1642, 1999.
- [85] M. M. Mansour, S. P. Alex, L. M. Jalloul *et al.*, "Reduced complexity soft-output mimo sphere detectors-part I: Algorithmic optimizations," *Signal Processing, IEEE Transactions on*, vol. 62, no. 21, pp. 5505–5520, 2014.
- [86] H. Q. Ngo, E. G. Larsson, and T. L. Marzetta, "Energy and spectral efficiency of very large multiuser MIMO systems," *IEEE Trans. Commun.*, vol. 61, no. 4, pp. 1436–1449, Apr. 2013.
- [87] P. Li and R. D. Murch, "Multiple output selection-LAS algorithm in large MIMO systems," *IEEE Commun. Lett.*, vol. 14, no. 5, pp. 399–401, May 2010.
- [88] N. Srinidhi, T. Datta, A. Chockalingam, and B. S. Rajan, "Layered tabu search algorithm for large-MIMO detection and a lower bound on ML performance," *IEEE Trans. Commun.*, vol. 59, no. 11, pp. 2955–2963, Nov. 2011.
- [89] T. L. Narasimhan and A. Chockalingam, "Channel hardening-exploiting message passing (CHEMP) receiver in large-scale MIMO systems," *IEEE J. Sel. Topics Signal Process.*, vol. 8, no. 5, pp. 847–860, Oct. 2014.
- [90] Q. Zhou and X. Ma, "Element-based lattice reduction algorithms for large MIMO detection," *IEEE J. Sel. Areas Commun.*, vol. 31, no. 2, pp. 274–286, Feb. 2013.

- [91] T. Datta, N. A. Kumar, A. Chockalingam, and B. S. Rajan, "A novel Monte-Carlo-sampling-based receiver for large-scale uplink multiuser MIMO systems," *IEEE Trans. Veh. Technol.*, vol. 62, no. 7, pp. 3019–3038, Sept. 2013.
- [92] J. Choi, "Nulling and cancellation detector for MIMO and its application to multistage receiver for coded signals: performance and optimization," *IEEE Trans. Wireless Commun.*, vol. 5, no. 5, pp. 1207–1216, 2006.
- [93] D. W. Waters and J. R. Barry, "The Chase family of detection algorithms for multiple-input multiple-output channels," *IEEE Trans. Signal Process.*, vol. 56, no. 2, pp. 739–747, 2008.
- [94] M. Siti and M. P. Fitz, "A novel soft-output layered orthogonal lattice detector for multiple antenna communications," in *Communications, 2006. ICC'06. IEEE International Conference on*, vol. 4. IEEE, 2006, pp. 1686–1691.
- [95] Y. Jiang, J. Li, and W. W. Hager, "Joint transceiver design for MIMO communications using geometric mean decomposition," *IEEE Trans. Signal Process.*, vol. 53, no. 10, pp. 3791–3803, 2005.
- [96] —, "Uniform channel decomposition for MIMO communications," *IEEE Trans. Signal Process.*, vol. 53, no. 11, pp. 4283–4294, 2005.
- [97] S. L. Ariyavisitakul, J. Zheng, E. Ojard, and J. Kim, "Subspace beamforming for near-capacity mimo performance," *Signal Processing, IEEE Transactions on*, vol. 56, no. 11, pp. 5729–5733, 2008.
- [98] H. Sameddeen, M. M. Mansour, and A. Chehab, "Hard-output chase detectors for large MIMO: BER performance and complexity analysis," in *Proc. IEEE Int. Symp. Personal Indoor and Mobile Radio Commun. (PIMRC)*, Montreal, Canada, Oct. 2017, pp. 1–5.
- [99] H. Sameddeen, M. M., and A. Chehab, "Channel-punctured large mimo detection," in *Proc. IEEE Int. Symp. Information Theory (ISIT)*, Vail, CO, USA, Jun. 2018, p. (to appear).
- [100] M. M. Mansour, "A near-ml mimo subspace detection algorithm," *Signal Processing Letters, IEEE*, vol. 22, no. 4, pp. 408–412, 2015.
- [101] O. B. Usman, H. Jedda, A. Mezghani, and J. A. Nossek, "MMSE precoder for massive MIMO using 1-bit quantization," in *Proc. IEEE Int. Conf. Acoustics, Speech, and Signal Process. (ICASSP)*, Mar. 2016, pp. 3381–3385.

- [102] O. B. Usman, J. A. Nossek, C. A. Hofmann, and A. Knopp, "Joint MMSE precoder and equalizer for massive MIMO using 1-bit quantization," in *Proc. IEEE Int. Conf. Commun. (ICC)*, May 2017, pp. 1–6.
- [103] M. Alonzo and S. Buzzi, "Cell-free and user-centric massive MIMO at millimeter wave frequencies," in *Proc. IEEE Int. Symp. Personal Indoor and Mobile Radio Commun. (PIMRC)*, Montreal, QC, Canada, Oct. 2017, pp. 1–5.
- [104] M. Alonzo, S. Buzzi, A. Zappone, and C. D'Elia, "Energy-efficient power control in cell-free and user-centric massive mimo at millimeter wave," *IEEE Transactions on Green Communications and Networking*, vol. 3, no. 3, pp. 651–663, Sep. 2019.
- [105] M. Bashar, K. Cumanan, A. G. Burr, M. Debbah, and H. Q. Ngo, "On the Uplink Max–Min SINR of Cell-Free Massive MIMO systems," *IEEE Trans. Wireless Commun.*, vol. 18, no. 4, pp. 2021–2036, Apr. 2019.
- [106] R. Schmidt, "Multiple emitter location and signal parameter estimation," *IEEE Trans. Antennas Propag.*, vol. 34, no. 3, pp. 276–280, Mar. 1986.
- [107] R. Roy and T. Kailath, "ESPRIT estimation of signal parameters via rotational invariance techniques," *IEEE Trans. Acoust., Speech, Signal Process.*, vol. 37, no. 7, pp. 984–995, Jul. 1989.
- [108] H. Krim and M. Viberg, "Two decades of array signal processing research: the parametric approach," *IEEE Signal Process. Mag.*, vol. 13, no. 4, pp. 67–94, Jul. 1996.
- [109] T. Wang, B. Ai, R. He, and Z. Zhong, "Two-dimension direction-of-arrival estimation for massive MIMO systems," *IEEE Access*, vol. 3, pp. 2122–2128, Nov. 2015.
- [110] A. Hu, T. Lv, H. Gao, Z. Zhang, and S. Yang, "An ESPRIT-based approach for 2-D localization of incoherently distributed sources in massive MIMO systems," *IEEE J. Sel. Topics Signal Process.*, vol. 8, no. 5, pp. 996–1011, Oct. 2014.
- [111] L. Cheng, Y. Wu, J. Zhang, and L. Liu, "Subspace identification for DoA estimation in massive/full-dimension MIMO systems: Bad data mitigation and automatic source enumeration," *IEEE Trans. Signal Process.*, vol. 63, no. 22, pp. 5897–5909, Nov. 2015.
- [112] R. Shafin, L. Liu, J. Zhang, and Y. Wu, "DoA estimation and capacity analysis for 3-D millimeter wave massive-MIMO/FD-MIMO OFDM systems," *IEEE Trans. Wireless Commun.*, vol. 15, no. 10, pp. 6963–6978, Oct. 2016.

- [113] D. Fan, Y. Deng, F. Gao, Y. Liu, G. Wang, Z. Zhong, and A. Nallanathan, "Training based DoA estimation in hybrid mmWave massive MIMO systems," in *Proc. IEEE Global Commun. Conf. (GLOBECOM)*, Singapore, Singapore, Dec. 2017, pp. 1–6.
- [114] H. Xie, F. Gao, S. Zhang, and S. Jin, "A unified transmission strategy for TDD/FDD massive MIMO systems with spatial basis expansion model," *IEEE Trans. Veh. Technol.*, vol. 66, no. 4, pp. 3170–3184, Apr. 2017.
- [115] D. Fan, F. Gao, Y. Liu, Y. Deng, G. Wang, Z. Zhong, and A. Nallanathan, "Angle domain channel estimation in hybrid mmWave massive MIMO systems," *IEEE Trans. Wireless Commun.*, vol. 17, no. 12, pp. 8165–8179, Dec. 2018.
- [116] S. Kim and B. Shim, "FDD-based cell-free massive MIMO systems," in *Proc. IEEE Int. Sig. Process. Advances in Wireless Commun. Workshop (SPAWC)*, Kalamata, Greece, Jun. 2018, pp. 1–5.
- [117] J. G. Andrews, A. K. Gupta, and H. S. Dhillon, "A primer on cellular network analysis using stochastic geometry," *arXiv preprint arXiv:1604.03183*, 2016.
- [118] D. Moltchanov, "Distance distributions in random networks," *Ad Hoc Networks*, vol. 10, no. 6, pp. 1146–1166, 2012.
- [119] *Evolved Universal Terrestrial Radio Access (E-UTRA); Radio Resource Control (RRC) (Release 13)*, 3GPP Std. TS 36.331. [Online]. Available: <http://www.3gpp.org>
- [120] S. Gupta, R. D. Yates, and C. Rose, "Soft dropping power control—a power control backoff strategy," in *Proc. IEEE Int. Personal Wireless Commun. (PWC)*, Mumbai, India, Dec. 1997, pp. 210–214.
- [121] *Proximity-based services (ProSe); Stage 2 (Release 13)*, 3GPP Std. TS 23.303. [Online]. Available: <http://www.3gpp.org>
- [122] S. Chandrasekharan *et al.*, "Propagation measurements for D2D in rural areas," in *Proc. IEEE Int. Commun. Workshop (ICCW)*, London, UK, Jun. 2015, pp. 639–645.
- [123] *Universal Geographical Area Description (GAD) (Release 13)*, 3GPP Std. TS 23.032. [Online]. Available: <http://www.3gpp.org>
- [124] N. Al-Dhahir and J. M. Cioffi, "On the uniform adc bit precision and clip level computation for a gaussian signal," *IEEE Trans. Signal Process.*, vol. 44, no. 2, pp. 434–438, Feb. 1996.

- [125] J. Bussgang, “Crosscorrelation functions of amplitude-distorted Gaussian signals,” Massachusetts Institute of Technology, Technical report TK7855.M41 R43 no.216, Mar. 1952.
- [126] C. Mollén, J. Choi, E. Larsson, and R. W. Heath, “Uplink performance of wideband massive MIMO with one-bit ADCs,” *IEEE Trans. Wireless Commun.*, vol. 16, no. 1, pp. 87–100, Jan. 2017.
- [127] B. Hassibi and B. M. Hochwald, “How much training is needed in multiple-antenna wireless links?” *IEEE Trans. Inf. Theory*, vol. 49, no. 4, pp. 951–963, Apr. 2003.
- [128] N. Kim, Y. Lee, and H. Park, “Performance analysis of MIMO system with linear MMSE receiver,” *IEEE Trans. Wireless Commun.*, vol. 7, no. 11, pp. 1536–1276, Nov. 2008.
- [129] S. N. Diggavi and T. M. Cover, “The worst additive noise under a covariance constraint,” *IEEE Transactions on Information Theory*, vol. 47, no. 7, pp. 3072–3081, Nov 2001.
- [130] L. Fan, S. Jin, C. Wen, and H. Zhang, “Uplink achievable rate for massive mimo systems with low-resolution adc,” *IEEE Commun. Letters*, vol. 19, no. 12, pp. 2186–2189, Dec 2015.
- [131] H. Ngo, E. Larsson, and T. Marzetta, “Energy and spectral efficiency of very large multiuser MIMO systems,” *IEEE Trans. Commun.*, vol. 61, no. 4, pp. 1436–1449, Apr. 2013.
- [132] P. Li, D. Paul, R. Narasimhan, and J. Cioffi, “On the distribution of SINR for the MMSE MIMO receiver and performance analysis,” *IEEE Trans. Inf. Theory*, vol. 52, no. 1, pp. 271–286, Jan. 2006.
- [133] M. Joham, W. Utschick, and J. A. Nossek, “Linear transmit processing in mimo communications systems,” *IEEE Trans. Signal Process.*, vol. 53, no. 8, pp. 2700–2712, Aug 2005.
- [134] D. M. Arnold, H. . Loeliger, P. O. Vontobel, A. Kavcic, and W. Zeng, “Simulation-based computation of information rates for channels with memory,” *IEEE Transactions on Information Theory*, vol. 52, no. 8, pp. 3498–3508, Aug 2006.
- [135] T. Marzetta and B. Hochwald, “Capacity of a mobile multiple-antenna communication link in Rayleigh flat fading,” *IEEE Trans. Inf. Theory*, vol. 45, no. 1, pp. 139–157, Jan. 1999.

- [136] F. Fernandes, A. Ashikhmin, and T. L. Marzetta, “Inter-cell interference in noncooperative TDD large scale antenna systems,” *IEEE J. Sel. Areas Commun.*, vol. 31, no. 2, pp. 192–201, Feb. 2013.
- [137] R. Chopra, C. R. Murthy, H. A. Suraweera, and E. G. Larsson, “Performance analysis of FDD massive MIMO systems under channel aging,” *IEEE Trans. Wireless Commun.*, vol. 17, no. 2, pp. 1094–1108, Feb. 2018.
- [138] K. Hugl, K. Kalliola, and J. Laurila, “Spatial reciprocity of uplink and downlink radio channels in FDD systems,” in *Proc. COST*, vol. 273, no. 2. Citeseer, 2002, p. 066.
- [139] C. Stoeckle, J. Munir, A. Mezghani, and J. A. Nossek, “DoA estimation performance and computational complexity of subspace- and compressed sensing-based methods,” in *Proc. Int. ITG Workshop on Smart Antennas (WSA)*, Ilmenau, Germany, Mar. 2015.
- [140] E. Björnson, J. Hoydis, L. Sanguinetti *et al.*, “Massive MIMO networks: Spectral, energy, and hardware efficiency,” *Foundations and Trends® in Signal Processing*, vol. 11, no. 3-4, pp. 154–655, 2017.
- [141] Z. Luo, W. Ma, A. M. So, Y. Ye, and S. Zhang, “Semidefinite relaxation of quadratic optimization problems,” *IEEE Signal Processing Magazine*, vol. 27, no. 3, pp. 20–34, May 2010.
- [142] M. Grant, S. Boyd, and Y. Ye, “CVX: Matlab software for disciplined convex programming,” 2008.
- [143] S. Boyd and L. Vandenberghe, *Convex Optimization*. Cambridge University Press, 2004.
- [144] R. V. C. Helmberg, F. Rendl and H. Wolkowicz, “An interior-point method for semi-definite programming,” *SIAM J. Optim.*, vol. 6, no. 2, p. 342–361, 1996.
- [145] H. Ye, G. Y. Li, and B. Juang, “Power of deep learning for channel estimation and signal detection in ofdm systems,” *IEEE Wireless Communications Letters*, vol. 7, no. 1, pp. 114–117, Feb 2018.
- [146] C. He, Y. Hu, Y. Chen, and B. Zeng, “Joint power allocation and channel assignment for noma with deep reinforcement learning,” *IEEE J. Sel. Areas Commun.*, vol. 37, no. 10, pp. 2200–2210, Oct 2019.
- [147] D. Gündüz, P. de Kerret, N. D. Sidiropoulos, D. Gesbert, C. R. Murthy, and M. van der Schaar, “Machine learning in the air,” *IEEE J. Sel. Areas Commun.*, vol. 37, no. 10, pp. 2184–2199, Oct 2019.

- [148] . T. Demir and E. Björnson, “Channel estimation in massive mimo under hardware non-linearities: Bayesian methods versus deep learning,” *IEEE Open Journal of the Commun. Soc.*, vol. 1, pp. 109–124, 2020.
- [149] G. Grimmett and D. Stirzaker, *Probability and random processes*. Oxford University Press, 2001.